ABSTRACT

The problem of ice movement is considered both with respect to the 1968 Gulf of St. Lawrence Ice Drift Study and from the theoretical point of view. Gulf data are analysed to determine the influence of tides and windstress. Statistical tests on the data include an analysis of the relation between geostrophic and surface wind, transient response and spectral analysis. The Reed and Campbell model is tested and good agreement found with observed ice speed, though not with direction. A non-linear inertial ice drift model is studied and numerically integrated with measured wind values. Observed and numerically determined results are compared and the effect of different parameters considered. Finally, the equations of time-dependent motion of water beneath the ice are examined and analytically integrated for an arbitrary forcing function to derive expressions for the drag effect of water on ice. Both uniform eddy viscosity and boundary layer conditions are considered.

Title: Observations on Ice Movement in the Gulf of St. Lawrence

Author: David Malcolm Farmer

Submitted: July 1969, McGill University

Degree: Master of Science, Marine Science Center

OBSERVATIONS ON ICE MOVEMENT IN THE GULF OF ST. LAWRENCE

by

David Malcolm Farmer

Being a thesis submitted to the Faculty of Graduate Studies and Research, McGill University, in partial fulfillment of the requirements for the degree of Master of Science.

Montreal July 1969

ACKNOWLEDGEMENTS

The author wishes to thank Dr. E.R. Pounder for making it possible for him to undertake this study and for his helpful guidance.

It is also a pleasure to acknowledge the assistance of Drs. K. Hunkins, S. Savage, O. Johannessen, S. Orvig and K. Tam for contributing many useful ideas during the course of this study.

Many of the geostrophic wind values and all of the data from meteorological stations around the Gulf were kindly supplied by J. Walmsley. The author is also indebted to H.Serson for providing notes on the original collection of data, to W.Seifert for help in translating German papers, to R.H. Farmer for assistance in devising the scheme given in Appendix 2 and to the staff of the McGill inter-library loan service for promptly obtaining numerous periodicals from outside the University.

This study was financed by the National Research Council of Canada.

TABLE OF CONTENTS

TABLE OF CONTENTS (cont'd.) Page

LIST OF FIGURES

LIST OF FIGURES (cont'd.) Page

LIST OF TABLES

Chapter 1 - Introduction

This thesis is concerned with a number of topics relevant to the movement of sea-ice, both in connection with the drift of a manned ice station in the Gulf of St. Lawrence and also with the theoretical problem of time dependent motion.

In some respects an area such as the Gulf is much easier to study than a vast region like the Arctic Ocean. It is closer, better surveyed and is surrounded by meteorological stations. But it also presents many difficulties not encountered in the open ocean. The tide is no longer simply related to the tidal potential, but is a complicated function of the shape of the basin and it is much stronger than oceanic tides. Strong, narrowly defined and fluctuating currents are present. Moreover, to be of value, ice drift predictions must be much more accurate in the absolute sense on account of the smaller scale involved.

In choosing the most relevant topics for analysis consideration had to be given to the limitations of the data and the local conditions. The predominantly wind-driven nature of ice drift in the Gulf, and the strong tides both suggest the importance of studying these influences. On the other hand there is very little known about surface currents, particularly in the winter, and it is difficult at this stage to investigate their effect on ice movement with any precision. Part of the difficulty lies in the fact that with the exception of the Gaspé current, the surface movements of the Gulf are greatly influenced by meteorological conditions. The wind drives the ice and the ice drives

the water beneath it; but currents can also be set up by variations in the atmospheric pressure distribution around the Gulf. Unfortunately attempts to measure current in the study described here were largely unsuccessful.

A further consideration in the choice of topics was the requirement of appropriate computer programmes for future ice-drift studies at McGill. Thus rather more attention than might otherwise seem warranted has been paid to numerical procedures in certain cases, such as in the discussion of functional approximation for velocity estimation from position fixes. Flow diagrams of the more important programmes are given in Appendix 1.

Theoretical investigations of drift have been confined almost exclusively to steady state problems in which the ice is presumed to travel in the same direction at a constant velocity. But inasmuch as the wind itself rarely blows at the same speed in the same direction for any great length of time, the ice must be constantly changing its velocity. In discussing the transient motion of sea-ice, Reed and Campbell (1960) state that "Accurate prediction of ice displacement will never be achieved by summation of equilibrium drift vectors. A more precise solution of the prediction problem must be based on integration of the complete equations of motion, with acceleration included; and, because of the non linear nature of these equations, the integration must be performed by numerical methods. It is not too early to ask how such numerical predictions may be carried out in principle and to contemplate the obstacles which stand in the way of their practical achievement....

"Despite these difficulties early experiments in numerical

prediction are desirable. Drastic assumptions will be necessary. The internal stresses may be neglected, and the water drag may be handled crudely. Nevertheless, important insights into complex ice movements may be gained and the foundation laid for more realistic approaches".

In this spirit the last two chapters of this thesis are offered. A simple inertial model is used with actual wind data. Finally the equations of motion are investigated and put into a form in which they can be handled numerically. Unfortunately there has not been time to run test data on the latter model, but it is hoped that it may prepare the way for more sophisticated ice-drift experiments.

Chapter 2 - McGill Ice Drift Station

2.1 - McGill Ice Studies

Ice studies in the Gulf of St. Lawrence have been carried out by the Marine Sciences Centre at McGill each winter since 1967. Ingram (1967) examined ice charts issued by Ice Forecasting Central in Halifax. Daily movements of individual floes were traced and the motion was accounted for by a modified form of the drift theory proposed by Reed and Campbell (1960). One result of this work was the preparation of a map of surface residual currents that were assumed to explain the difference between the theoretical ice movements and those actually observed.

In March 1967 a Geodyne toroidal buoy equipped with a radio beacon was set down on an ice-floe off the Gaspé coast. During its drift to the south-east, seven position fixes were obtained by the Ice Reconnaissance aircraft over a period of twenty days until the beacon stopped transmitting. The Reed and Campbell drift theory was used to estimate the drift due to wind stress values obtained from the pressure maps, the difference between observed and predicted results providing an indication of surface current. The results suggest that as the floe approached the Magdalen Islands, internal ice stress slowed its progress. A full report of this study is given by Ingram, Johannessen and Pounder (1968).

The 1967 study had indicated the advantage that might be gained by using a manned drifting station. In February 1968 the project which is the subject of discussion in this thesis was undertaken.

A life-raft manned by three persons, H. Serson, J. Keys and W. Seifert, was set down on an ice-floe 38 kilometers north of St. Anne des Monts, together with an instrumented buoy. For six days the floe drifted down through the Gaspé Passage (Figure 2.01) under the influence of severe weather conditions. After evacuation of the station the instrumented buoy continued to drift under the influence of the wind until picked up by ice-breaker on February 22nd.

In February 1969 another ice study was carried out. On this occasion the sealing vessel "M/V Polarfish" was used and observations included the measurement of surface Reynolds stress and floe interaction, in addition to drift and current. A preliminary account of these investigations is given by Johannessen et al. (1969).

2.2 - M.D.S.: Logistics, Instrumentation

Since a fairly detailed account of the logistics and instrumentation of the 1968 ice study is given in Johannessen et al. (1968), the following brief description is repeated for completeness only and reference is made to the Preliminary Report for further details.

A fourteen foot diameter pneumatic life-raft supported by plywood six inches above the ice was used for accommodation. In addition a four foot square shelter was set up for hydrographic work.

The equipment and crew were brought in and evacuated by ice-breaker. Helicopter support was also provided, an S-55 helicopter being stationed at St. Anne des Monts.

The unique aspect of the manned drifting station, hereafter referred to as "M.D.S.", was that it included navigation equipment

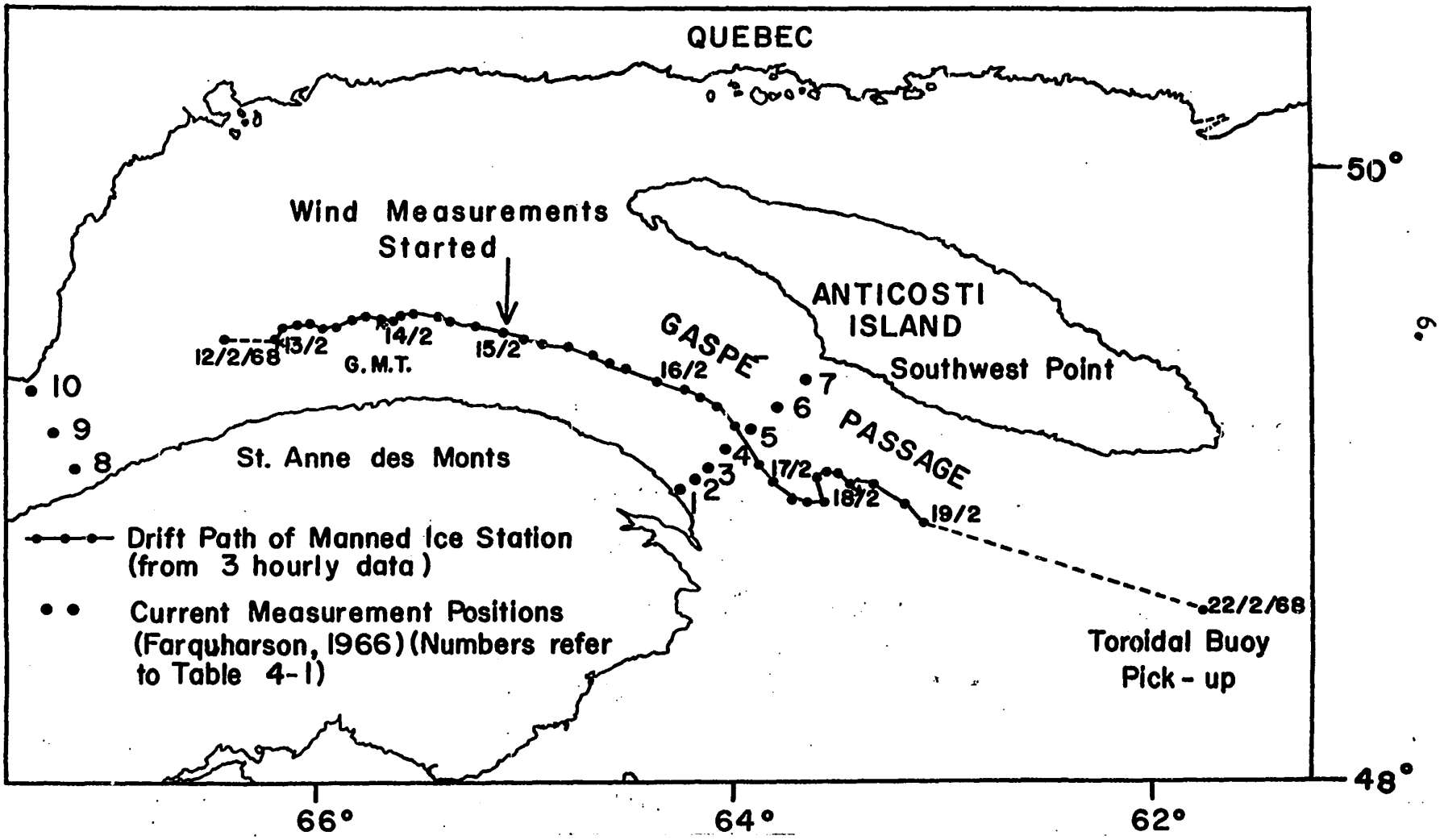

Figure 2.01 - Drift of Manned Ice Station.

intended to give frequent and accurate position fixes. The Decca installation consisted of a Mark V receiver fed from a 20 foot whip antenna, which drove a C.D.C. analog to digital converter. Output was provided by a Kellog paper tape printer. The device was intended to give position fixes once every two minutes.

Two anemometers were used, a Lambrecht paper-tape and a Geodyne film-recording model each using 3-cup sensors. The first of these provided a continuous record of wind speed and direction. The film-recording anemometer, which was set up soon after the paper tape model was in operation, was adjusted to take twelve wind samples over each twenty minute period. It was mounted on a 9 foot mast attached to the toroidal buoy.

Suspended beneath the buoy was a film recording current meter and a telemetering current meter, the latter being connected to a tape-recorder mounted in a shelter on the buoy. In addition a surface read-out current meter was used.

The data collected was considerably less than that originally anticipated. Power failures caused by the sensitivity of the generator to severe weather conditions rendered position fixing intermittant. In addition the output printer behaved erratically in the cold and provided unreliable results for much of the observation period. The shelter, set up on the buoy to house the tape-recorder, caught fire; the equipment survived but a fault in the tape-recorder prevented any information from the telemetering current meter being retained. The film-recording current meter was snapped off its cable and lost, possibly because of ice rafting. The only remaining current meter,

a Plessey surface read-out device behaved most erratically. Subsequent tests (H. Serson, personal communication) showed that the stainless steel hull containing the current-meter with its magnetic compass, had a residual magnetism of its own. The current data will not be considered in this thesis. Both anemometers did function, the film recording model continuing to provide output during occupation of the station, but it stopped working 22 hours later.

In addition, difficulty was encountered in determining the position of the radio beacon equipped buoy. For this reason the toroidal buoy was recovered only 3 days after M.D.S. was evacuated, although it had been planned to leave it out for 1½ to 2 months.

2.3 - Ice Characteristics

M.D.S. was situated on a larger than average ice-floe approximately 3 km across by 5 km long. A helicopter survey on February 10th showed the floe to be surrounded by moving ice of 8/10 concentration. Close to shore there was a region of land-fast ice 3-5 kilometers wide, beyond which floated ice-pans of about 5 m. diameter and floes of 20-500 m. diameter. Approximately 30 kilometers off the south shore there was a band of open water with a maximum ice concentration of 3/10. The floe was oriented in a N.E. - S.W. direction. At the south and west edge of the floe the ice cover was 10/10, though not solid, but was 7/10 north and east of the floe. Farther east ice concentration increased to 9/10.

Department of Transport ice reconnaissance maps show additional details of the ice coverage for the area in which M.D.S. was drifting for the 13th, 14th, 16th, 17th and 21st February. These are recorded in Table 2-1. M.D.S. appears to have been situated in a rather large

TABLE 2-1

Ice characteristics in area of manned drifting station, taken from Department of Transport Ice maps. Concentration given in tenths.

Date	General Classification of Ice in Area of M.D.S.	Details: Thick Winter	Medium Winter	Young	New	Other Details
Feb. 13th	7/10 - 9/10 Young. Medium sized floes or greater.	1/10	3/10 (2/10 med. sized floes)	4/10 (2/10 med. sized floes)	1/10	
Feb. 14th	7/10 - 9/10 Young. Medium sized floes or greater.	1/10	4/10 (3/10 med. sized floes)	4/10 (4/10 med. sized floes)	1/10	1/10 Ridging 1/10 - 2/10 rafted ice
Feb. 16th	7/10 - 9/10 Thick Winter. Medium sized floes or greater.	5/10 (3/10 med. sized floes)	4/10 (3/10 med. sized floes)	1/10	0	2/10 - 3/10 Ridging 9/10 snow cover
Feb. 17th	7/10 - 9/10 Thick Winter. Medium sized floes or greater.	5/10 (3/10 med. sized floes)	4/10 (2/10 med. sized floes)	1/10	0	Open Water South of Eastern Anticosti Island.
Feb. 21st	Several ice types in the area; thick winter and young predominating. 7/10 - 10/10 coverage.					1/10 - 2/10 Ridging on thick winter ice; 1/10 - 2/10 rafting on new ice.

area of predominantly young and medium winter ice, 4/10 of which was in the form of medium sized floes or larger. No ridging was present on the 13th, but 1/10 was recorded on the 14th and 2/10 - 3/10 on the 16th. By the 16th the M.D.S. area was classified as predominantly thick winter, still with 7/10 - 8/10 coverage. By convention the tenths of ridging present refers to the proportion of the surface ice cover on which ridging occurs. On the 17th a long tongue of open water was shown south of eastern Anticosti Island. The next report for this area was not issued until February 21st, by which time several small areas of different ice types were recorded, young and thick winter ice predominating.

Measurements of the ice thickness and temperature were taken, reference again being made to Johannessen et al. (1968) for further details. The surface topography was extremely rough, making ice thickness measurements difficult, but measurements indicate a gradual increase in thickness from 30 cm on February 13th to 50 cm five days later.

The floe rotated anticlockwise through 130° in the first two and a half days of observation, thereafter approximately maintaining its orientation.

Chapter 3 - Preparation of Data

3.1 - Navigation Data

For the purposes of ice-drift analysis two main types of data resulted from the M.D.S. operation: position fixes and wind data. Output from the Decca equipment was in two forms; that provided by the paper tape printer and that recorded by hand at approximately hourly intervals from the visual read-out device. Output from neither of these sources, of course, was available at times when the generator failed, but the manually recorded data did provide a check on the performance of the output printer at other times.

The Decca navigation system consists of one master radio transmitter and one or more slave transmitters situated about the region they serve. Serving the western part of the Gulf of St. Lawrence a master transmitter near Port Menier drives slave stations at Sept Isles, Shippegan Island and Natashquan. The receiving device uses the signal pattern created by any two transmitters to determine the location. Since more than two signals can be received in the Gulf of St. Lawrence, extra position fixes can be obtained as a check on the first. The equipment does not give a position in terms of latitude or longitude, but in terms of two numbers, each number referring to a certain hyperbola centered on the respective transmitter location. The numbers may then be used to read off positions directly from a specially prepared map on which the appropriate intersecting curves, colour coded to each transmitter, are drawn. Alternatively the numbers may be converted numerically into latitude and longitude, facilities for this work being provided by the equipment agency.

The equipment manufacturer states that in the area of the Gulf in which M.D.S. was under observation, absolute errors of $1\frac{1}{2}$ nautical miles at night and less than $\frac{1}{4}$ mile at day are unlikely at the 95% significance level, to be exceeded more than one in twenty times. In practice, considerably smaller errors may be expected. Furthermore, relative errors between closely spaced position fixes could be smaller still.

The effect of cold on the output printer had been to make the device stick on one number from time to time, and also to jump "lanes", that is, to add some constant to the number being printed. To eliminate as many of these errors as possible the numbers were themselves plotted at ten minute intervals. This procedure clearly indicated lane jumps which could be corrected. Numerous discontinuities and other effects due to malfunctioning of the equipment were also noticed. Where possible these were corrected by reference to the manually recorded position numbers; elsewhere the data was discarded. Another problem that continually plagued the navigation equipment was lane drift. This resulted in an error, increasing apparently linearly with time, until the device automatically corrected itself before repeating the drift in the same way. Again it was generally possible to correct this provided the rate of error accumulation could be determined by reference to the manually recorded figures, but sometimes it was necessary to discard data for this reason also.

After making these preliminary corrections the data were numerically converted into Latitude and Longitude. This was done in two sets: at ten-minute intervals throughout the period of observation

for which reliable data was available, and at two-minute intervals for two 2-hour periods during which the equipment appeared to have operated without mishap.

Since equidistant data is much easier to handle than unevenly spaced data, interpolation was carried out to obtain 10-minute intervals throughout. Interpolation was done using the Aitken-Lagrange scheme. This procedure uses a method of successive approximations and does not suffer the disadvantage of the Lagrangian method in that it is not necessary to decide the best order of the interpolating polynomial in advance (Hildebrand, 1956 & I.B.M., 1968).

After interpolation the data was again plotted by computer, and a few remaining irregularities that must have been caused by instrument malfunction were removed.

3.2 - Smoothing and velocity estimation

It is well known (Ralston, 1965) that derivatives are very hard to estimate accurately by numerical procedures. Various differentiating formulae are available, but they provide no flexibility and may seriously distort results wherever the data is subject to random fluctuations. An alternative procedure is to use some form of functional approximation and then to determine the derivative by analytic differentiation of the function. Both procedures imply some sort of smoothing, but the latter offers much greater flexibility.

The method used in this case was to approximate short sections of the data with Gram orthogonal polynomials using the least squares criterion. The most appropriate least squares polynomial must meet two requirements: it must be of high enough degree so that it provides

a good approximation to the true function, but it must not be of so high a degree that it fits the observed data too closely in the sense that noise, or inaccuracies are retained in the approximation.

Data sets of various lengths were tried using different criteria for establishing the best fit. These indicated than an appropriate degree of smoothing was obtained using 19 points at a time and testing the fit for approximations of successively higher degree until the ratio of the sum of the squared deviations to the number of degrees of freedom ceased to decline significantly (Ralston, 1965). This generally occurred with polynomials of degree two to five. The derivative of the middle point was than found by analytic differentiation in the usual way. The next data set was shifted one time interval forward and the derivative of the mid-point again found, the process being iterated in this way throughout the data series. The first and last fitted 9 points of the series were determined from the first and last fitted polynomials respectively. A scheme for generating the Gram polynomial coefficients is given in Appendix 2.

In order to reduce round-off errors, only the last four significant digits of the latitude and longitude data were used, the appropriate constant being added back after the computation. After determining the derivatives conversion of the velocity values from spherical to Cartesian co-ordinates was made using the relationship

$$U = -R_e \cos\theta \frac{d\phi}{dt}$$

$$V = R_e \frac{d\theta}{dt}$$

where $U, V = x, y$ components of velocity

$R_e =$ radius of the earth

$\theta, \phi =$ Latitude and Longitude

3.3 - Anemometer Data

Wind measurements were taken both by a paper-tape recording anemometer and by a film recording Geodyne model. The film record from the Geodyne anemometer is processed by the manufacturer, by digital computer. Twelve samples are taken over each 20 minute period in order to yield an average value for the interval.

The paper-tape anemometer produced a continuous trace on a slowly moving tape. On account of the fluctuations in the wind and the slow movement of the paper the output is generally in the form of a broad band. Output from the Geodyne model was used exclusively in preference to the paper-tape output except for the first 16 hours in which only the paper-tape anemometer was in operation. The wind data were collected over the period from 0000 hours on February 15th, to 2310 hours on February 19th.

Processing of film output from the Geodyne model automatically included correction for azimuth changes, but this correction was made separately for data from the paper-tape anemometer. Correction was made to both sets of data for deviation of Magnetic North from true North, and the data were interpolated at ten-minute intervals to correspond with the velocity data.

Because of the large amount of position and wind information collected during this study, the data has not been reproduced in this thesis except in graphic form (Figures 4.05 and 4.06). Both raw and processed data are on file at the Marine Sciences Center, McGill University.

Chapter 4 - Tidal Analysis

4.1 - Semidiurnal Tide M_2

In the Gulf of St. Lawrence tides are propagated principally through Cabot Strait. By far the most important tide is the lunar semi-diurnal constituent M_2. A cotidal chart of M_2 as given by Farquharson (1962) for the Gulf of St. Lawrence is shown in Figure 4.01.

The time taken for a progressive wave to travel from Cabot Strait to the main reflecting barrier in the St. Lawrence estuary is approximately equal to one third of the period of the M_2 constituent. For this reason the amphidromic point, at which the nodal lines of transverse and longitudinal semi-diurnal oscillation intersect, lies within the Gulf.

Figure 4.01 shows that the range of M_2 decreases eastwards, down the Gaspé Passage, towards the amphidromic point. A path such as that taken by M.D.S. therefore moves through a region of decreasing tidal range, but fairly constant phaselag, only starting to cut across the cotidal lines sharply in the area south of Southwest Point on Anticosti Island.

Few measurements have been carried out to determine the extent of the horizontal components of M_2. Farquharson (1966) has given surface current measurements taken at the stations shown in Figure 2.01, and these are recorded in Table 4-1. From this it is seen that the direction of the major axis of the tidal ellipse is fairly constant across the Gaspé Passage, being about 296° at the station past which M.D.S. drifted most closely. Farther west the major axis lies at 250° to 270°. The data is sparse, but it seems reasonably clear that the orientation

TABLE 4-1

Tidal current measurements at 13 m. depth in the Gaspé Passage and St. Lawrence Estuary, from Farquharson (1966). Location numbers refer to Figure 2.01.

	M_2			K_1		
Location	Direction	Phase lag	Amplitude (mean)	Direction	Phase lag	Amplitude
1	321°	351°	.36 knots	321°	146°	.05 knots
2	312°	346°	.41 "	312°	143°	.06 "
3	308°	357°	.46 "	308°	148°	.06 "
4	282°	003°	.32 "	282°	135°	.03 "
5	296°	356°	.34 "	296°	162°	.05 "
6	285°	009°	.35 "	285°	126°	.03 "
7	308°	002°	.38 "	308°	136°	.06 "
8	251°	022°	.28 "	251°	143°	.04 "
9	252°	025°	.32 "	252°	142°	.04 "
10	273°	022°	.62 "	273°	151°	.10 "

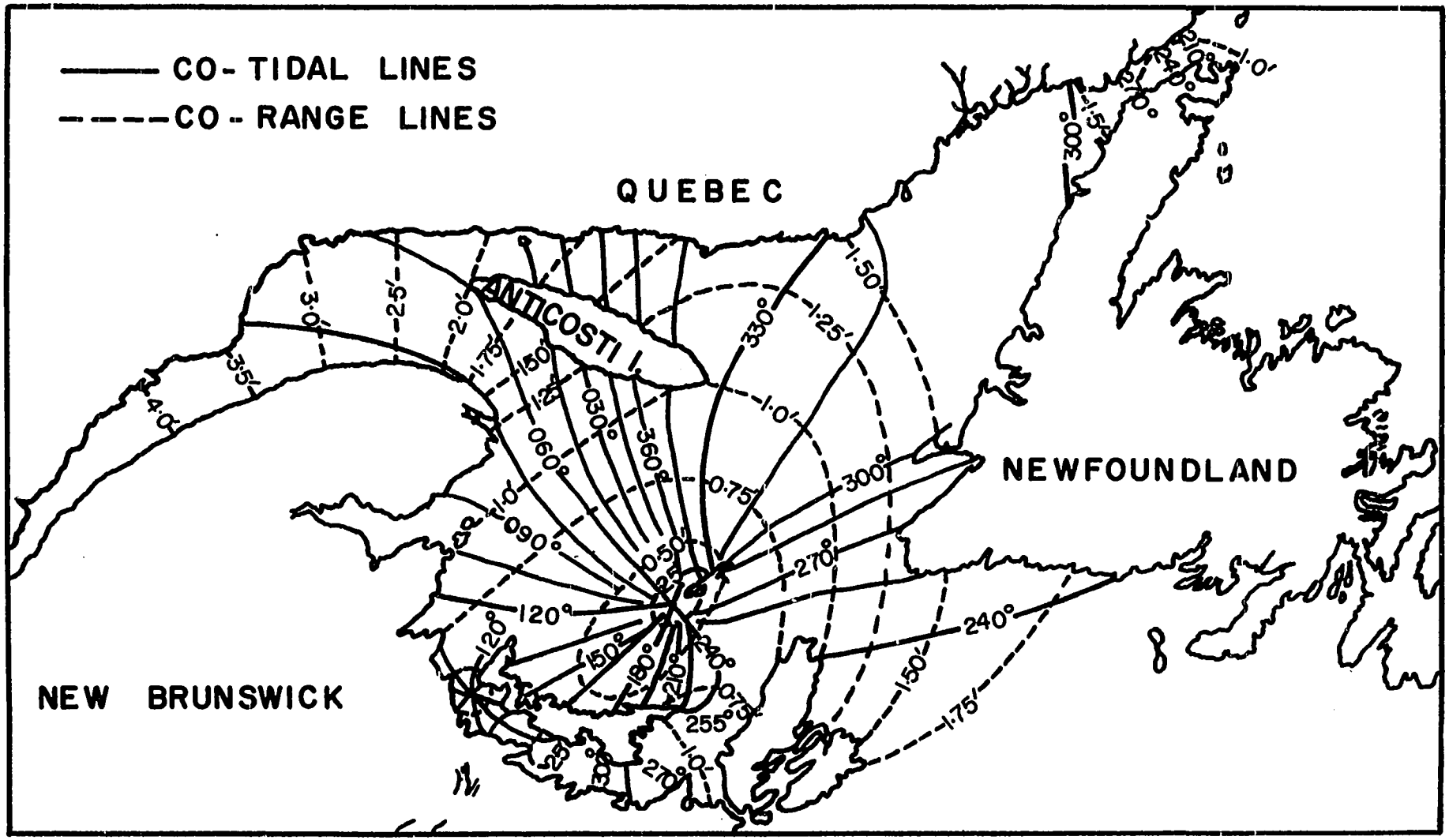

Figure 4.01 - Tidal Constituent M_2 for Gulf - (Farquharson, 1962).

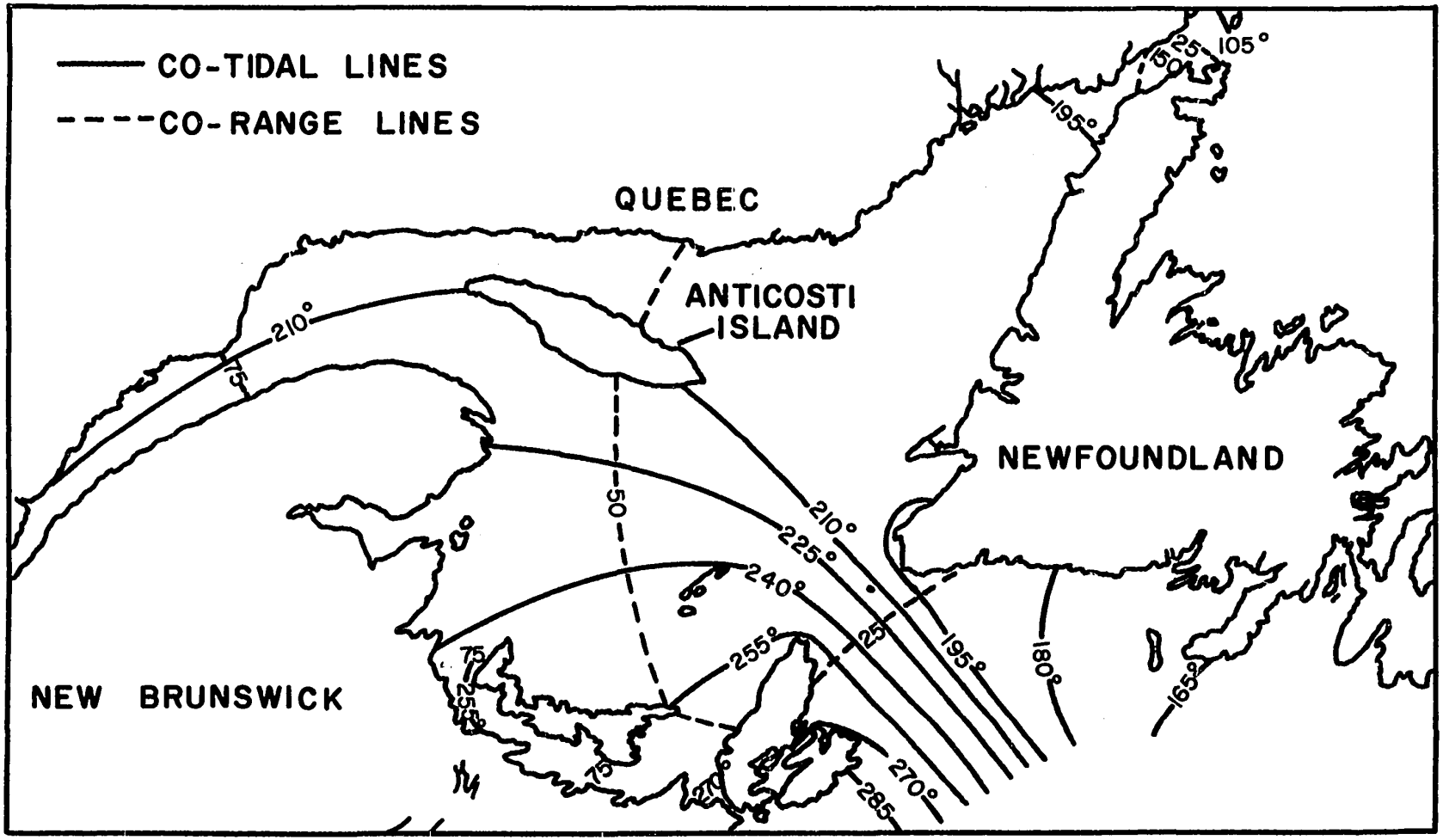

Figure 4.02 - Tidal Constituent K_1 for Gulf - (Farquharson, 1962).

of the major axis followsthat of the south coast through Gaspé Passage.

The minor component is in general very weak. Farquharson (1962) gives respective amplitude ratios of 1:4 and 1:7 for minor to major components at two stations in the Gaspé Passage.

4.2 - Diurnal Tide K_1

Figure 4.02 shows the cotidal and co-range lines for the diurnal oscillation K_1, as given by Farquharson (1962). Since the period of the tide is twice that of the semi-diurnal, the time required for a progressive wave to travel from Cabot Strait to the reflecting barrier is 1/6 that of the diurnal period. The amphidromic point in this case must lie well to seaward of Cabot Strait and it is therefore reasonable to expect the influence of this tide to be fairly uniform throughout the Gulf.

Details of the tidal stream measurements for K_1 are given in Table 4-1. Again the orientation of the ellipse follows the Gaspé coast, but the amplitudes in this case are in general barely one seventh that of the semi-diurnal tide. Farquharson (1962) considers the minor component of the K_1 constituent to be so small that it is of no significance.

Other tidal components include MS_f of 14.8 days period, M_f (13.6 days) and Mm (27.6 days). Although these tides are insignificant in the open ocean, they may be amplified in shallow or semi-enclosed regions. In this case they are important inasmuch as they augment or decrease the tide with which they are associated. MS_f is associated with M_2, M_f with K_1.

Farquharson (1966) considers the net effect of the tidal variations on the daily flows will be that the outgoing tidal stream will be greatest 4 days after new and full moon. Since full moon occurred on February 12th, we should on this basis expect a maximum ingoing tidal stream on February 16th.

4.3 - Residual Currents

Little is known about the surface residual currents in the Gaspé Passage. The Gaspé current is the most significant feature of the area, setting eastward and close to the south shore at an average rate of approximately 1.7 knots. The extent to which the Gaspé current spreads across the Passage varies with astronomical and meteorological conditions. In the northern part of the Passage a weak counter current setting north-west appears to exist. Farquharson (1966) found that currents measured at station 5 past which M.D.S. drifted on the 16th February, varied between .2 knots seaward and .1 knots upstream, the downstream current predominating.

Since full moon occurred on February 12th, in the absence of meteorological effects we might expect a weak ingoing current at the time M.D.S. drifted past station 5. However, the strong westerly winds must have considerably influenced the surface current.

In the 1968 pilot study (Ingram, Johannessen and Pounder, 1968) great variation of current vectors was encountered. The instrumented buoy passed a little closer to the coast than M.D.S., but when it was in a position roughly corresponding to M.D.S. on the 16th February a current towards the E.N.E. at just over one knot was found. A little further to the east there appeared to be no current at all.

4.4 - A method of tidal analysis

Any attempt to analyse the influence of tidal streams for a short period on a moving ice floe runs into considerable difficulties. Since the floe is constantly drifting under the influence of wind and current, the phaselags and amplitudes of the tidal streams affecting the floe are also changing. The more general problem associated with harmonic analysis of short term observations is that created by background noise. In the case under consideration this was particularly severe due to the presence of a strong meteorological disturbance.

The tidal analysis undertaken in this study will follow that given by Fjeldstad (1964) and is a method particularly suited to short-term observations. Fjeldstad originally developed the procedure for studying tide-generated internal waves, but the method is a general one and applicable in the present case. After smoothing the original data, three lunar-hour first order differences are taken. The process is repeated to arrive at second order differences which include an amplification factor that must be taken into acccunt in the computation.

We assume that the observed current may be represented by

$$U = A + Bt + Ct^2 + R_t \cos(\sigma t - \varphi) + \delta \qquad \ldots\ (4.01)$$

where the second degree polynomial represents the non-tidal component and δ represents the random fluctuations which are neglected after smoothing. σ and φ are the angular frequency and phaselag respectively and R_t is the tidal amplitude. First order 3 hour differences give

$$\Delta U = U(t+3) - U(t-3) \qquad \ldots\ (4.02)$$

Repeating the process we obtain

$$\Delta^2 U = \Delta \{U(t+3) - U(t-3)\}$$

$$= U(t+6) - 2Ut + U(t-6) \qquad \ldots\ (4.03)$$

and substitution of (4.01) into (4.03) yields

$$\Delta^2 U = 72C - 4R \sin^2(3\sigma) \cdot \cos(\sigma t - \varphi) \qquad \ldots\ (4.04)$$

The polynomial part is thus removed and the periodic part has been multiplied by a factor of $4\sin^2(3\sigma)$. For diurnal analysis Fjeldstad recommends taking 6 hourly differences, that is, 12 hour second order differences, lunar time.

Since we perform the analysis on data resolved into two orthogonal components, we obtain the two periodic currents

$$U = M\cos\sigma t + N\sin\sigma t \qquad \text{(East component)}$$

$$V = P\cos\sigma t + Q\sin\sigma t \qquad \text{(North component)} \qquad \ldots\ (4.05)$$

It can be shown (Fjeldstad, 1964) that the coefficients M, N, P, Q determine the axes and orientation of the current ellipse. Let χ be the orientation of the major axis with respect to the x or East coordinate, then

$$\chi = \frac{\alpha + \beta}{2}$$

where

$$\alpha = \tan^{-1}\left(\frac{P-N}{M+Q}\right)$$

$$\beta = \tan^{-1}\left(\frac{P+N}{M-Q}\right)$$

The maximum velocity then occurs at time τ_{max} given by

$$\tau_{max} = \frac{\beta - \alpha}{2}$$

Finally, if

$$A = \tfrac{1}{2}\left[(M+Q)^2 + (P-N)^2\right]^{\frac{1}{2}}$$

$$B = \tfrac{1}{2}\left[(M-Q)^2 + (P+N)^2\right]^{\frac{1}{2}} \quad \ldots\ (4.06)$$

then the value of the maximum velocity is determined by $A+B$ and the minimum by $A-B$.

Suppose $M=N=P=Q$, then $A=B$ and (4.05) would describe simple harmonic motion along one plane with a maximum velocity of $2A$ and zero minimum velocity. Now suppose $M=Q$ and $P=N$, but $|M| > |N|$. This sets $A>B$ and (4.05) describes anti-clockwise motion. Finally consider $M=Q$ and $P=N$, but with $|N| > |M|$, so that $B>A$; then (4.05) describes clockwise motion. In general, using the conventions defined in (4.05) a negative value of $A-B$ defines clockwise motion, a positive value defines anti-clockwise motion.

The assumption made in representing the data by (4.01) place corresponding restrictions on the result. The phase angle must be constant during the period of observation and the non-tidal component must be of a form that can be adequately described by a second degree polynomial. It should be noted that M.D.S. during its drift south of Anticosti Island met these restrictions only very approximately at best.

Since the floe was moving throughout the period of observation the analysis for each tide was limited to successive sets of data

analysed over a time equal to three tidal periods. The tidal ellipse was then found and used to determine the tidal component at the centre of the period analysed. The entire procedure was iterated at intervals of 10 minutes corresponding to the spacing of the original data, the tidal component being deducted from the data at the mid-point, for each step. Tidal components at the two ends of the series were computed directly from the first and last tidal ellipse. Since the data was spaced in units of sidereal time, lunar hour differences were determined by weighting, in the M_2 case, hourly values from a table of length 37 sidereal hours.

4.5 - Analysis of Results

Amplitudes of the major and minor axes of the tidal ellipse computed for M_2 and K_1 are shown in Figure 4.03. Since the relationship between the co-tidal and co-range curves and the tidal stream can only be calculated in the simplest of examples (Defant, 1960), we cannot expect to predict the tidal streams from charts such as those shown in Figures 4.01 and 4.02. However, from considerations of water transports implied by the co-range lines, it would seem reasonable to expect small tidal streams close to the amphidromic point and close to the reflecting barrier of the St. Lawrence Estuary, with a maximum somewhere between. If that is the case, then the major axis of M_2 shown in Figure 4.03 would appear to bear this out, the maximum being located mid-way between Southwest Point and the Gaspé coast.

Another feature of the M_2 major axis, is the unsteady behaviour over the 16th and 17th of February. This effect is undoubtedly a consequence of the rapid change in direction and velocity during the 17th. The decrease in magnitude of the major axis during the last part

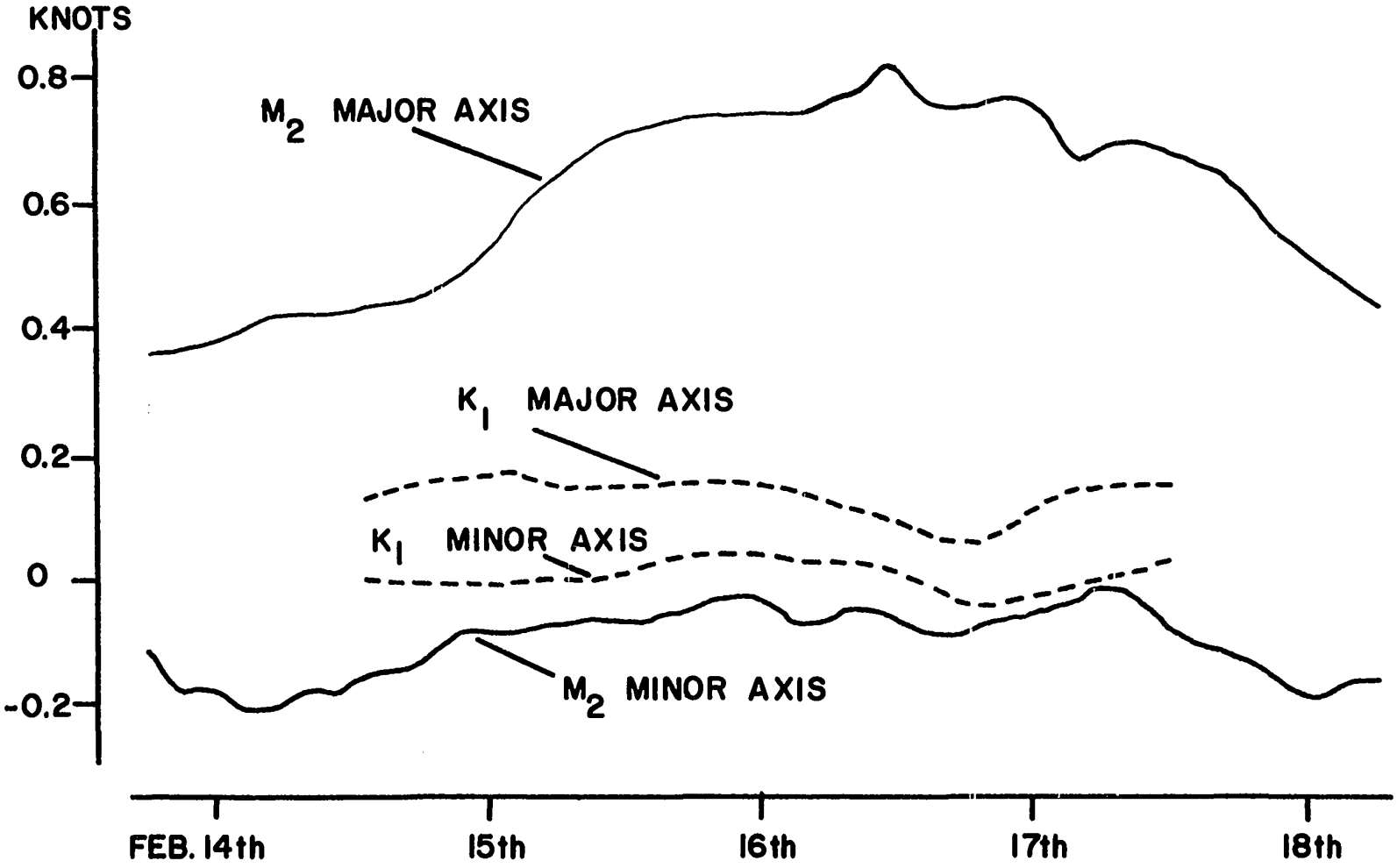

Figure 4.03 - Ellipse Parameters of Tidal Constituent M_2 and K_1.

of the observed drift must also be attributed in part to the fact that the floe was cutting the co-tidal lines at this time. Inasmuch as the different contributions to the computed ellipse were not in phase, the axes of the ellipse must be correspondingly reduced.

The major axis varies between .4 and .8 knots, somewhat higher than the mean value of .34 given by Farquharson (1966) for station 5, Figure 2.01, which M.D.S. passed at about 1200 hours on the 16th. Between 0000 hours on February 15th and 1200 hours on the 17th the minor M_2 axis is less than .1 knots. The transverse component of the oscillation only becomes significant outside the narrowest part of the Passage. Since negative values result for the minor axis, a clockwise rotation is determined for the M_2 constituent. Farquharson (1962) gives two values of major to minor axis ratios for the Passage: .36 and .19. The ratios determined for M.D.S. vary between .25 and .14.

The horizontal diurnal constituent is barely one fifth of the semi-diurnal tide which conforms to expectations based on Farquharson's results, Table 4-1. The axes are too small for variations to be considered meaningful in view of the length of the observations but it is clear that the minor axis is negligible.

The orientation of the tidal ellipse for the M_2 constituent is given for various points along the drift path in Figure 4.04. The tidal effect appears to be oriented along the coast until the floe moved past the Paspé Peninsular, when the ellipse takes on a N.E.-S.W. orientation. However, part of this effect must again be ascribed to the rapid changes in velocity undergone by the floe on February 17th.

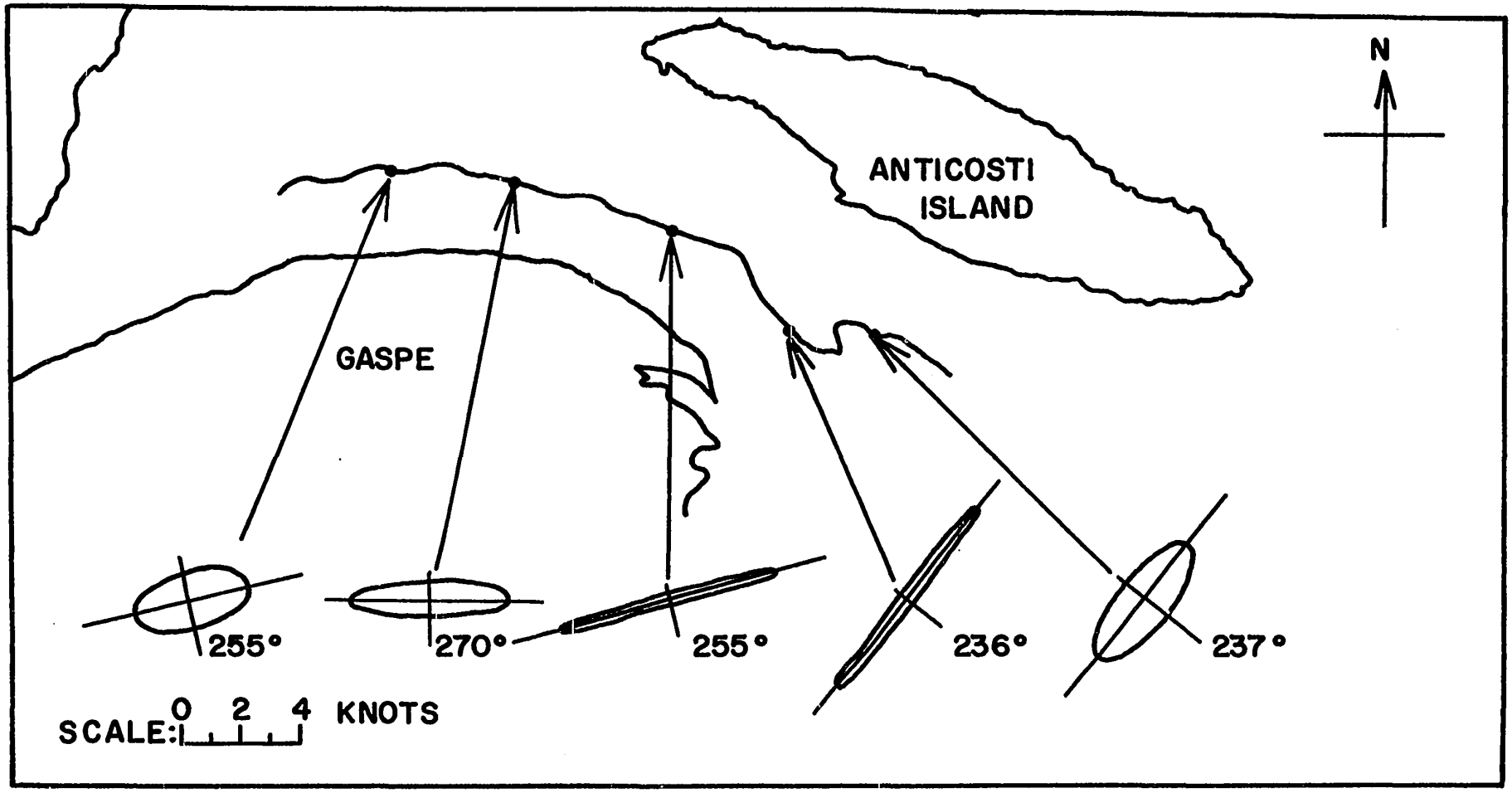

Figure 4.04 - Orientation and Ellipticity of Constituent M_2.

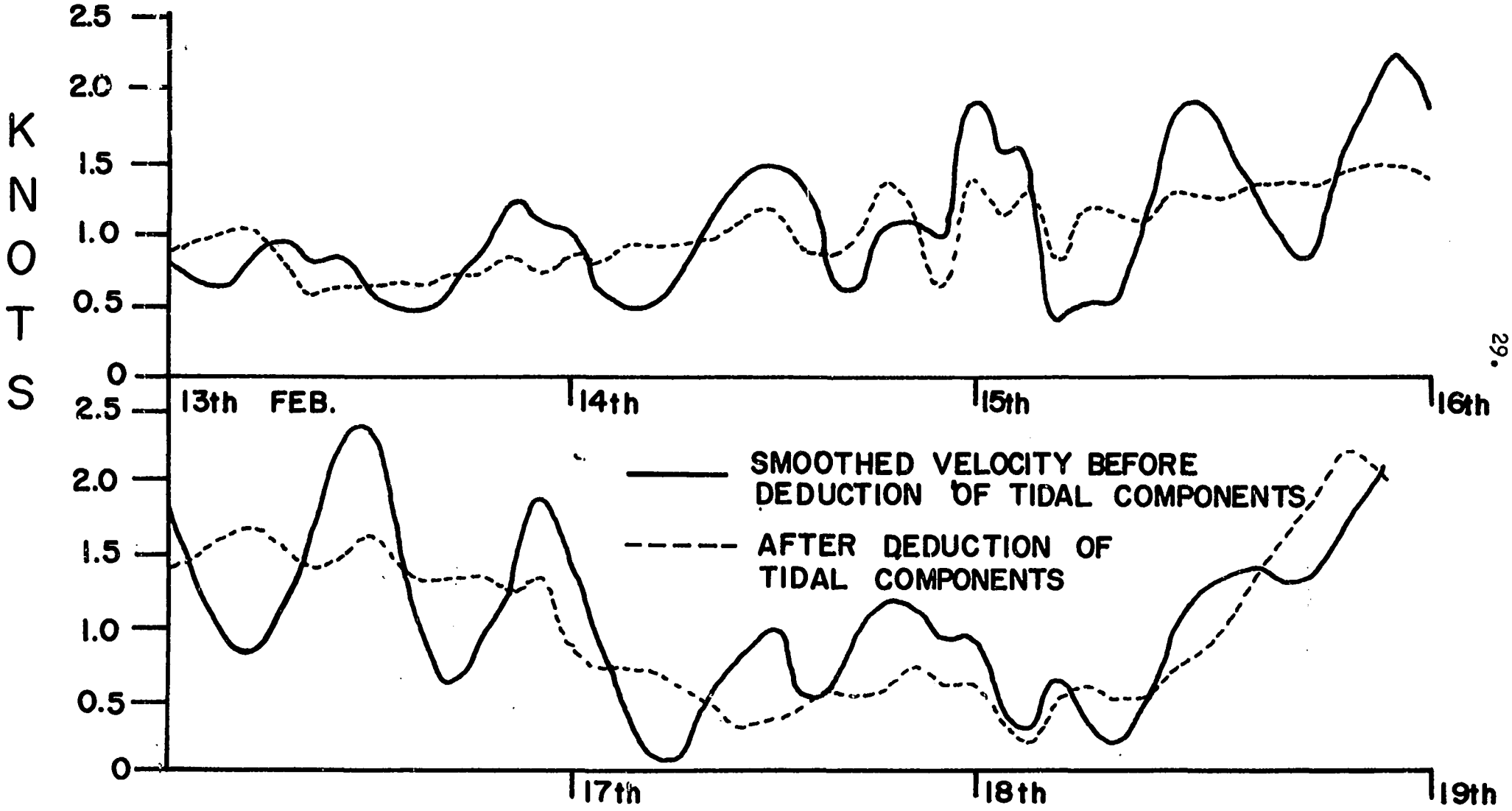

Figure 4.05 - Drift Velocity Before and After Removing Tidal Component.

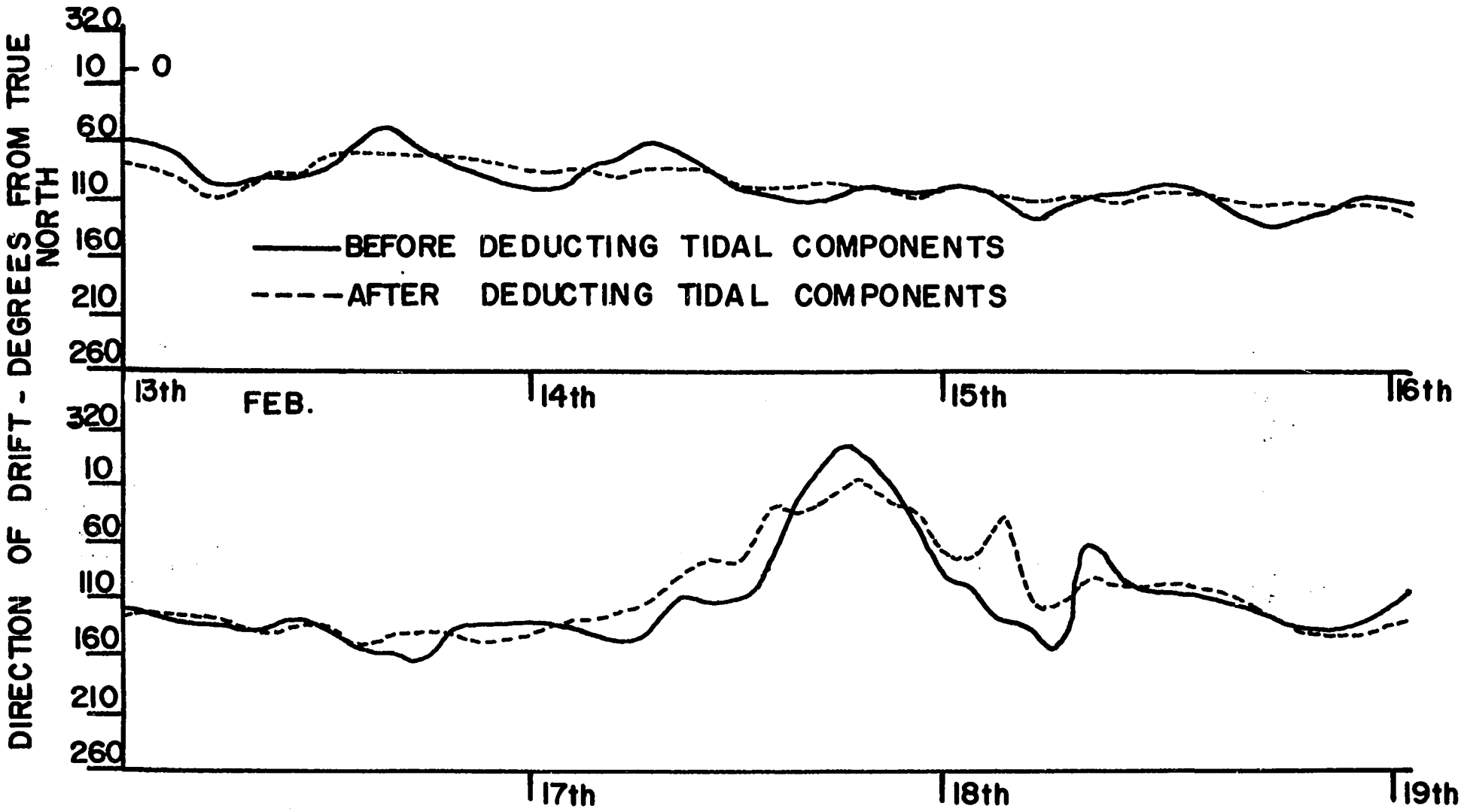

Figure 4.06- Drift Direction Before and After Removing Tidal Component.

A further complication that will not be considered here is the effect that tide-generated internal waves might have on the ice motion. The velocity data before and after deduction of the tidal component by the method outlined above is given in Figures 4.05 and 4.06. In Chapter 6 spectral analysis of the drift data is discussed and the results of this are shown in Figure 6.02, in which the peaks caused by tidal motion are clearly visible. A similar calculation on the data after the removal of the tidal component yielded a peak at the M_2 frequency of approximately one fifth the size of that shown in Figure 6.02.

Chapter 5 - Analysis of Wind-Stress

5.1 - Meteorology of observation period

The meteorological conditions over the Gulf of St. Lawrence during the drift of M.D.S. may be roughly divided into two parts. The first of these extended from February 12th until early on the 17th. During this time the wind was from the west, increasing slowly but without abrupt changes. Two low pressure areas straddled the Gulf, one over Newfoundland, the other over Quebec City. During the 15th another low moved north towards Newfoundland displacing the first, but conditions changed little over the Gulf.

The second period was one of marked variation. Late on the 16th a pressure ridge began to develop west of the Gulf. During the day the ridge became more pronounced and travelled eastwards over the St. Lawrence Estuary and out across the Gulf. Between 0600 hours and 0900 hours the ridge passed over M.D.S. The pressure distribution at that time is shown in Figure 5.01. When this happened the surface wind dropped, then swung round anti-clockwise through 100^{o}. At the same time another low started moving in from the west. Throughout the rest of the 17th the wind increased in velocity turning still further in the same direction until early on February 18th. By this time the low that had moved in from the west stood over the western end of the Gulf. During the 18th it moved north over Anticosti Island towards Labrador where it stayed throughout the 19th and 20th leaving strong westerlies in its wake, with estimated geostrophic velocities exceeding 100 knots on one occasion. Finally, during the 21st and 22nd the low over Labrador moved west spreading out over the Gulf as it travelled.

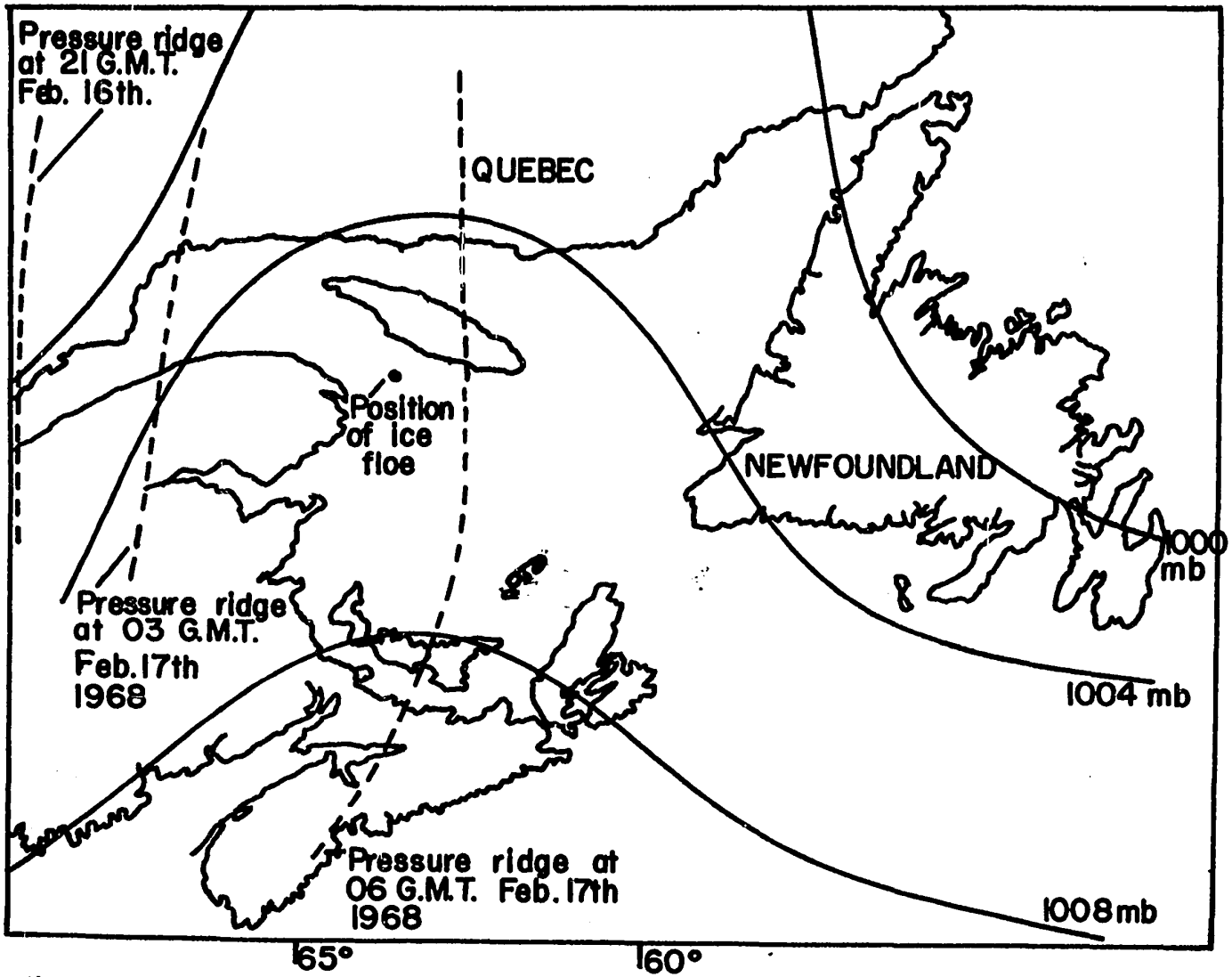

Figure 5.01 - Pressure Map for 0600 hrs February 17th Showing Movement of Pressure Ridge. (From D.O.T. Surface Pressure Chart)

5.2 - The relationship between geostrophic wind and surface stress

Any day-to-day attempt to predict the movement of ice over a large region must utilise data from synoptic pressure maps in order to estimate surface wind-stress. From the recorded pressure distribution it is possible to determine the velocity of the frictionless geostrophic wind, which always tends to blow along the isobars at a velocity determined by the equation

$$u_g = -\frac{1}{\rho f}\cdot\frac{\partial p}{\partial y}$$

$$v_g = \frac{1}{\rho f}\cdot\frac{\partial p}{\partial x}$$

where u_g , v_g are the geostrophic velocities in the x, y directions respectively, ρ is the air density, $\frac{\partial p}{\partial x}$ and $\frac{\partial p}{\partial y}$ the x and y components of the horizontal atmospheric pressure gradient, and f is the Coriolis parameter defined by $f = 2\Omega \sin\theta$, Ω being the angular velocity of the earth. In the event of significant centripetal acceleration occurring due to the curvature of the isobars the equations cease to be valid. Approximations suitable for such situations have been developed by Haurwitz (1936).

In practice meteorologists use standard scales for reading the geostrophic wind direct from the pressure maps. These scales must be prepared for the type of chart on which the curves are drawn, including a correction for the map distortion factor, and are calibrated for latitude and the distance between successive pressure curves. A scale calculated for the typical Gulf latitude of 49°, for use with a 1:5,000,000 polar stereographic projection true at 60° North with pressure lines 4 mb apart is given in Figure 5.02. The direction of

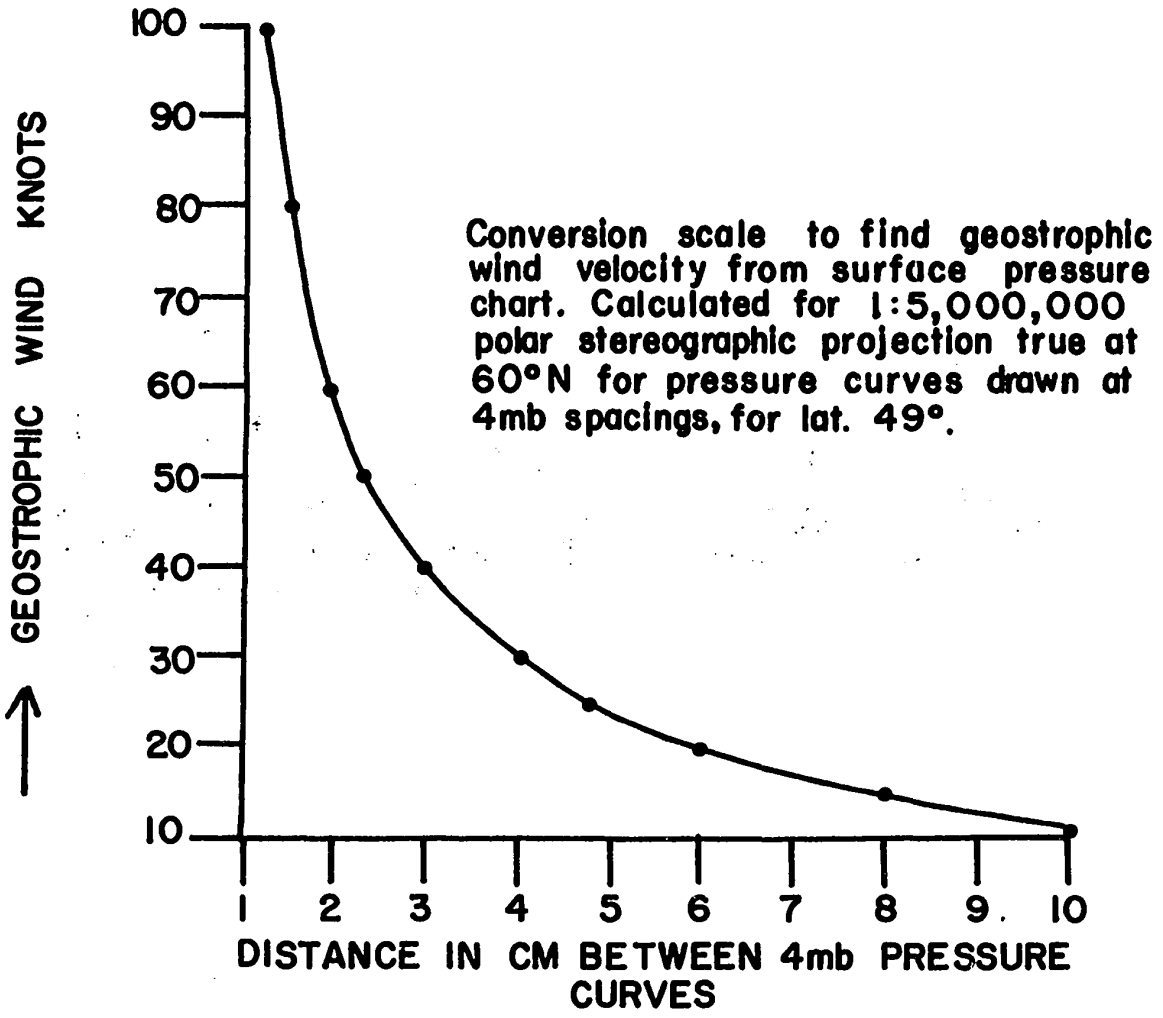

Figure 5.02 - Scale for Determing Velocity of Geostrophic Wind from Pressure Maps.

the geostrophic wind is taken to be along the isobar at the point measured, to the right in the Northern hemisphere for a negative pressure gradient. It is also possible to use finite differencing techniques such as that given by Blackford and Tsang (1964); however, it is perhaps questionable whether such a method actually gives more precise values over an area like the Gulf of St. Lawrence where pressure curves must be estimated from stations some distance from the point at which the gradient is required.

Estimating the surface stress from the geostrophic wind is a much harder problem. It is necessary to integrate the equations of motion from the surface to the geostrophic wind level. If the pressure gradient is constant with height and the wind is unaccelerated, the surface wind stress exactly balances the Coriolis force so that the linearised equations become

$$f(V_z - V_g) + \frac{d}{dz}\left[K_m \frac{d}{dz}(U_z - U_g)\right] = 0$$

$$-f(U_z - U_g) + \frac{d}{dz}\left[K_m \frac{d}{dz}(V_z - V_g)\right] = 0$$

.... (5.01)

where U_z, V_z are the x, y components of wind velocity at height z and K_m is the kinematic eddy viscosity at this height. Integration of equations (5.01) requires knowledge of the vertical distribution of eddy viscosity. The problem has been attacked under various assumptions. Ekman (1905) and Taylor (1915) took K_m to be uniform with height, Kohler (1933) assumed it to increase by some power of the height and Rossby and Montgomery (1935) combined a

a Prandtl-type boundary layer with a logarithmic spiral solution. Ellison (1956) assumed K_m to be of the form

$$K_m = k_0 U^* z$$

where U^* is the surface friction velocity and k_0 the von Karman constant.

The most satisfactory analysis appears to be that given by Blackadar (1962). Following a suggestion of Heisenberg (1948) he assumed

$$K_m = \epsilon^{1/3} l^{4/3}$$

where l is a typical eddy length and ϵ is the rate of dissipation of turbulent energy defined by

$$\epsilon = K_m \left[\left(\frac{du}{dz}\right)^2 + \left(\frac{dv}{dz}\right)^2 \right]$$

Using the results of Lettau (1950) and Panofsky and McCormick (1960), he assumed l to be related to height by the relationship

$$l = k_0 z (1 + k_0 z/\lambda)$$

where λ is the value of l in the free atmosphere. In a neutral atmosphere λ is related to the Surface Rossby Number V_g / f and empirical studies show that

$$\lambda = .00027 V_g / f$$

Blackadar integrated (5.01) numerically using these relationships and obtained a curve relating U^*/V_g to $V_g / f z_0$ and also a curve relating the cross-isobar wind angle α_0 to $V_g / f z_0$, where z_0 is the surface roughness parameter. The concept of a roughness parameter is widely used in discussions of the frictional coupling

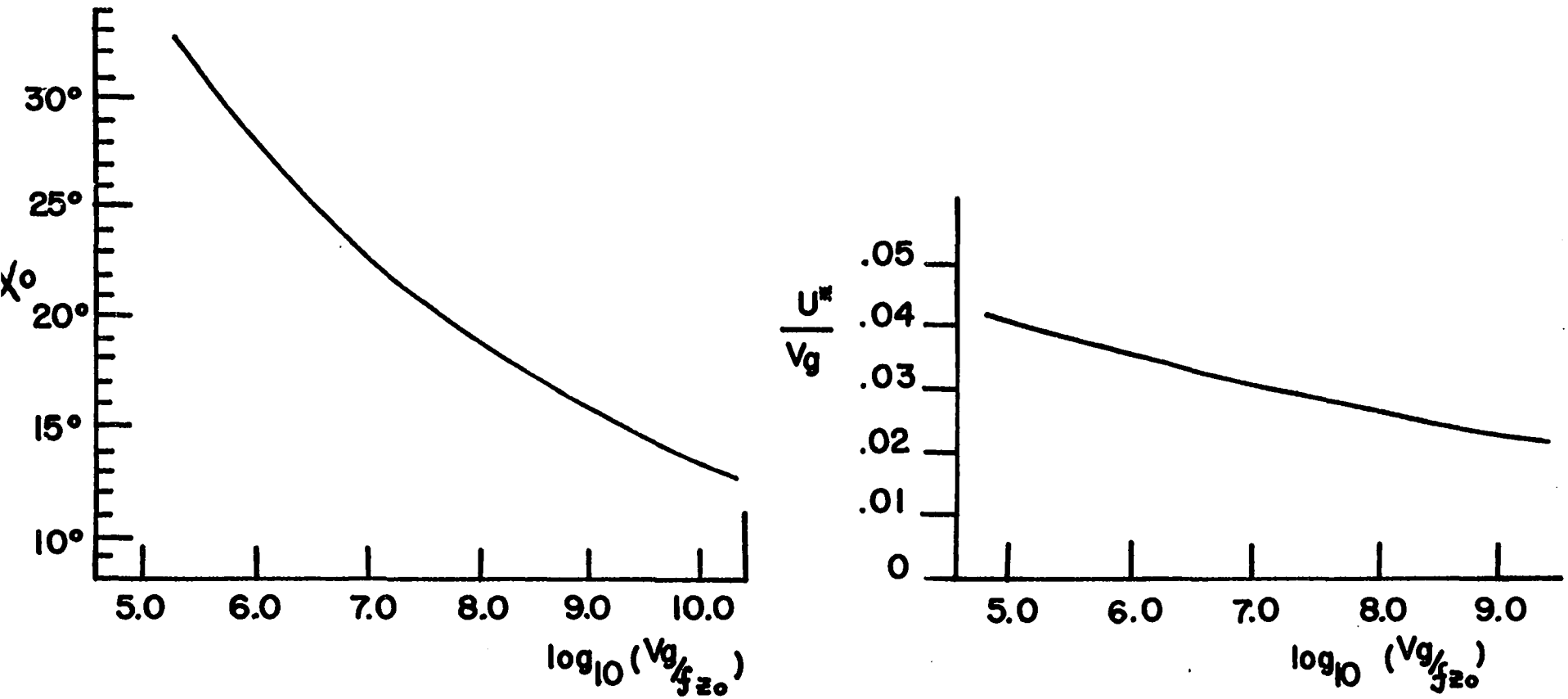

Figure 5.03 - Relationship Between Geostrophic Wind and Surface Stress (Blackadar, 1962).

between fluid and solid surface. Its value is generally determined by its effect on the fluid's velocity profile rather than direct measurement, but in general it appears to have a value of approximately $1/30$ that of representative features on the solid surface. Both of the curves found by Blackadar are shown in Figure 5.03.

The variation of cross-isobar angle α_o with stability has been discussed by Frost (1948) who found that

$$\alpha_o = \frac{p}{p+1} \cdot \frac{\pi}{2}$$

where p occurs in the expression Frost had assumed for the distribution of eddy viscosity:

$$K_m \propto p z^{1-p}$$

He found that p varied between $1/2$ for high stability and $1/10$ for low stability, giving cross-isobar angles of 30° and 8° respectively.

5.03 - Analysis of results

Surface and geostrophic wind velocities and direction over M.D.S. are shown in Figures 5.04 and 5.05. The geostrophic wind data was scaled directly from 1:5,000,000 Department of Transport atmospheric pressure maps. Geostrophic wind values from February 19th must be considered with caution since no position data was then available. Positions were linearly interpolated between the 19th and the pick-up date, February 22nd. The author is indebted to J. Walmsley who kindly supplied nearly one half of the geostrophic values shown.

In order to compare the anemometer readings with the geostrophic values smoothing of the surface wind data were required. The procedure used was to fit the data with the orthogonal polynomials described earlier using least squares criteria. 12-hour periods were

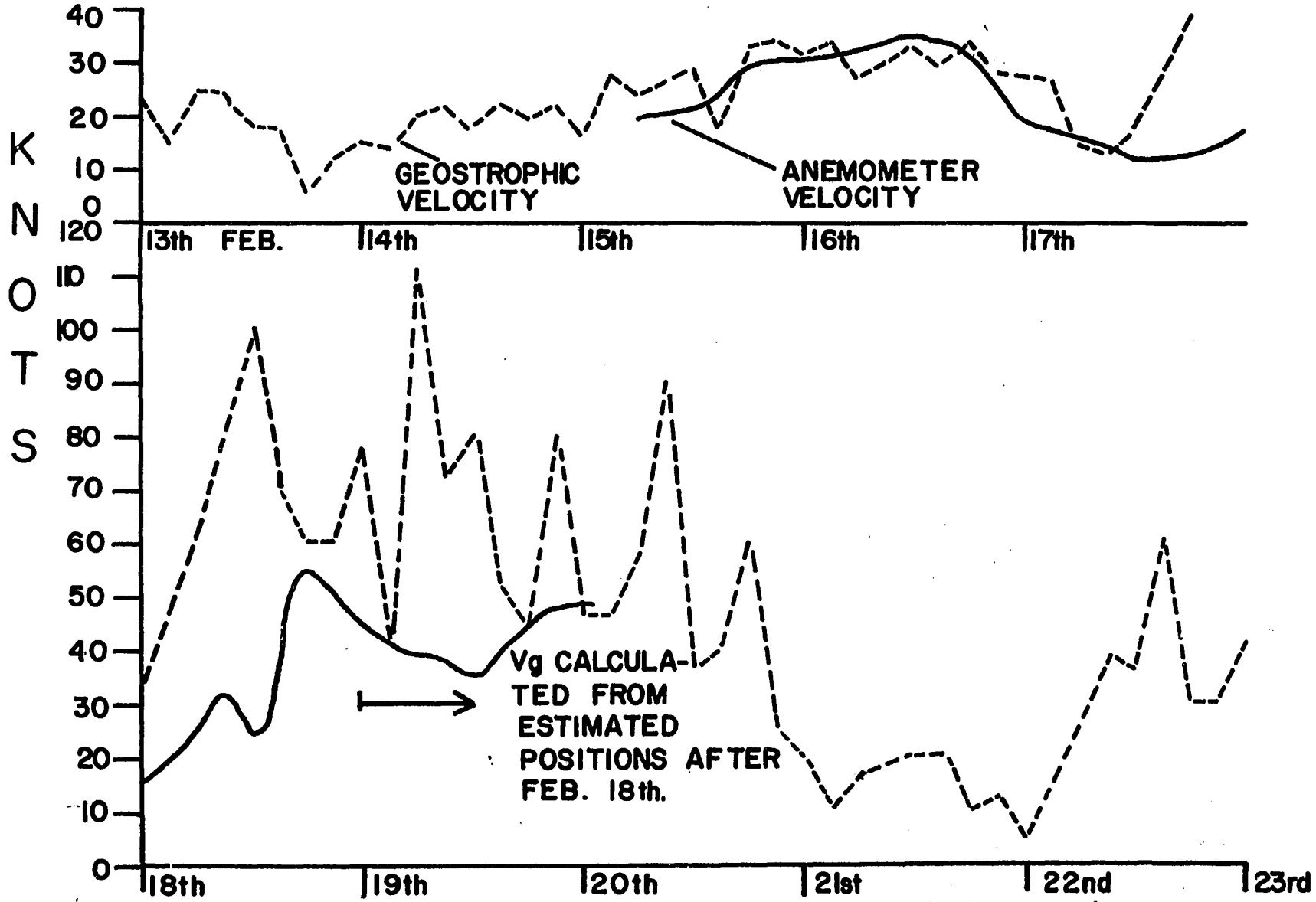

Figure 5.04 - Estimated Geostrophic Wind Velocity and Smoothed Anemometer Velocity Data.

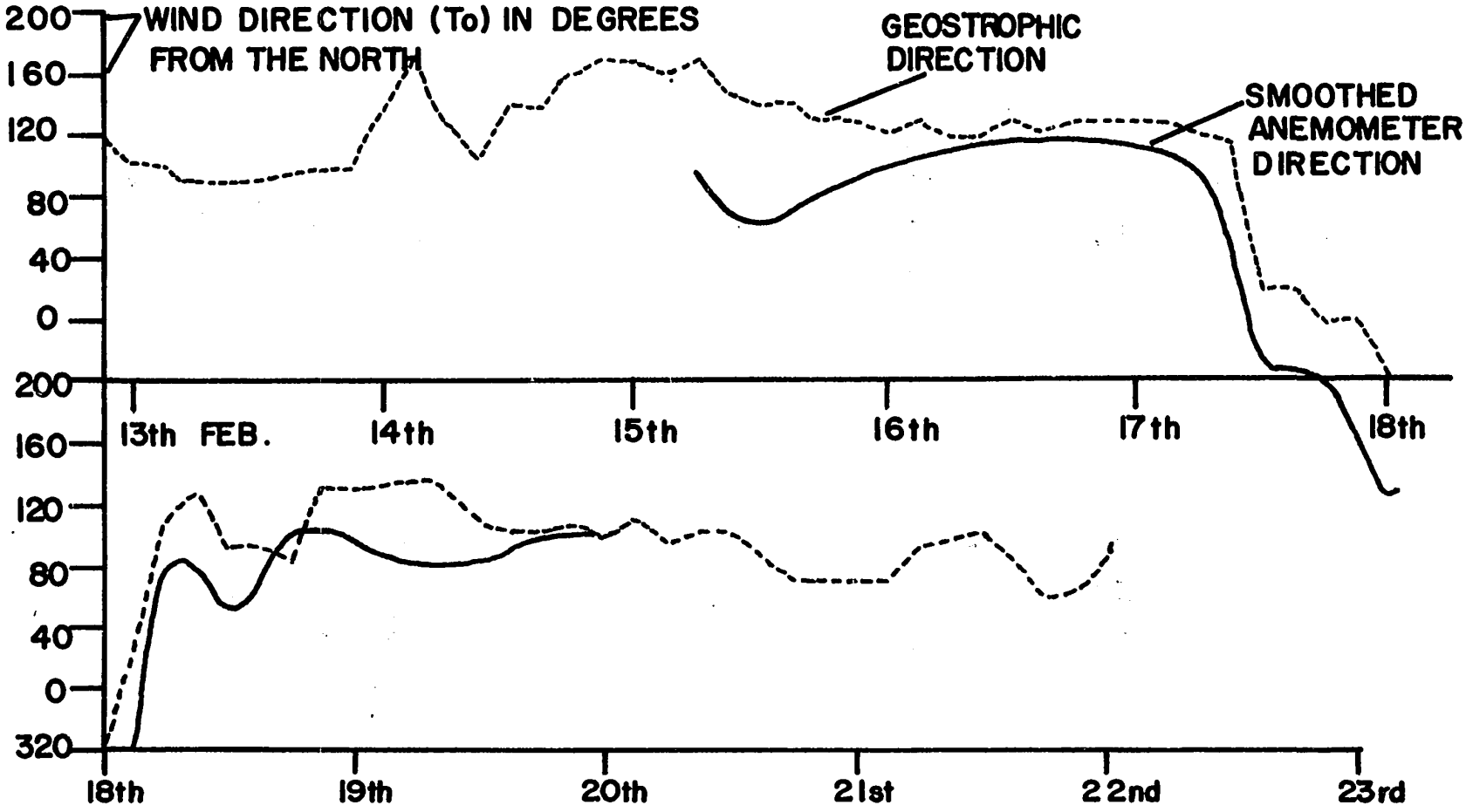

Figure 5.05- Estimated Geostrophic Wind Direction and Smoothed Anemometer Direction Data

taken in 6-hourly increments with a 3-hourly overlap at each end, polynomials of maximum degree 3 being fitted for each period.

It is clear from Figures 5.04 and 5.05 that the surface wind does follow the estimated geostrophic velocity and direction to some extent. In general the surface wind deviates to the right of the geostrophic wind and the surface velocity is smaller, though this does not hold in all cases. The rather poor agreement over the 19th may be partly due to an incorrect estimate of the position. It must also be pointed out that since the anemometer stopped working before being picked up there is no check on the accuracy of the timing mechanism.

The relationship between surface and geostrophic velocity and direction obtained from the anemometer and pressure maps was analysed statistically. These results are given in Table 5-01. They show that a very much higher correlation exists between directions than between velocities. However, the correlation between Geostrophic velocity and angle of deviation, denoted α_o , is negligible. The mean surface deviation was 40° to the left of the geostrophic direction with a standard deviation of 29°. A linear regression between the geostrophic velocity and the percent reduction in velocity represented by the surface wind and denoted by R was made and the result is given in Figure 5.06.

In an attempt to obtain more meaningful relationships a statistical analysis was made of 95 on-shore winds measured at meteorological stations around the Gulf during the period that M.D.S. was under observation. The standard meteorological station measuring height is 10 meters. The author is again indebted to J. Walmsley for

TABLE 5-01

LINEAR REGRESSION ANALYSIS OF WIND DATA

1. Geostrophic & Surface Winds (3 m. ht.) over M.D.S.

Dependent Variable	Independent Variable	Correlation %	Null * Hypothesis
Geostrophic Velocity	Anemometer Velocity	53	5
Geostrophic Velocity	R (% Reduction)	53	5
Geostrophic Direction	Anemometer Direction	92	.5
Geostrophic Velocity	α_o (Deviation)	4	>10

2. Geostrophic & Surface Winds (10 m. ht.) from Met. Stations

Dependent Variable	Independent Variable	Correlation %	Null * Hypothesis
Geostrophic Velocity	Anemometer Velocity	67	<.5
Geostrophic Velocity	R	51	<.5
Geostrophic Velocity	α_o	27	2.5
Geostrophic Velocity(only values 20 knots considered)	Anemometer Velocity	43	<.5
Geostrophic Velocity (")	R	36	1
Geostrophic Velocity(only values 30 knots considered)	Anemometer Velocity	31	5
Geostrophic Velocity (")	R	28	10

* % Significance level at which we may reject the hypothesis that the variance accounted for by regression is more than could reasonably be accounted for if all true regression coefficients were zero.

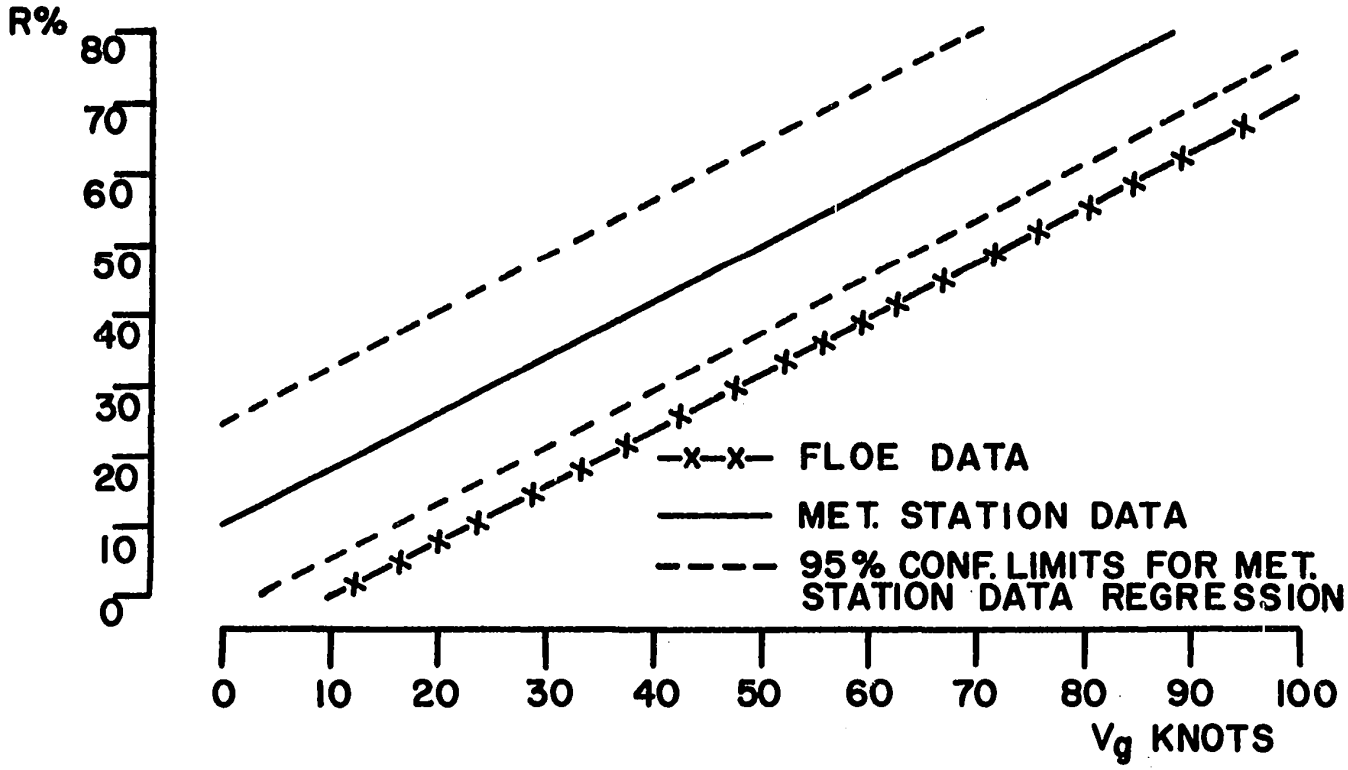

Figure 5.06 - Regression of Geostrophic Wind Velocity on % Reduction at Surface.

supplying the data. The purpose in selecting on-shore winds was to reduce local topographic effects; it was further hoped that the frictional effects of the ice-surface on the geostrophic wind might be fairly representative of that surrounding M.D.S. The limitations of this sort of analysis are appreciated, but it should be emphasized that attempts to predict ice motion in this area must always rely heavily on data collected from stations around the Gulf, and it is therefore important to learn how to use this data.

The intention in this analysis was to seek simple, empirical relationships between the geostrophic speed and the two parameters necessary to deduce surface wind: the deviation angle and the percent reduction in velocity. Regression was limited to first degree since there seemed little point in fitting second or higher degree curves to such scattered and limited data. The results are given in Table 5-01. Reasonable correlation was found between the geostrophic velocity and percent reduction at the surface but the direction data is too scattered to provide a useful relationship between geostrophic velocity and deviation. Attempts to obtain better correlations by neglecting lower velocities, which are harder to estimate accurately from the pressure maps, were not successful.

The regression curve relating geostrophic velocity and percent reduction is plotted in Figure 5.06 together with 95% population confidence limits for the standard error of estimate. That the slope is almost identical to that found for the floe data can only be regarded as coincidental. However, it is perhaps worth noting that the meteorological station curve is shifted upwards from the floe data regression line, that is, towards higher values of R for each geostrophic velocity. This result may be explained by the

topographical influence near the meteorological stations. Even though the analysis was restricted to on-shore winds, many of the stations are situated several miles inland and local topography can be expected to decrease the surface wind despite the slightly greater height at which it is measured, thus shifting the regression curve upwards.

Using the curves given in Figure 5.03 by Blackadar (1962), we may consider the following example. Let the geostrophic wind V_g be 60 knots, the latitude 49° and the upper ice surface roughness z_o be .02 cm corresponding to the value given by Untersteiner and Badgley (1965). Then

$$\log_{10}\left[\frac{V_g}{fz_o}\right] = \log_{10} 1.41\times 10^{9} = 9.15$$

If we assume neutral stability and use Figure 5.03 we obtain

$$\frac{U^*}{V_g} = .023$$

But since

$$U^* = k_o W / \ln\left[\frac{z+z_o}{z_o}\right]$$

where $k_o = .4$ is von Karman's constant and $z = 300$ cm is the M.D.S. anemometer height we have

$$W = .023\times 7.65\times 10^{3}\times \ln\left(\frac{300}{.02}\right) = 1700 \text{ cm/sec or } 33 \text{ knots}.$$

This represents a geostrophic to surface velocity reduction of 45% which is not too far off the 40% given by the regression curve in Figure 5.06. The data were too scattered to permit a comparison of predicted and measured cross-isobar angle.

Finally, an antocorrelation analysis performed on the surface wind data showed that there was no dominant frequency of wind gusts.

Chapter 6 - Statistical Analysis of Wind Drift

6.1 - Transient Response

The drift velocity and direction is shown in Figures 3.05 and 3.06. Apart from the tidal component and a fluctuation shortly before February 15th, M.D.S. drifted at a gradually increasing speed until the 16th. Early on the 17th the wind dropped and shifted. The abrupt change in direction is clearly indicated in Figure 3.06. On the 18th the floe drifted E.S.E. again at a rapidly increasing velocity.

The strongly transient characteristics of the drift pattern provide an opportunity for determining the response of the ice to a change in the wind-stress. Wind velocities were compared throughout the drift period with drift velocities for different lag times in steps of ten minutes. Drift velocities after deduction of the tidal component were used; both wind and drift velocities were normalised before comparison. Normalisation was carried out by using the transformation:

$$X'_i = \frac{X_i - M_n}{S.D.}$$

where M_n = the Mean of the series

S.D. = the Standard Deviation

and the prime denotes the transformed variable. Thus the standard deviation of each series is set equal to unity, and the means coincide.

The correlation was sought for successive lag steps using the relationship given by Blackman and Tukey (1959):

$$C_j = \frac{1}{n-j} \sum_{i=1}^{n-j} \left(W_i - \frac{1}{n} \sum_{i=1}^{n} W_i\right)\left(D_{i+j} - \frac{1}{n} \sum_{i=1}^{n} D_i\right)$$

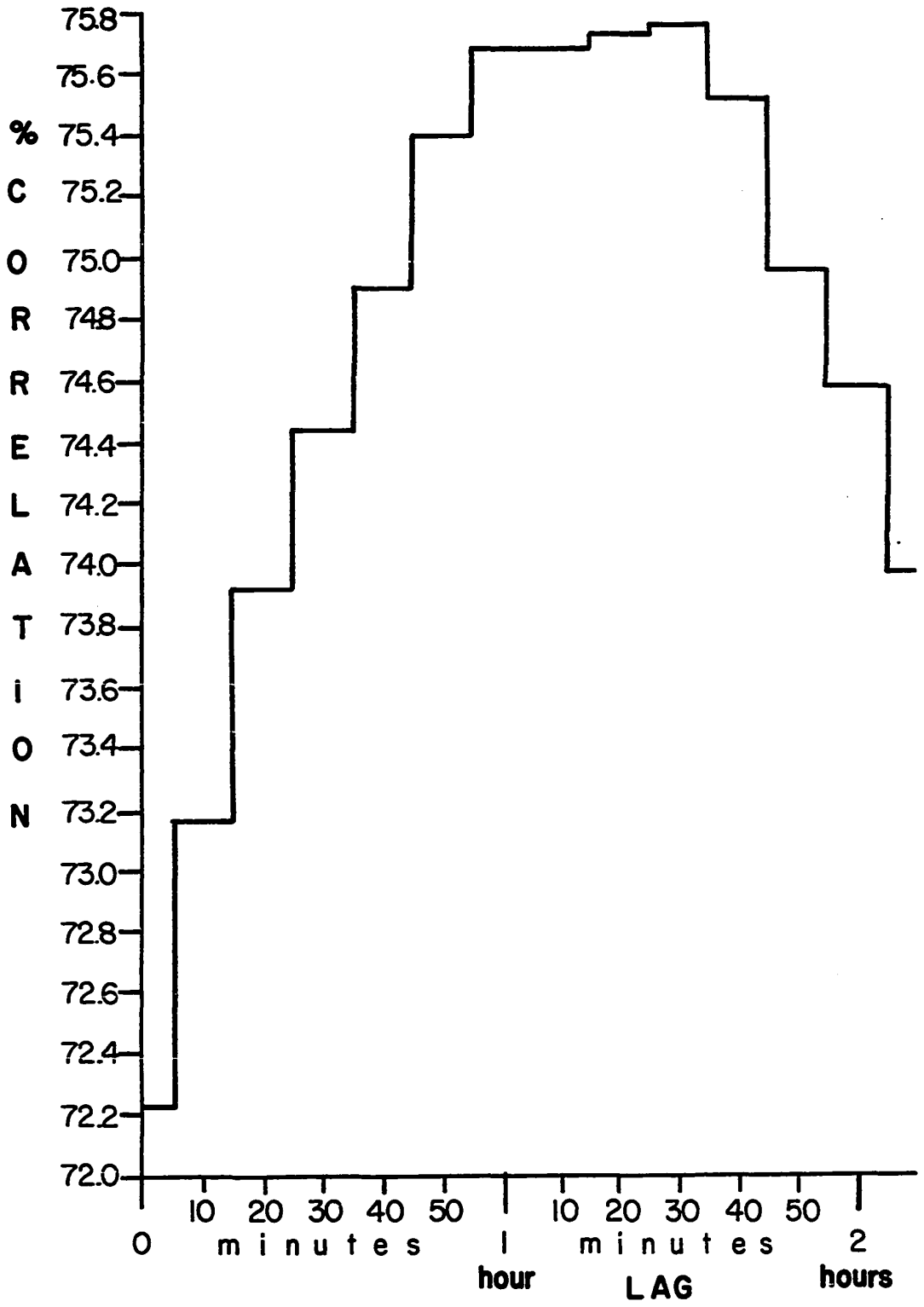

Figure 6.01 - Cross-Correlation of Normalised Drift Velocity Lagging Normalised Wind Velocity.

where,

c_j = cross-correlation for lag j.

n = number of observations in each series

j = 0, 1, 2, 3, ... represents lag steps of 0, 1, 2,... etc.

W_i, D_i = i^{th} absolute value of wind and drift velocities respectively.

The results of this analysis are given in Figure 6.01. From this it is seen that a 76% cross-correlation is achieved in less than two hours. The rapid decrease after this point must be attributed to the continual variation of the wind. Since the wind rarely blows in the same direction and at the same speed for very long, the floe drift can only be correlated with recent wind conditions.

6.2 - Spectral Analysis

If the drift velocity is transformed into the frequency domain it is possible to investigate the dominant drift components at different frequencies. The transformation is normally performed on the auto-correlation function of the data for successive lags (Blackman and Tukey, 1959) and this technique was used in the following analysis. A Tukey window was used and in order to analyse a wide range of frequencies with maximum resolution the data were processed in four sets using a maximum of 30 lags in each set. Minimum lag times were 5, 3 and 1 hours; for examining high frequency noise the two-minute unsmoothed data were used.

No significant peak occurred in the high frequency spectrum, which is not shown here. The 5 and 3 hour data however, clearly indicate the tidal constituent M_2, (Figure 6.02). The constituent

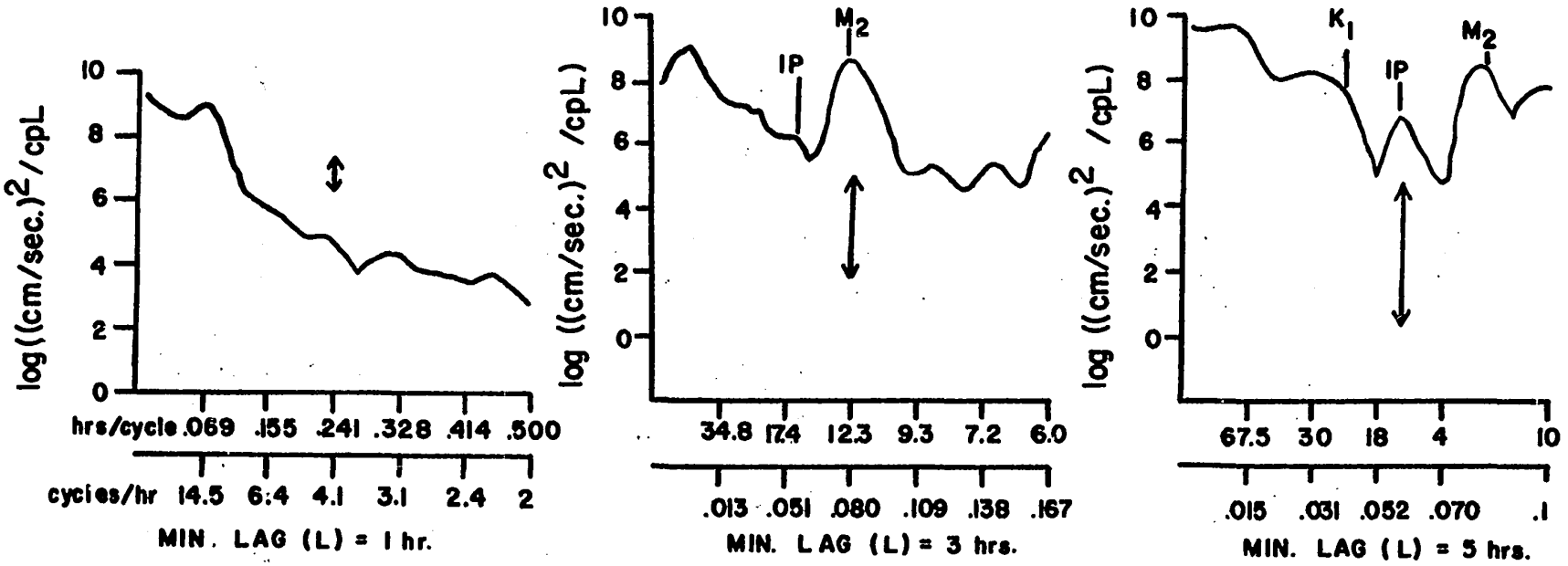

Figure 6.02 - Power Spectrum of Drift Velocity Data. (Arrows indicate 80% Confidence Limits)

K_1 is not sharply defined, but the 5 hour data do show a well-defined peak at the inertial period, marked I.P. in Figure 6.02, of 16 hours. This peak does not clearly show up in the spectrum of 3 hour data, a fact which emphasises the importance of using different decimation ratios for examining different frequencies.

Energy density is plotted on a logarithmic scale since this permits us to represent the confidence interval for the spectrum by a constant interval about the spectral estimate (Jenkins and Watts, 1968). The confidence limits on a logarithmic scale are given by

$$\log \bar{C}_{(f)} + \log \frac{d.f.}{\chi_{df}\left(1-\frac{\alpha_p}{2}\right)} \quad , \quad \log \bar{C}_{(f)} + \log \frac{d.f.}{\chi_{df}\left(\frac{\alpha_p}{2}\right)}$$

where $d.f.$ is the number of degrees of freedom appropriate to the spectral window employed, $\bar{C}_{(f)}$ is the value of the autospectra at frequency f, $100(1-\alpha_p)$ is the percent confidence required and χ_{df} is the probability distribution for the given number of degrees of freedom. Given $d.f.$ and α_p the limits each side of $\bar{C}_{(f)}$ can be found by reference to appropriate tables or graphs (Jenkins and Watts, 1968).

In interpreting the peaks shown in Figure 6.02 the confidence interval must always be considered. The inertial period is close to the minimum frequency that can be satisfactorily resolved with the length of data series used here.

6.3 - A Steady State Solution

Although the drift of M.D.S. was strongly time-dependent for most of the period in which wind velocity and ice-motion were observed, from 0000 hours to 1200 hours on February 16th may be considered a

time of sufficiently steady conditions for an equilibrium solution to be tested.

The theory used in the following analysis is that given by Reed and Campbell (1960). In this model three forces are considered: wind-stress, water-drag and the Coriolis force. The balance of these forces is shown in Figure 6.03.

In this case the wind-stress will be determined assuming a Prandtl-type boundary layer:

$$\vec{\tau}_a = \rho_a k_o^2 \left(\ln\left[\frac{z+z_o}{z_o}\right]\right)^{-2} |\vec{W}_z| \vec{W}_z \qquad \ldots\ (6.02)$$

where $\vec{W}_z$ is the air velocity vector at the anemometer height z, and z_o is the upper surface roughness parameter discussed earlier.

The Coriolis force is a "pseudo-force" arising from the use of a rotating co-ordinate system and the horizontal component is given by

$$\vec{D} = \rho_i h_i f \vec{V}_i \times \vec{k} \qquad \ldots\ (6.03)$$

where $f = 2\Omega \sin\theta$ and $\vec{k}$ is the unit vector pointing upwards, and $\rho_i h_i$ is the product of ice density and thickness.

The unusual aspect of the Reed and Campbell model is the formulation of water-stress. The theory takes account of a Prandtl-type boundary layer in which the Coriolis force is neglected and in which the vertical shear is assumed to be uniform. At the interface between

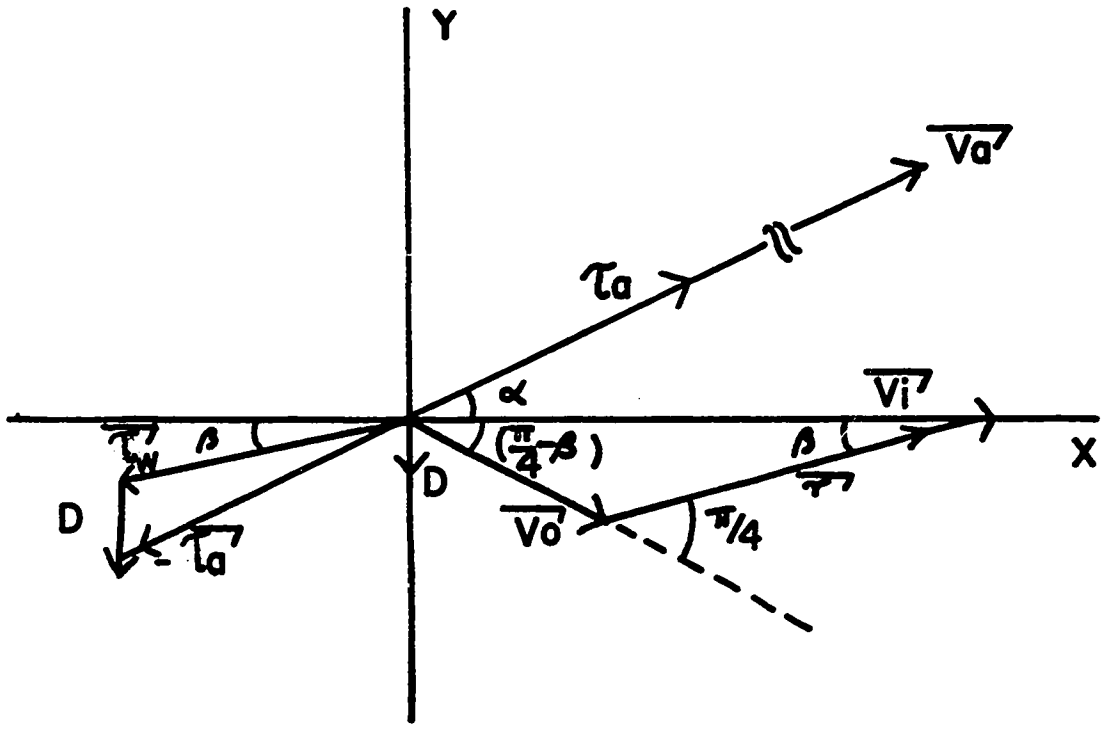

τ_a : WIND STRESS

τ_w : WATER DRAG

α : ANGLE BETWEEN WIND AND ICE VELOCITY VECTORS

β : ANGLE BETWEEN ICE AND RELATIVE VELOCITY VECTORS

Vi : ICE VELOCITY

Vo : VELOCITY OF WATER AT BASE OF BOUNDARY LAYER

τ : RELATIVE MOTION BETWEEN ICE AND WATER AT THE BASE OF BOUNDARY LAYER

Va : WIND VELOCITY

D : CORIOLIS FORCE

Figure 6.03 - Balance of Forces for Equilibrium Drift, (Reed & Campbell, 1960).

the boundary layer and the subsurface water on which the Coriolis force acts, a 45^{o} deviation in the direction of flow, to the right in the Northern hemisphere, is taken, analogous to the deflection given by Ekman's wind-driven current theory at the air-water interface (Ekman, 1965). Within the boundary layer the eddy viscosity is taken to increase linearly from the surface matching the eddy viscosity of the spiral layer at the interface, beneath which it is assumed to be constant.

The water-stress may be put in a form analogous to (6.02) if the relative velocity vector between the ice and the top of the spiral layer, $\vec{r}$ is used:

$$\vec{\tau}_w = \rho_w k_o^2 \left[\ln\left(\frac{z+z_o}{z_o}\right)\right]^{-2} |\vec{r}|\,\vec{r} \qquad \ldots. (6.04)$$

where z_o is now the roughness parameter for the lower surface of the ice.

If these forces are now resolved into x and y components and the assumptions made earlier concerning eddy viscosity are used, the following equations are obtained:

$$\tan\alpha = \tan\beta + \frac{\sqrt{2}\,B\rho_i h_i f}{\sin 2\beta}\left[\frac{\cos\beta}{\gamma_w'^{3}\tau_a\cos\alpha}\right] \qquad \ldots. (6.05)$$

$$V_i^2 = r^2 + \sqrt{2}\,B r^{5/2} + B^2 r^3 \qquad \ldots. (6.06)$$

$$\sin\beta = \left[\frac{B^2 r}{2(B^2 r + \sqrt{2B^2 r} + 1)}\right]^{1/2} = \frac{B r^{3/2}}{\sqrt{2}\,V_i} \qquad \ldots. (6.07)$$

$$\gamma_w'^{2} r^4 + 2\rho_i h_i f \gamma_w' \sin\beta V_i r^2 + (\rho_i h_i f V_i)^2 = \tau^2 \qquad \ldots. (6.08)$$

where $$B = k_o [f(H_f + Z_o)]^{-\frac{1}{2}} \left[\ln\left(\frac{H_f + Z_o}{Z_o}\right)\right]^{-\frac{3}{2}} \quad \ldots\ldots (6.09)$$

γ_w' = drag coefficient of water and is defined by

$$\gamma_w' = k_o^2 \left[\ln\left(\frac{H_f + Z_o}{Z_o}\right)\right]^{-2}$$

and H_f = thickness of boundary layer beneath ice

h_i = ice thickness

ρ_i = ice density

β = angle between $\vec{V}_i$ and $\vec{r}$

α = angle between $\vec{\tau}_a$ and $\vec{V}_i$

Reed and Campbell (1962) found solutions by substituting a range of values for r into equations (6.06) and (6.07) in order to find the relation of r to V_i and β. Substituting these values into equation (6.08) gives r as a function of τ_a. Finally, β and τ_a are substituted into (6.05) and α is found by trial and error.

Since the trial and error method of solution is very cumbersome attempts were made to solve (6.05) to (6.09) by one of the standard methods for non-linear equations; in this case the Wegstein method was tried (I.B.M., 1968 and Wegstein, 1960). However, the attempt was unsuccessful on account of the proximity of imaginary roots to the real solution. This difficulty emphasises one of the disadvantages of this model: it is not readily put into a form appropriate for application to large amounts of data.

As before we make the assumption that the upper ice roughness parameter is .02 cm conforming with that given by Untersteiner and Badgley (1965). A typical ice thickness for the time under consideration is 50 cm. The lower roughness parameter and the boundary layer thickness

are harder to estimate. The current measurements close to the ice are inconclusive, partly on account of the uncertainty over the operation of the current meter. Johannessen, Pounder et al. (1968) suggest a lower roughness parameter of 4.9 cm which seems large compared with the 2.0 cm given by Untersteiner and Badgley for arctic ice, in spite of the rather rough appearance of the ice around M.D.S. The same report suggests a boundary layer thickness of between 20 and 70 cm. In view of the uncertainty of the data and the difficulty in estimating these parameters, the following calculation must be considered with caution.

If we take the representative wind velocity and direction on February 16th between 0000 hours and 1200 hours as 120° and 32 knots respectively, and accept the following parameters,

$$z_o \text{ (upper)} = .02 \text{ cm}$$

$$z_o \text{ (lower)} = 4.0 \text{ cm}$$

$$H_f = 70 \text{ cm}$$

$$\rho_i h_i = 50 \text{ grams/cm}^2$$

$$\rho_a = 1.2 \times 10^{-3} \text{ grams/cm}^3$$

$$\rho_w = 1.02 \text{ grams/cm}^3$$

then, using trial and error methods a solution to equations (6.05) to (6.09) yields the values

$$V_i = 75 \text{ cm/sec}$$

$$\alpha = 38.7^\circ$$

corresponding to a relative velocity r of 17.0 cm/sec.

Average values observed during this period are

$$V_i = 80 \text{ cm/sec}$$

$$\alpha = 15^\circ$$

It is possible that internal ice stress accounts for the much smaller deviation angle recorded. A weak upstream current may also have been present, though this would seem unlikely in view of the sustained westerly winds prior to the 16th. It is more probable that the parameters chosen are not truly representative for this case. Nevertheless, surprisingly good agreement with the drift velocity is obtained. Accurate estimation of the deviation α has always been a difficult problem and no ice-drift theory has yet been able to handle it very satisfactorily.

Chapter 7 - The Time Dependent Motion of Sea Ice

7.1 - Introduction

The drift of sea ice has occupied the attention of oceanographers ever since the remarkable Fram expedition in the late 19th century. Early interest in this problem lay in the fact that the angle between drift and wind vectors is much less than that predicted by Ekman's theory.

The first models such as that given by Nansen (1902) concentrated on the solution of an equation relating the forces of wind-stress, water-stress and the Coriolis force. Sverdrup (1928) attempted to explain the discrepancy with Ekman's theory by including an internal ice-stress which he took to be proportional and opposite in direction to the ice velocity, but this required him to postulate much higher wind-stress values than actually exist. Rossby and Montgomery (1935) were the first to realise the importance of a boundary layer next to the ice, a concept used also by Shuleikin (1938). More recently the empirical models of Zubov (1943) and Gordienko (1958) may be mentioned, and the solution of Fukutomi (1958) appropriate to enclosed regions. Fel'zenbaum (1958) included water currents but neglected the boundary layers at the ice interfaces, a deficiency made good in the Reed and Campbell (1960) model discussed earlier. A significant departure from previous methods is that given by Campbell (1964), in which two-dimensional partial differential equations are numerically integrated on a vast scale, permitting theinclusion of surface ice interaction which Campbell represented by the Laplacian of the ice velocity.

All these theories applied to the steady-state or "quasi-equilibrium" problem in which the forces were held on average to be

in balance and the ice drifted at constant velocity in the same direction. There have, however, been a few attempts to analyse the problem of time-dependent motion. In Sverdrup's discussion of the steady-state drift of ice, there is also included an analysis of transient motion in which he integrated his equations under a few simple assumptions regarding the wind-stress. His purpose in doing this was to estimate the average effect of a wind that was gradually changing in velocity or direction. The equations investigated by Sverdrup were

$$\frac{du}{dt} = c_1 W_x - c_2 u + fv$$

$$\frac{dv}{dt} = c_1 W_y - c_2 v - fu \qquad \ldots\ (7.01)$$

where W_x and W_y are the x and y components of the time-dependent wind-stress and c_1 and c_2 are constants defining the relation between wind velocity and wind-stress and between ice velocity and the resistance to motion due to internal ice stress. Sverdrup based his assumption that the resistance to motion was dominated by internal stresses and that the water drag could be neglected on his observations of the sharp density discontinuity at 30 m. during winter months over the North Siberian Shelf. He believed this to imply a very low vertical eddy viscosity at the discontinuity so that the ice and upper water layer would slip over the lower layer as a solid mass, without friction. Moreover, the extensive ridging suggested the importance of ice-stresses.

Shuleikin (1938) also discussed transient ice motion. He

limited his analysis to a simple step-function type of wind-stress and considered two cases: a low ice velocity at which the water resistance could be neglected, and a high ice velocity at which the Coriolis force could be neglected in comparison to the water resistance. Shuleikin used these models to estimate that the ice would reach 85% of its terminal velocity within one hour of such a wind-stress beginning.

In 1930 Fjeldstad put forward a theory in which he included the resistance to motion offered by the water in addition to internal ice-stress (Fjeldstad, 1930). In this rather complicated mathematical treatment the linearised equations of motion are integrated vertically in order to determine the surface velocity. Fjeldstad included the internal ice-stress terms as they appear in equations (7.01), but neglected the mass of the ice. He thus treated the ice-water system as a homogeneous fluid, acted on by a surface wind-stress, but also subject to a surface skin resistance.

Fjeldstad's neglect of the ice mass might be justifiable if the viscosity is invariant with depth and if the accelerations are relatively small, for then the solid surface acts merely to transmit the stresses to the water beneath, which at small depth moves at a velocity nearly equal to the ice. The theory ceases to be useful if we accept the findings of Rossby and Montgomery (1935) and include a sharp change in the vertical eddy viscosity close to the surface, for then the behaviour of the ice and surface layers will be very different to the slightly deeper water. Fjeldstad's paper is nevertheless important in that it is the only time-dependent ice drift theory to date that has included the vertically integrated equations of motion; moreover, it provided a satisfactory mathematical derivation of

Fredholm's solution for wind-driven currents (Ekman, 1905), it was the first model to allow for the effects of finite depth of the ocean and it also laid the foundation for the significant contribution of Hidaka (1932) which will be discussed later, and of Nomitsu (1933) and Defant (1940).

More recently Brown and Crary (1958) considered the effect of moving air systems over an ice field and were able to measure the tilt of the surface using a sensitive bubble level. Current measurements at 150 m. in the same study suggested the existence of a counter-current tending to balance the depression. Hunkins (1967) used equations (7.01) to investigate inertial oscillations of the arctic ice-island T-3 and integrated them analytically for the case of a step-function wind-stress. Hunkins was interested in summer ice conditions with loose pack-ice and he therefore used the terms $c_2 u$ and $c_2 v$ in (7.01) to describe the water-drag effects.

Reed and Campbell (1960) took the non-linear equations

$$\frac{du}{dt} = c_1 W_x - c_2 u^2 + fv$$

$$\frac{dv}{dt} = c_1 W_y - c_2 v^2 - fu \qquad \ldots\ (7.02)$$

and integrated them numerically under a step-function wind-stress. The result is shown in Figure 7.01.

Until very recently the quality of navigation data has not permitted the study of accelerations on the scale encountered in ice studies. Another problem has been the laborious computation necessary in the use of the more complicated solutions, likely to arise in the

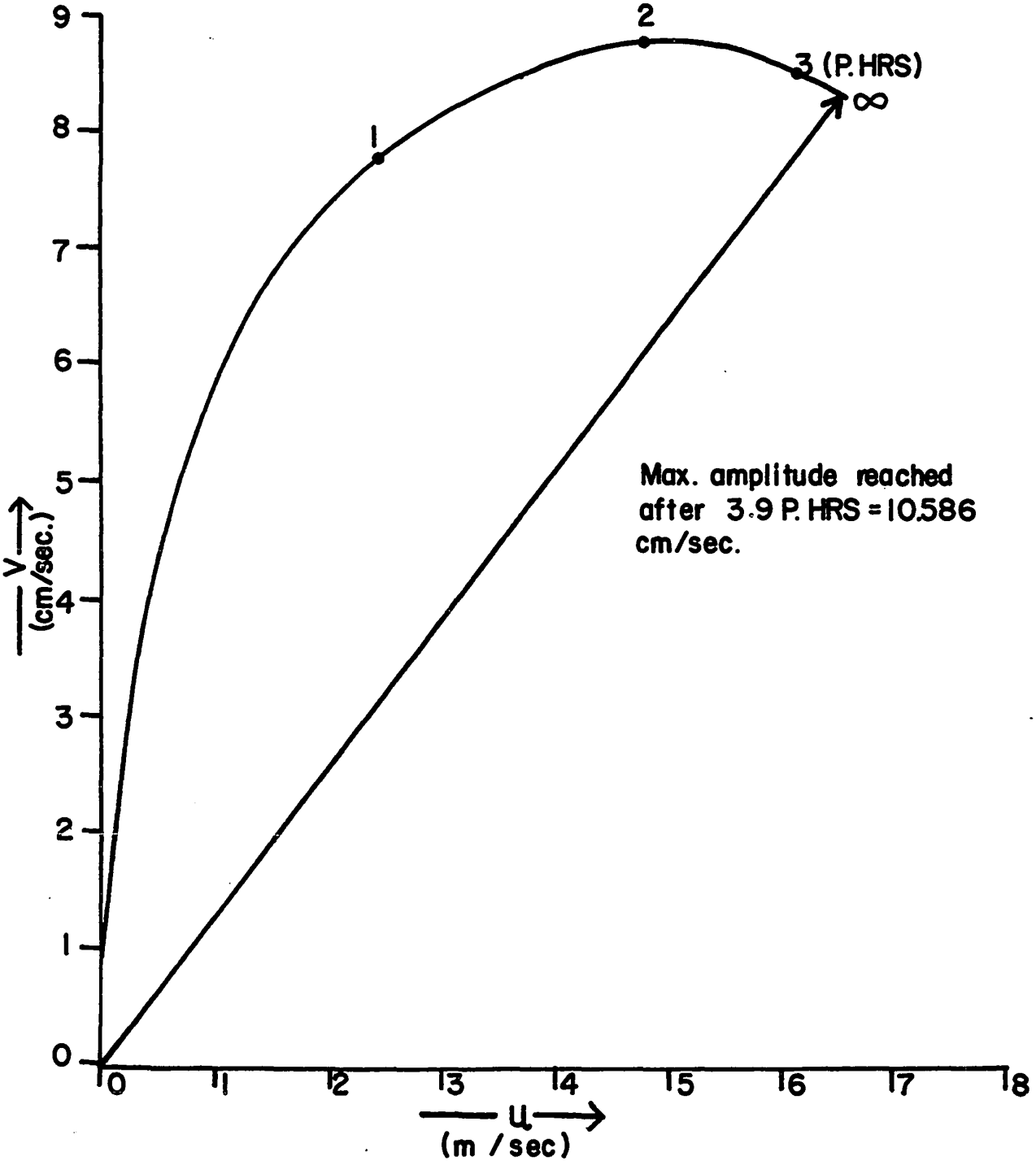

Figure 7.01 - Velocity Hodograph for Step-Function Wind-Stress (Reed & Campbell, 1960)

in the study of time-dependent motion. Improved navigation techniques and the availability of high-speed computers now permit us to analyse such models with observed data as input, rather than integrate simplified equations under the most stringent and artificial assumptions.

7.2 - Simple inertial model: Resonant Interaction and other properties

Any large water mass has certain natural periods of oscillation. In the Gulf of St. Lawrence we may expect to find a characteristic seiche frequency and also an inertial frequency determined by the latitude. Evidence of inertial motion is suggested in Figure 6.02, but even if this were not observed the forces involved are well-known and under certain circumstances may become very important.

In examining the oscillations of T-3, Hunkins (1967) found that the transient terms in his solution to (7.01) describe rotary motion with the inertial period, agreeing in general form with his observations. Rather than use (7.01) we shall consider the non-linear form (7.02) which we may rewrite as

$$\frac{du}{dt} = fv - \frac{K_w \rho_w}{\rho_i h_i} u^2 + \frac{K_a \rho_a}{\rho_i h_i} W_x^2$$

$$\frac{dv}{dt} = -fu - \frac{K_w \rho_w}{\rho_i h_i} v^2 + \frac{K_a \rho_a}{\rho_i h_i} W_y^2 \qquad \ldots\ (7.03)$$

where K_w and K_a are the water and air drag coefficients, and $\rho_i h_i$ the product of ice density and ice thickness. Figure 7.01 shows that when plotted in the u, v plane the ice velocity spirals into the equilibrium value. This is more obvious in the under-damped case shown in Figure 7.02, for a lower wind velocity and for parameters found to be realistic in the Gulf of St. Lawrence. In

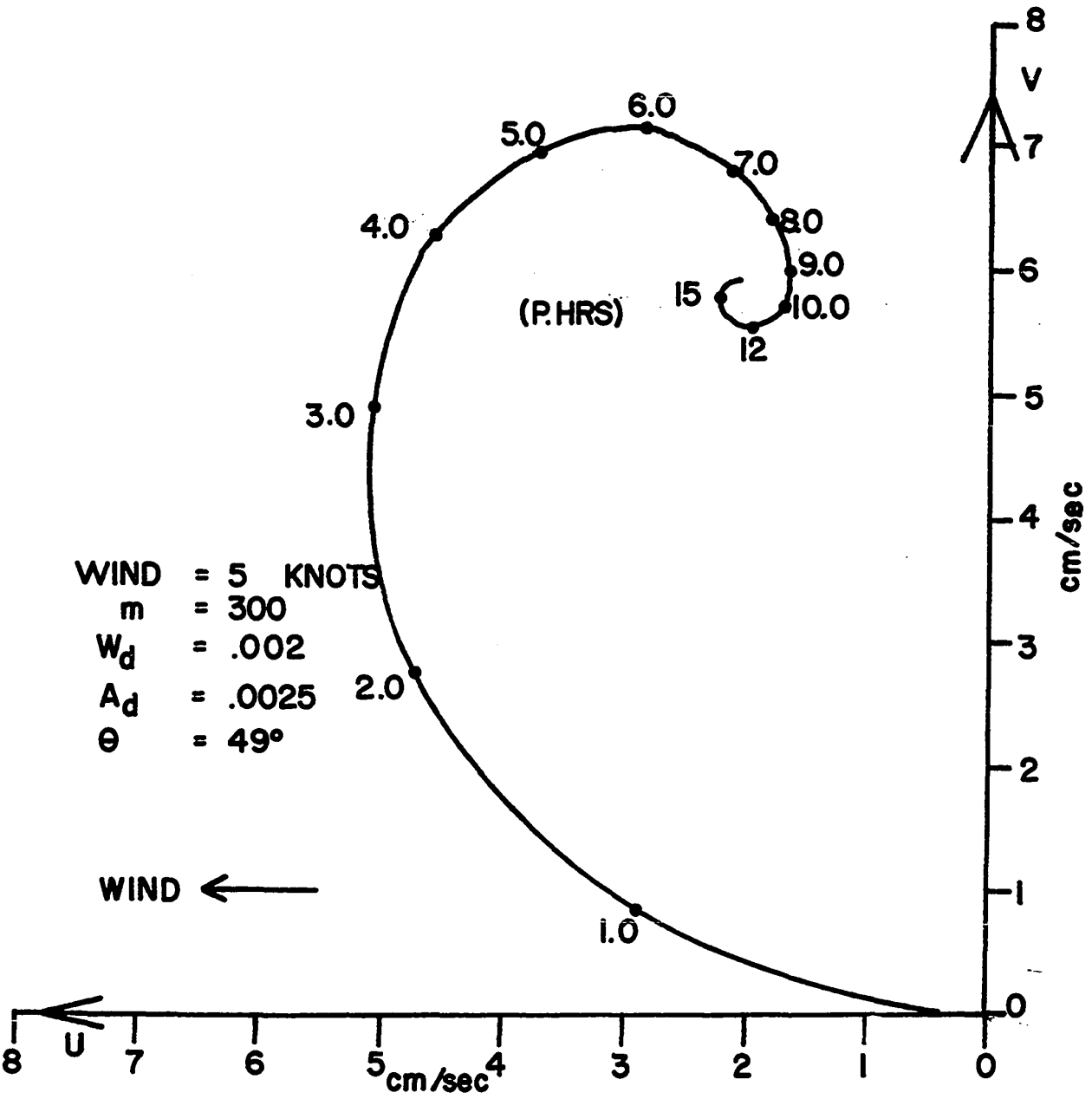

Figure 7.02- Hodograph of Ice Velocity Under Step-Function Wind Stress, Using Typical Gulf Values.

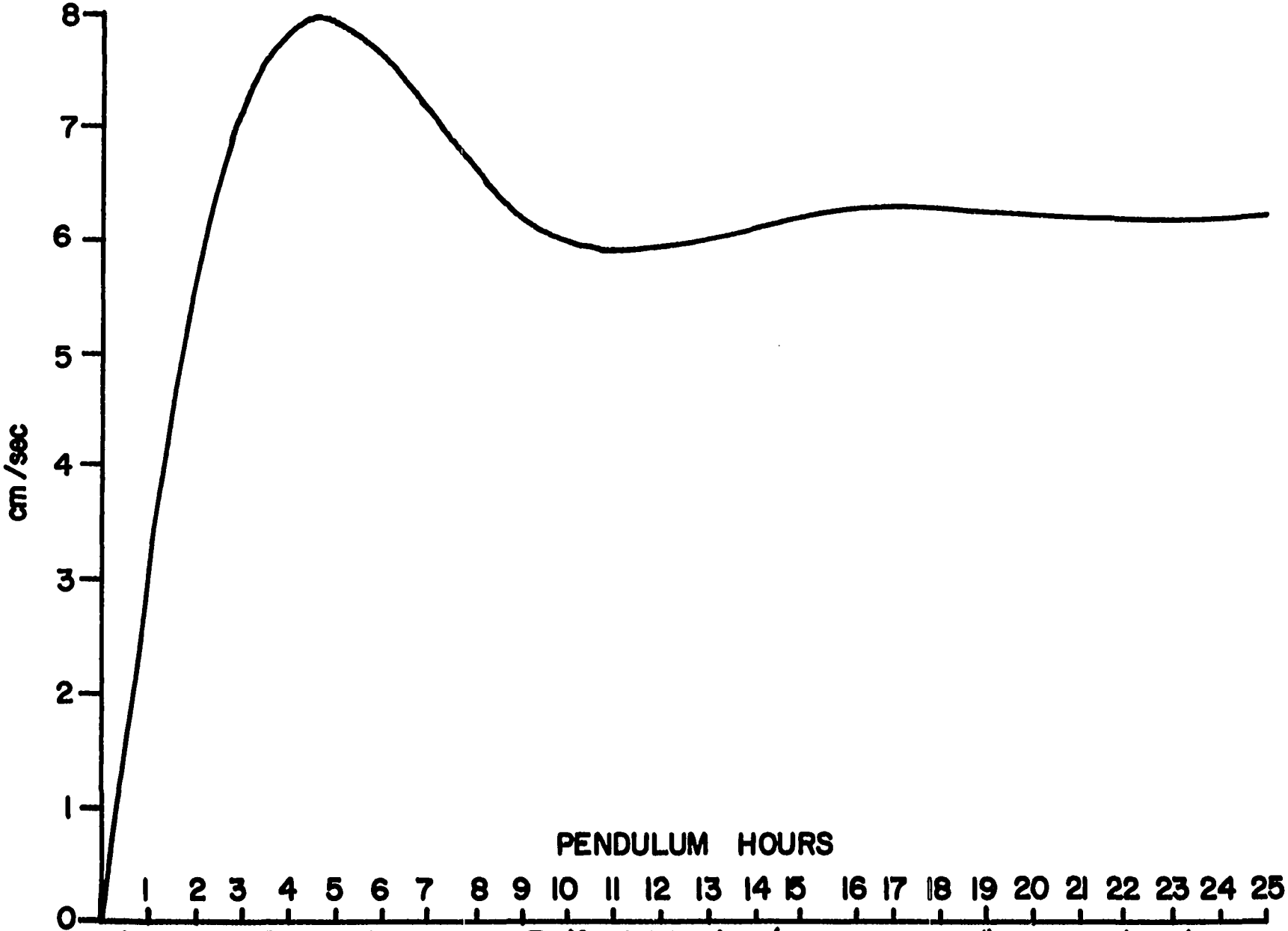

Figure 7.03 - Absolute Drift Velocity (corresponding to hodograph shown in Figure 7.02).

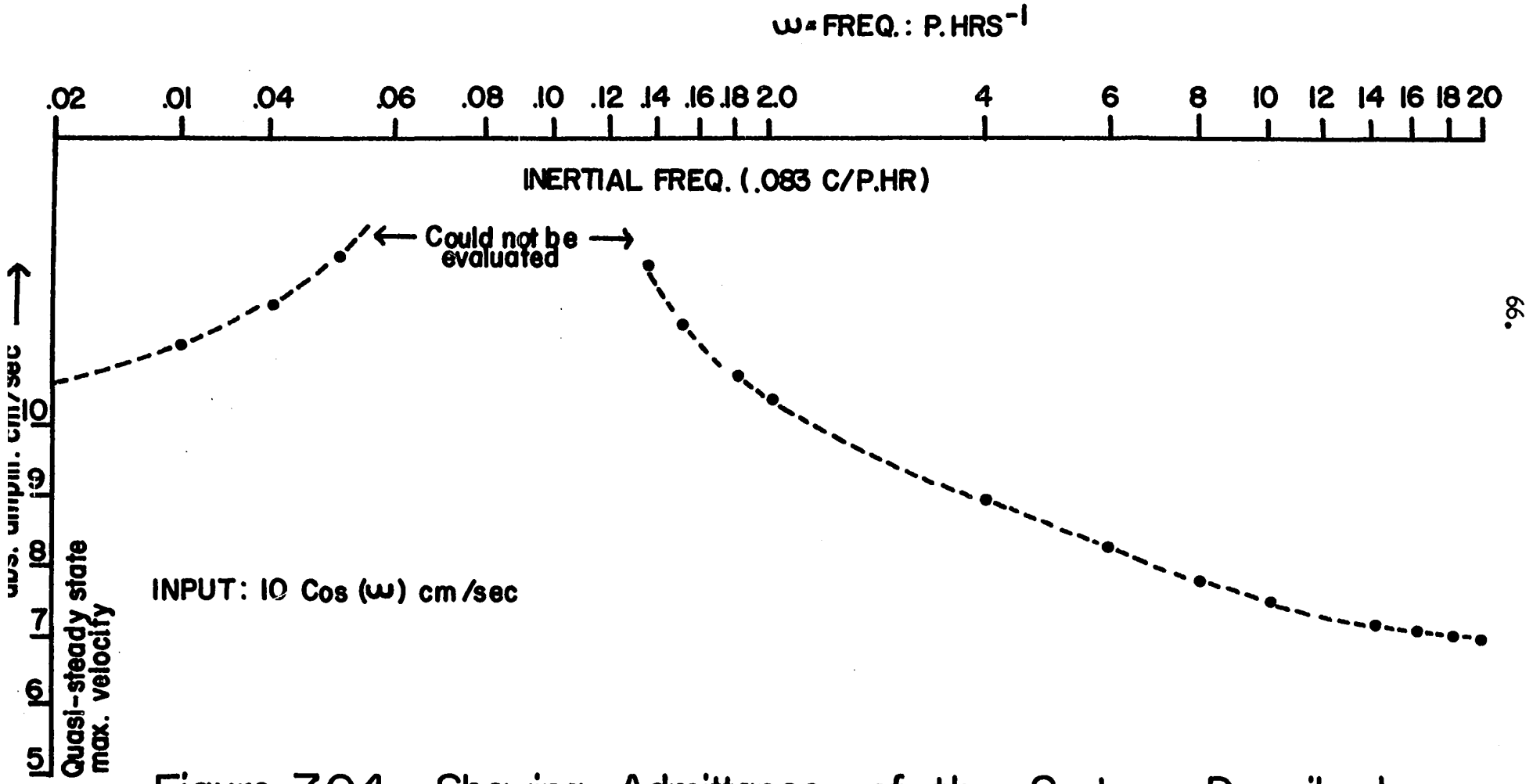

Figure 7.04- Showing Admittance of the System Described by Equations (7.02).

order to show more clearly the behaviour of solutions to (7.03) the absolute velocities for the case shown in Figure 7.02 are shown in Figure 7.03.

Since the system described by (7.03) has a characteristic periodicity, it is natural to examine its behaviour under forcing functions of different frequencies. The admittance may be estimated numerically by applying a periodic forcing function and waiting for the system to reach a state of uniform oscillation. This was done using a sine wave input and finding the amplitude of oscillation after several cycles for a range of frequencies. Figure 7.04 shows the curve determined in this way. Close to the inertial period the solution becomes unbounded.

It is clear from Figure 7.04 that if changes in the wind-stress over the Gulf are of the order of the inertial period, the inertial period at Lat. 49° is 16 hours, it is not unlikely that changes in the wind-stress could lead to amplifications in the ice-water system.

Although equations (7.03) do not allow for seiche frequencies, resonant interaction could occur here also. Finally, it should be noted that wind-stress changes in phase with the tides can also result in amplification of the surface motion.

7.3 - Application to measured wind-stress values

The facility with which equations such as (7.02) can be integrated suggest their use with measured wind-stress data over an extended period. In order to compare the result with the actual position fixes for M.D.S. the following system of equations was used:

$$\begin{cases} \dfrac{du}{dt} = f(v - c_y) - \dfrac{K_w \rho_w}{m}(u - c_x)^2 + \dfrac{K_a \rho_a}{m} W_x^2 \\ \dfrac{dv}{dt} = -f(u - c_x) - \dfrac{K_w \rho_w}{m}(v - c_y)^2 + \dfrac{K_a \rho_a}{m} W_y^2 \\ \dfrac{dx}{dt} = u + c_x \\ \dfrac{dy}{dt} = v + c_y \end{cases} \quad \ldots\ (7.04)$$

where c_x and c_y are the geostrophic current components for the area under consideration, upon which the ice motion due to other causes is superimposed.

The system was solved simultaneously to obtain x and y at 10-minute time steps corresponding to the standard data spacings. The origin was taken at the point where wind measurements were begun (Figure 3.01), and the solution compared using different parameters with the original position fixes. A predictor corrector method (Hamming, 1962) was first used to solve equations (7.04), but it was subsequently found that essentially the same results were obtained with less computation using the fourth order Runge-Kutta procedure.

It became immediately obvious that in solving (7.04) it was not possible to attach the usual meaning to the water-drag coefficient. Realistic drift velocities could only be obtained by using a drag coefficient at least an order of magnitude less than that appropriate to the Reed and Campbell model. Variations of the different parameters were tried in an attempt to determine which values most nearly duplicated the shape and dimensions of the curve describing the different floe positions. Moderate agreement was established using an areal density m of 300 grams/cm^2, a water-drag coefficient of .002, an

air-drag coefficient of .0025 and a current velocity of 4 cm/sec (C_x = 3.5, C_y = -1.9). The respective curves are shown in Figure 7.05.

In choosing an areal density of 300 grams/cm^2 we are really implying that for some 250 cm beneath the ice, the water moves with the ice mass. This is of course a great simplification, but rather poor results are obtained if we take an areal density of only 50 grams/cm^2. The result of choosing different densities is shown in Figure 7.06. Both the shape of the curve and the orientation are affected by changing the mass. The increased deflection with greater mass is presumably a consequence of the larger Coriolis term.

Variation of the coefficient of air-drag is shown in Figure 7.07. Since there appears to be fair agreement on this parameter it was held at the average value of .0025 in the tests to determine a best fit. Changes in the water-drag are given in Figure 7.08.

Finally, variations in the current are shown in Figure 7.09. Since there was inadequate knowledge of the surface currents in the area a uniform current in the general direction of drift had been assumed. Since the floe travelled some 150 kilometers over four days it is hardly surprising that the two curves shown in Figure 7.05 do not match more closely. The current is weak in this area, but is known to be very variable with changing meteorological conditions. Moreover, it will not be always in the same direction at all points along the drift path. A still closer fit could have been obtained if we had taken a more rapid current over the 16th February, and subsequently a smaller value than actually used in Figure 7.05. In general it would seem advisable to set the current components C_x , C_y to be equal to simple functions of the x , y co-ordinates, the function

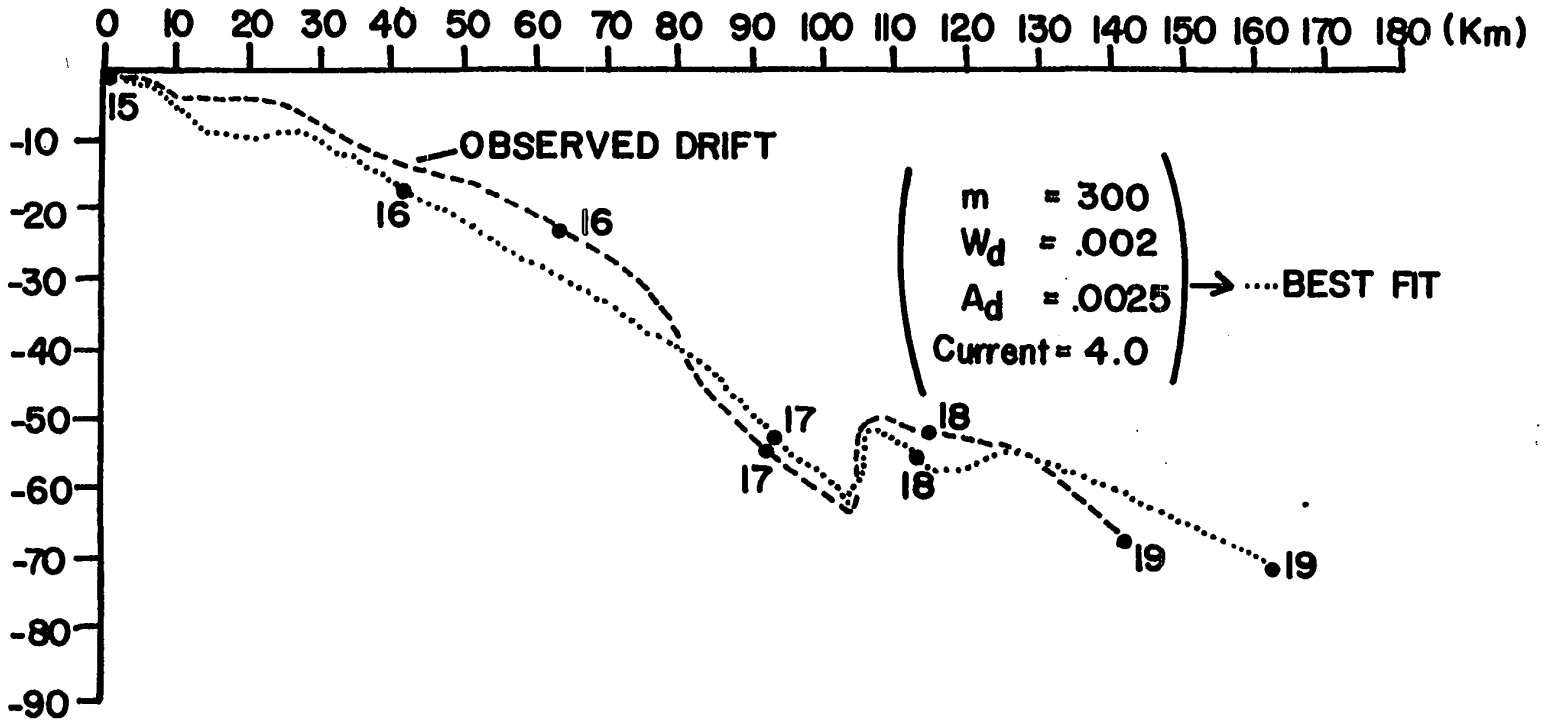

Figure 7.05- Observed Drift and Calculated Drift.

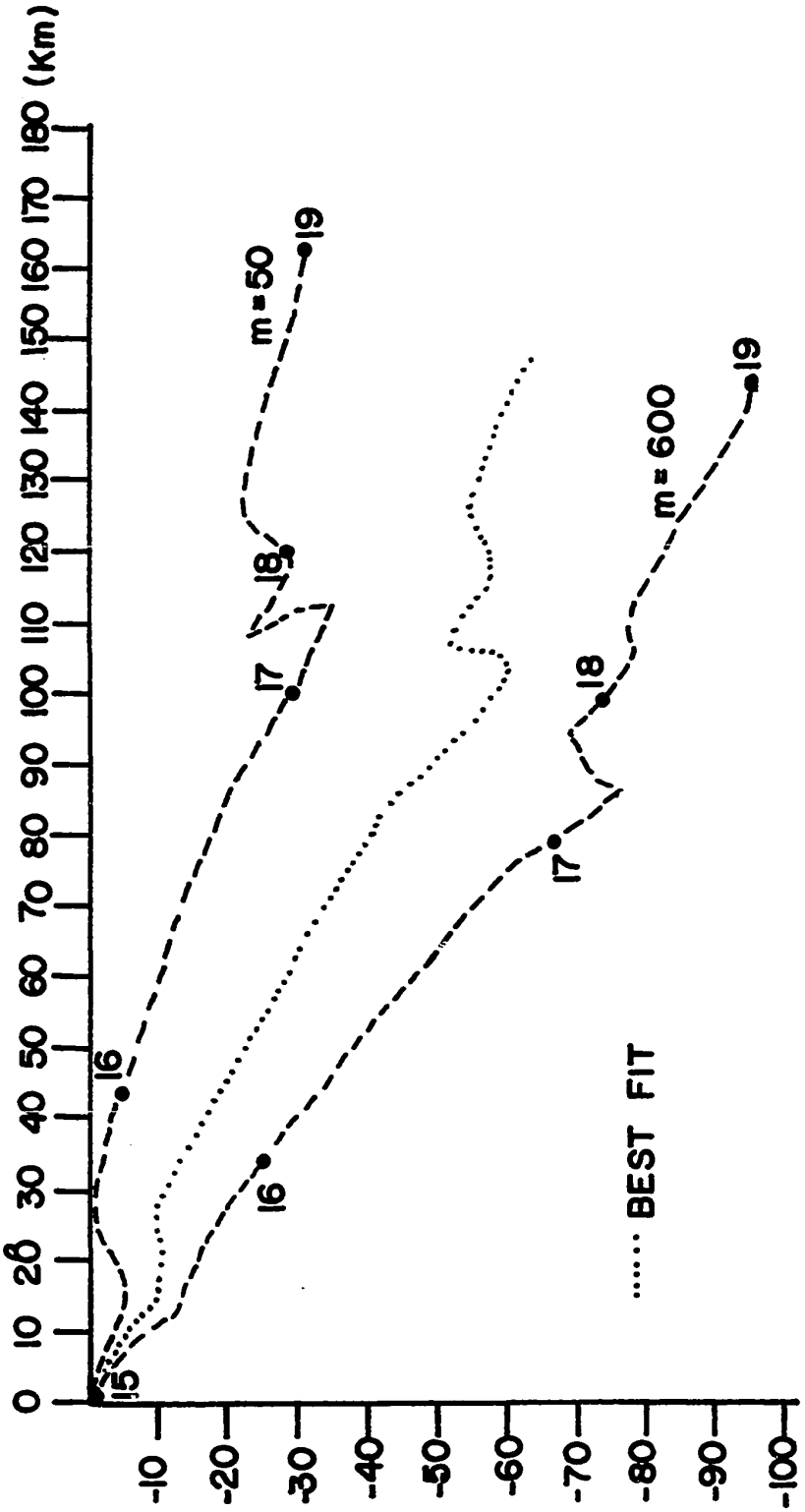

Figure 7.06 - Variation of Areal Density in Numerical Model.

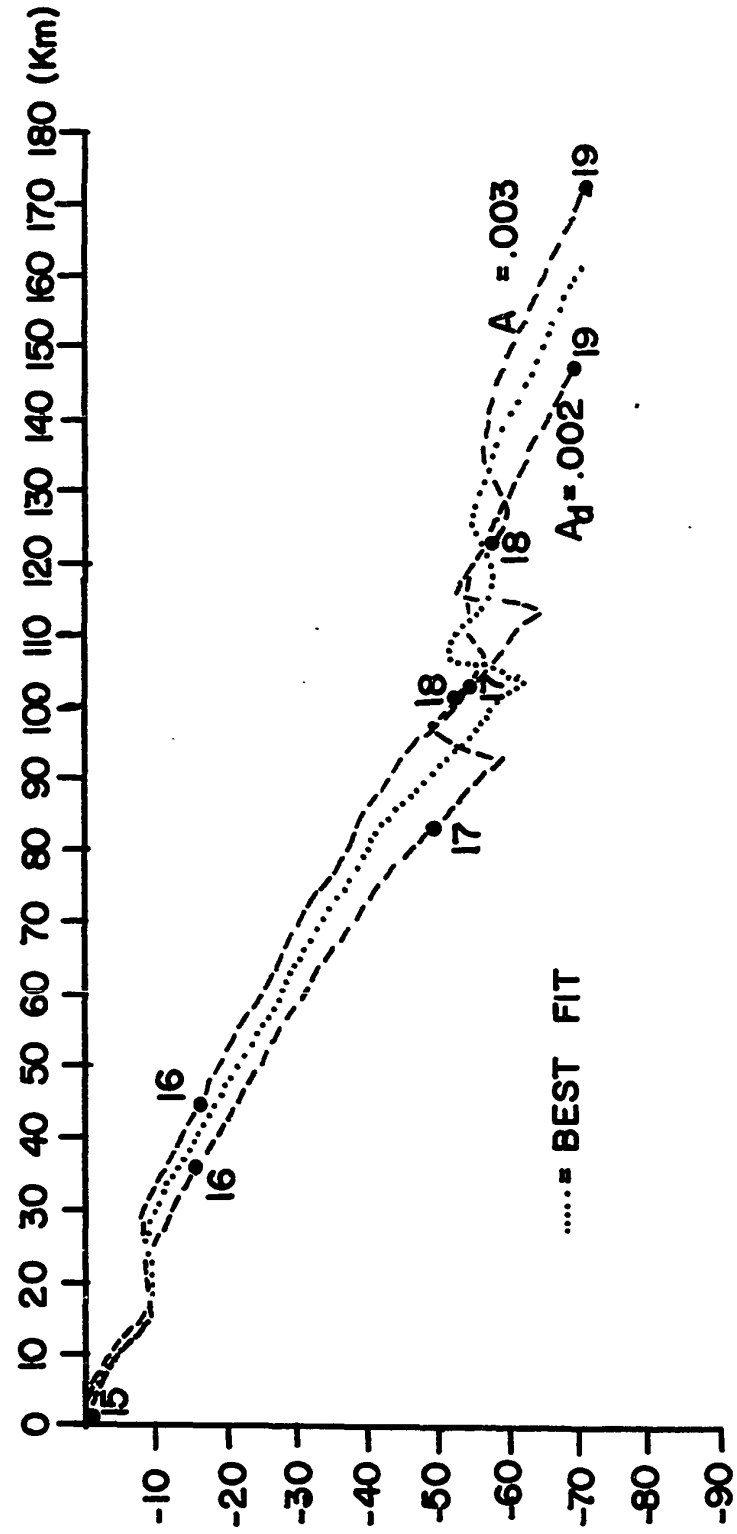

Figure 7.07 - Variation of Air Drag in Numerical Model.

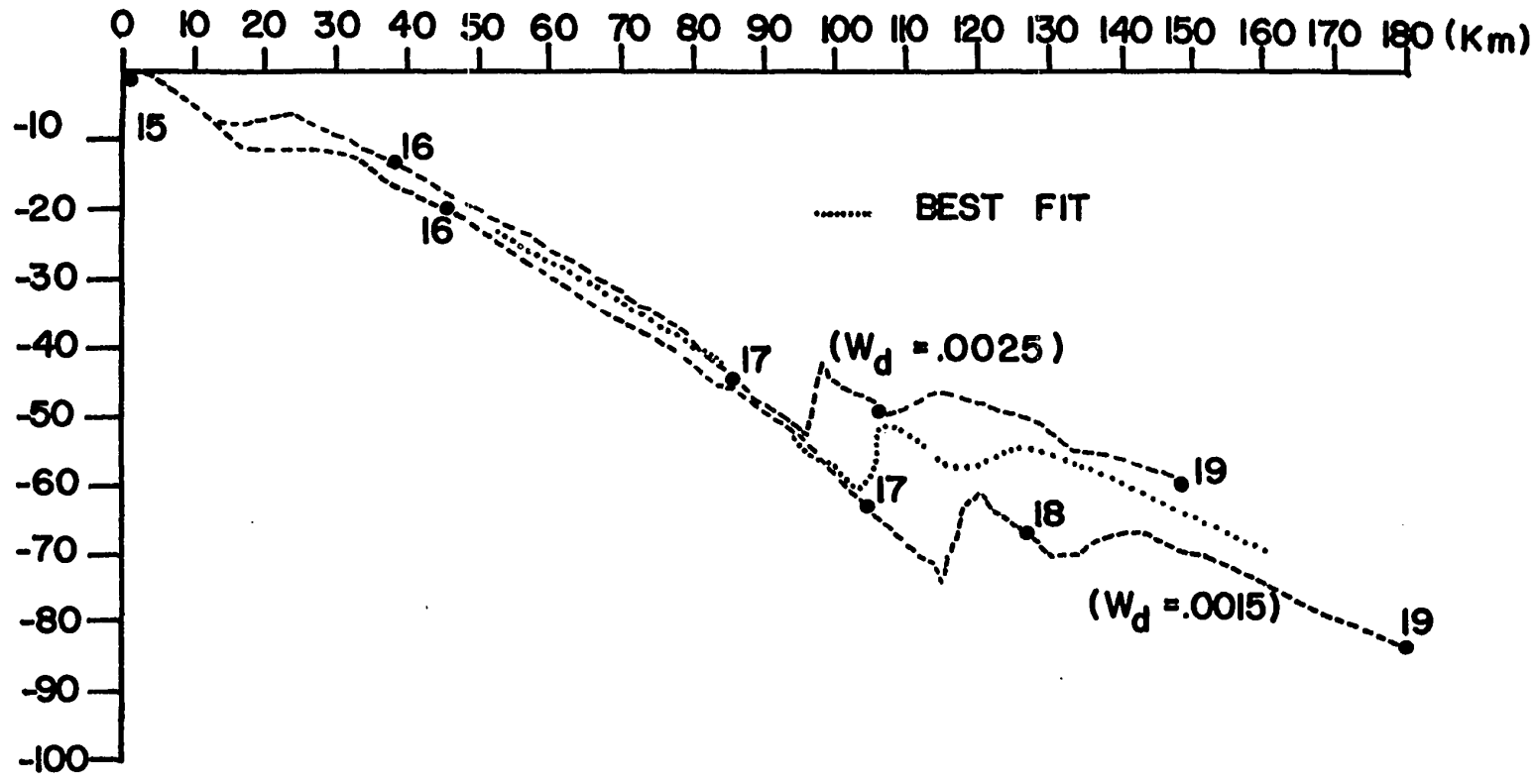

Figure 7.08 - Variation of Water Drag Coefficient in Numerical Model.

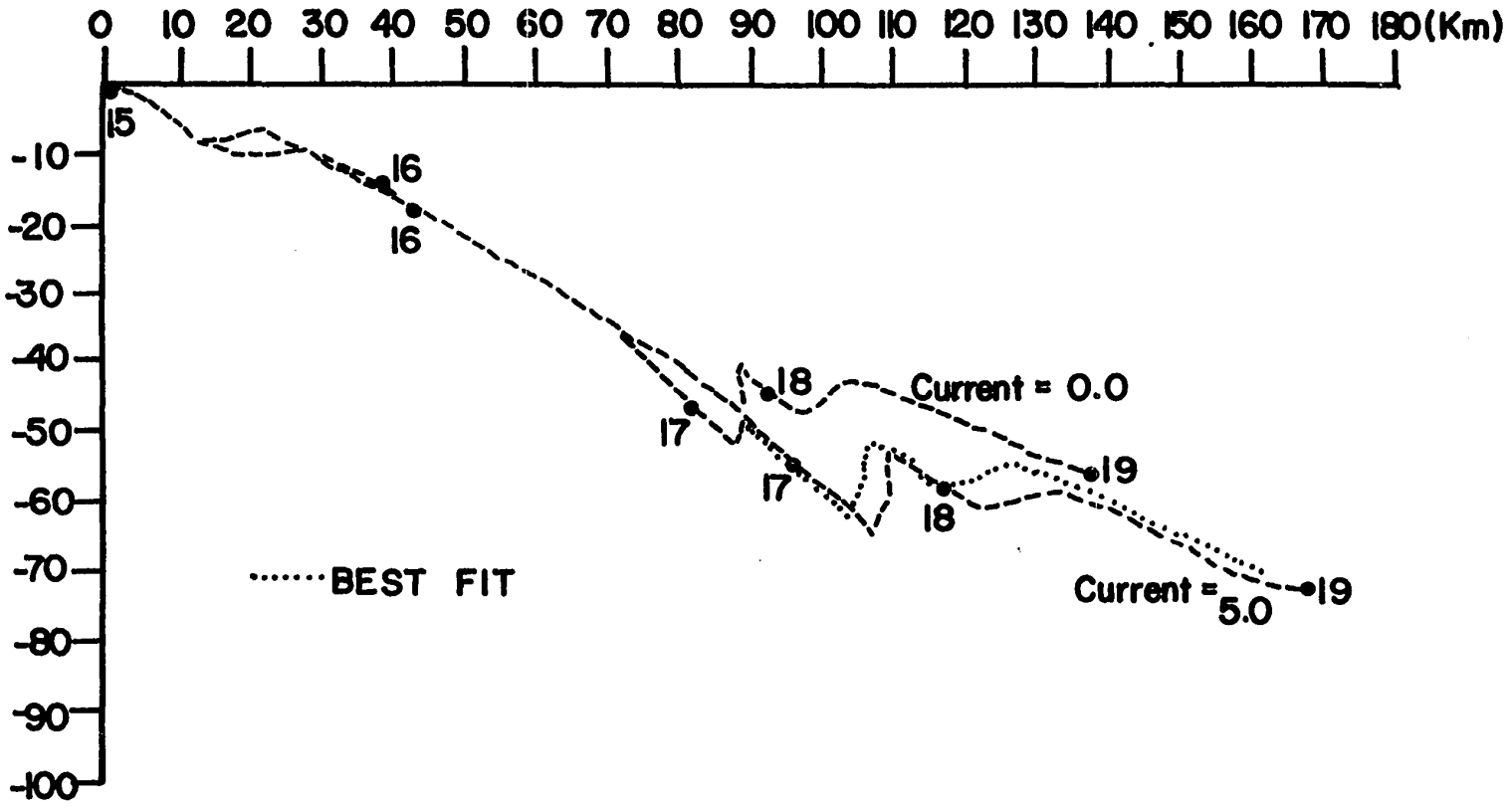

Figure 7.09 - Variations in Current Velocity.

parameters being determined from current data as they become available.

No attempt was made to allow for the possibility of internal ice stress. The model described by (7.04) can be modified to include Sverdrup-type internal resistance by adding terms of the form

$$-ru, \quad -rv$$

on the right-hand side of the first two equations, where r is the stress coefficient. The presence of ridging on the ice surrounding M.D.S. indicates the possibility of internal stresses, through the open water south of Anticosti Island and the general agreement of the observations with the simple model given above suggests that this is not an important factor in the case studied here. Sverdrup (1928) has shown how tidal motion can create ridging on an ice cover.

The model appears to provide a reasonable means of estimating ice drift. Application to M.D.S. data indicates that some 250 cm of water beneath the ice must be assumed to move with the surface cover, and that a water-drag coefficient appropriate to this assumption is .002.

Chapter 8 - Subsurface Accelerations

8.1 - Integration of Equations of Motion: uniform eddy viscosity

The limitation of models such as that considered in Chapter 7 is that they do not allow for the integrated effects of previous events on the water motion, and hence on the drag exerted by the water on the ice. The only theory that took this into account was Fjeldstad's, but since Fjeldstad neglected the mass of the ice he was not concerned with the water drag, but only with the velocity at the top of the water column.

The stress exerted by water on a moving sheet of ice will be the product of the (eddy) viscosity and the surface velocity shear of the water. The velocity shear in turn will be some function of the ice velocity at the time considered, together with the integrated effects of previous ice motion on the water mass. In order to analyse the surface shear we must therefore consider the equations of motion governing the water beneath the ice. In this analysis we neglect the curvature of the earth; we assume the surface stress to be distributed uniformly over an area great enough so that horizontal pressure gradients will not influence the result within the time periods of interest, and also that there is no vertical advection of water great enough to affect the result, except in the sense implied by the use of a coefficient of eddy viscosity, μ_e .

Under these conditions the Navier-Stokes equations reduce to

$$\frac{\partial u}{\partial t} - fv = \frac{\partial}{\partial z}\left[K_m(z)\frac{\partial u}{\partial z}\right]$$

$$\frac{\partial v}{\partial t} + fu = \frac{\partial}{\partial z}\left[K_m(z)\frac{\partial v}{\partial z}\right] \quad \ldots\ (8.01)$$

where $K_m = \mu_e/\rho_w$ is the vertical kinematic eddy viscosity. Assuming that the no-slip condition holds at the sea-bed and also at the ice-water interface, we obtain the boundary and initial conditions:

1. $U(z,0) = F(z)$, $V(z,0) = G(z)$ where $F(z)$ and $G(z)$ are functions defining the velocity distribution at time $t=0$.
2. $U(H,t) = V(H,t) = 0$
3. $U(0,t) = U_0(t)$, $V(0,t) = V_0(t)$ where $U_0(t)$ and $V_0(t)$ are the velocity components of the ice at time $t=0$.

The last boundary condition couples the partial differential equations (8.01) describing water motion, to the ordinary differential equations describing the ice motion:

$$\frac{dU_0}{dt} - fV_0 = -\frac{1}{\rho_i h_i} \cdot K_m(0)\left[\frac{\partial u}{\partial z}\Big|_{z=0}\right] + \frac{1}{\rho_i h_i}\tau_{a_x}$$

$$\frac{dV_0}{dt} + fU_0 = -\frac{1}{\rho_i h_i} \cdot K_m(0)\left[\frac{\partial v}{\partial z}\Big|_{z=0}\right] + \frac{1}{\rho_i h_i}\tau_{a_y} \quad \ldots\ldots (8.02)$$

where τ_{a_x} and τ_{a_y} are the x and y components of wind-stress. These equations will have to be integrated numerically under the specific initial conditions and wind-stress. This may be done in exactly the same way as was done in Chapter 7. It is the purpose of this chapter to derive expressions for the surface shear:

$$\frac{\partial u}{\partial z}\Big|_{z=0} \quad \text{and} \quad \frac{\partial v}{\partial z}\Big|_{z=0}$$

for substitution into equations (8.02).

If we use the transformation suggested by Fjeldstad (1930):

$$U = \varphi(z,t)\cos ft + \psi(z,t)\sin ft$$

$$V = -\varphi(z,t)\sin ft + \psi(z,t)\cos ft \qquad \ldots\ (8.03)$$

it can be shown (Appendix 4) that φ and ψ must satisfy

$$\frac{\partial \varphi}{\partial t} = \frac{\partial}{\partial z}\left[K_m(z)\frac{\partial \varphi}{\partial z}\right], \quad \frac{\partial \psi}{\partial z} = \frac{\partial}{\partial z}\left[K_m(z)\frac{\partial \psi}{\partial z}\right] \qquad \ldots\ (8.04)$$

Our conditions now become:

1. $\varphi(z,o) = F(z)$, $F(z)$ a known function of z
2. $\psi(z,o) = G(z)$, $G(z)$ a known function of z
3. $\varphi(H,t) = \psi(H,t) = o$
4. $\varphi(o,t)\cos ft + \psi(o,t)\sin ft = U_o$
5. $-\varphi(o,t)\sin ft + \psi(o,t)\cos ft = V_o$ $\qquad \ldots\ (8.05)$

Solving (8.05)-4 and -5 gives:

$$\varphi(o,t) = U_o\cos ft - V_o\sin ft$$

$$\psi(o,t) = U_o\sin ft + V_o\cos ft \qquad \ldots\ (8.06)$$

Hidaka (1932) has shown how these equations (under rather different boundary conditions) can be solved using Stokes' Method of Integration. However, this method relies on the expansion of φ and ψ in terms of eigenfunctions arising from an ordinary differential equation which includes the function $K_m(z)$. This author has not been able to solve this equation for a viscosity

distribution appropriate to the situation described here; it appears that the solutions are likely to be very complicated.

As a first step in examining this problem we shall consider the case of uniform eddy viscosity $K_m(z) = K_m$, where K_m is held to be constant. In this case the method of Laplace Transforms yields a solution more readily than Stokes' Integration method. We make the simplifying assumption that the depth is infinite and that the water is motionless at time $t = 0$. Since contributions to the solution decay exponentially with depth the effect of the former assumption will be negligible for ordinary ocean depths. If the initial conditions are non-zero the solution can still be obtained by use of the Green's Function (Appendix 5). The boundary conditions are now:

1. $\varphi(z,0) = \psi(z,0) = 0$
2. $\varphi(0,t) = U_0 \cos(ft) - V_0 \sin(ft)$
3. $\psi(0,t) = U_0 \sin ft + V_0 \cos ft$
4. $\varphi(z,t) = \psi(z,t) \to 0 \quad$ as $z \to \infty$ .... (8.07)

and equations (8.04) may be rewritten

$$\frac{\partial \varphi}{\partial t} = K_m \frac{\partial^2 \varphi}{\partial z^2}$$

$$\frac{\partial \psi}{\partial t} = K_m \frac{\partial^2 \psi}{\partial z^2} \qquad \text{.... (8.08)}$$

Applying the Laplace Transformation to equations (8.08) we obtain

$$\int_0^\infty e^{-pt}\frac{\partial \varphi}{\partial t}\,dt - K_m\int_0^\infty e^{-pt}\frac{\partial \psi}{\partial t}\,dt = 0$$

or $$\frac{d^2\varphi'}{dz^2} - \frac{p}{K_m}\varphi' - \frac{1}{K_m}\varphi(z,0) = 0$$

where the prime denotes the transformed function. For zero velocity initial conditions we have

$$\frac{d^2\varphi'}{dz^2} - \frac{p}{K_m}\varphi' = 0 \qquad \ldots. (8.09)$$

Since φ and hence ψ must be bounded as $z \to \infty$, of the two solutions to (8.09)

$$A e^{-z\sqrt{p/K_m}} \quad \text{and} \quad B e^{z\sqrt{p/K_m}}$$

we must use only $A e^{-z\sqrt{p/K_m}}$.

At the surface $z = 0$ we have condition (8.07)-2. Using the abbreviation

$$\varphi(0,t) = \chi_\varphi(t), \qquad \psi(0,t) = \chi_\psi(t)$$

this becomes on transformation

$$\varphi' = \chi'_\varphi(p) \qquad \text{at } z=0$$

The solution of equation (8.09) which has this value at $z = 0$ and is finite as $z \to \infty$ is $\varphi' = \chi'_\varphi(p)\, e^{-z\sqrt{p/K_m}}$

Now using the Superposition Theorem

$$L\{f_1(t)\}\,L\{f_2(t)\} = L\left\{\int_0^t f_1(\tau)\,f_2(t-\tau)\,d\tau\right\}$$

and the inverse transform of $e^{-z\sqrt{p/\kappa_m}}$, we obtain the solution

$$\varphi(z,t) = \frac{z}{2\sqrt{\pi\kappa_m}}\int_0^t \chi_\varphi(\tau)(t-\tau)^{-3/2} e^{\frac{-z^2}{4\kappa_m(t-\tau)}}\,d\tau$$

.... (8.10)

To obtain the shear at the surface we must take the limit as $z \to 0$ of the derivative with respect to z of our solution (8.10). We may then substitute φ_z and ψ_z into the shear equations:

$$u_z = \varphi_z \cos\omega t + \psi_z \sin\omega t$$

$$v_z = -\varphi_z \sin\omega t + \psi_z \cos\omega t$$

.... (8.11)

where the subscript z denotes partial differentiation with respect to z.

8.2 - Evaluation of the Shear

Taking the derivative of equation (8.10) yields, as $z \to 0$:

$$\lim_{z\to 0} \frac{\partial \varphi}{\partial z} = \lim_{z\to 0} \left\{ \frac{1}{2\sqrt{\pi K_m}} \int_0^t \frac{\chi_\varphi(\tau)\, e^{-z^2/4K_m(t-\tau)}}{(t-\tau)^{3/2}}\, d\tau \right.$$

$$\left. - \frac{z^2}{8K_m\sqrt{\pi K_m}} \int_0^t \frac{\chi_\varphi(\tau)\, e^{-z^2/4K_m(t-\tau)}}{(t-\tau)^{5/2}}\, d\tau \right\}$$

We cannot evaluate this limit as $z \to 0$ directly, since there is a singularity at $\tau = t$, and in general the function is not defined analytically.

Suppose, however, that $\chi_\varphi(\tau)$ behaves such that there exists some a close to t , $0 < a < t$, so that for $a \le \tau \le t$, $\chi_\varphi(\tau) =$ constant $= \bar{\chi}_\varphi$. Then we could break the solution (8.10) into two parts:

$$\varphi(z,t) = \frac{z}{2\sqrt{\pi K_m}} \int_0^a \chi_\varphi(\tau)\, (t-\tau)^{-3/2}\, e^{-z^2/4K_m(t-\tau)}\, d\tau$$

$$+ \frac{z}{2\sqrt{\pi K_m}}\, \bar{\chi}_\varphi \int_a^t e^{-z^2/4K_m(t-\tau)}\, (t-\tau)^{-3/2}\, d\tau$$

.... (8.12)

Considering first the second integral on the R.H.S. of (8.12), we use the transformation

$$u = z^2/4K_m(t-\tau), \qquad d\tau = (z^2/4K_m u^2)\, du$$

where u is the transformed variable, and obtain

$$\frac{\bar{\chi}_\varphi}{\sqrt{\pi}} \int_{z^2/4K_m(t-a)}^{\infty} e^{-u}\, u^{-1/2}\, du$$

This is the incomplete Gamma function,

$$\frac{\bar{\chi}_\varphi}{\sqrt{\pi}} \Gamma\left(\tfrac{1}{2},\ z^2/4K_m(t-a)\right)$$

which may be rewritten:

$$\frac{\bar{\chi}_\varphi}{\sqrt{\pi}} \left[\Gamma(1/2) - \gamma\left(1/2,\ z^2/4K_m(t-a)\right)\right]$$

Finally, using the relationship (Appendix 4)

$$\sqrt{\pi}\ \mathrm{erf}(x) = \gamma(1/2, x^2)$$

we have,

$$\frac{\bar{\chi}_\varphi}{\sqrt{\pi}} \left[\Gamma(1/2) - \sqrt{\pi}\ \mathrm{erf}\left(z/\sqrt{4K_m(t-a)}\right)\right]$$

so that equation (8.10) may be rewritten

$$\varphi(z,t) = \frac{z}{2\sqrt{\pi K_m}} \int_0^a \chi(\tau)\, \frac{e^{-z^2/4K_m(t-\tau)}}{(t-\tau)^{3/2}}\, d\tau$$

$$+\ \bar{\chi}_\varphi \left[1 - \mathrm{erf}\left(z/\sqrt{4K_m(t-a)}\right)\right]$$

.... (8.13)

At this point we may note that if we take $\lim_{z\to 0} \varphi(z,t)$ we obtain the previously defined surface value $\bar{\chi}_\varphi$.

We wish to determine the velocity shear at the surface, that is, we require $\lim_{z\to 0} \frac{\partial \varphi}{\partial z}$. Taking the derivative with respect to z of the first term on the R.H.S. of equation (8.13) gives:

$$\frac{1}{2\sqrt{\pi K_m}} \int_0^a \chi_\varphi(\tau)(t-\tau)^{-3/2} e^{-z^2/4K_m(t-\tau)} d\tau$$

$$+ \frac{z^2}{4K_m\sqrt{\pi K_m}} \int_0^a \chi_\varphi(\tau)(t-\tau)^{-5/2} e^{-z^2/4K_m(t-\tau)} d\tau$$

which in the limit as $z\to 0$ becomes

$$\frac{1}{2\sqrt{\pi K_m}} \int_0^a \chi_\varphi(\tau)(t-\tau)^{-3/2} d\tau \qquad \ldots. (8.14)$$

Next using

$$\frac{d}{dx}\left[\operatorname{erf}(x)\right] = \frac{2}{\sqrt{\pi}} e^{-x^2}$$

we take the derivative of the second term on the R.H.S. of (8.13) to obtain

$$-\left[\frac{2}{\sqrt{\pi}} e^{-z^2/4K_m(t-a)}\right] \frac{1}{\sqrt{4K_m(t-a)}} \bar{\chi}_\varphi$$

which in the limit as $z\to 0$ becomes

$$-\frac{2}{\sqrt{\pi}} \bar{\chi}_\varphi \frac{1}{\sqrt{4K_m(t-a)}} \qquad \ldots. (8.15)$$

Now combining (8.14) and (8.15) we obtain

$$\lim_{z\to 0} \frac{\partial \varphi}{\partial z} = \frac{1}{2\sqrt{\pi K_m}} \int_0^a \chi_\varphi(\tau)(t-\tau)^{-3/2} d\tau - \bar{\chi}_\varphi / \sqrt{\pi K_m (t-a)} \quad \ldots\ldots (8.16)$$

which is the required expression for surface shear.

If the ice had moved at a constant velocity from time $t=0$, we would obtain

$$\lim_{z\to 0} \frac{\partial \varphi}{\partial z} = - \frac{\bar{\chi}_\varphi}{\sqrt{\pi K_m t}}$$

which is exact for all $t > 0$. A singularity occurs here at $t = 0$, the physical significance of this being that the shear is infinite at that time due to the impulsive motion defined for the ice.

In evaluating (8.16) numerically a would be taken as one time step prior to t. Since the time steps are chosen to be small enough in comparison with the acceleration of the ice that there would be negligible change in $\chi_\varphi(\tau)$ over one time step, the errors incurred by the restriction that (8.16) implies will be within those normally accepted when using numerical integration procedures.

Deriving equation (8.16) for ψ

$$\lim_{z\to 0} \frac{\partial \psi}{\partial z} = \frac{1}{2\sqrt{\pi K_m}} \int_0^a \chi_\psi(\tau)(t-\tau)^{-3/2} d\tau - \frac{\bar{\chi}_\psi}{\sqrt{\pi K_m (t-a)}} \quad \ldots\ldots (8.17)$$

If we let $\bar{\chi}_\varphi = \chi_\varphi(t)$ and $\bar{\chi}_\psi = \chi_\psi(t)$ and substitute (8.16) and (8.17) into (8.11) we obtain

$$U_2 = \frac{1}{2\sqrt{\pi K_m}} \int_0^a \Big[\big(U_0(\tau)\cos f\tau - V_0(\tau)\sin f\tau\big)\cos ft + \big(U_0(\tau)\sin f\tau + V_0(\tau)\cos f\tau\big)\sin ft \Big] (t-\tau)^{-3/2}\, d\tau - \frac{1}{\sqrt{\pi K_m (t-a)}} \Big[\big(U_0(t)\cos ft - V_0(t)\sin ft\big)\cos ft + \big(U_0(t)\sin ft + V_0(t)\cos ft\big)\sin ft \Big]$$

$$V_2 = \frac{1}{2\sqrt{\pi K_m}} \int_0^a \Big[\big(U_0(\tau)\cos f\tau - V_0(\tau)\sin f\tau\big)(-\sin f\tau) + \big(U_0(\tau)\sin f\tau + V_0(\tau)\cos f\tau\big)\cos ft \Big] (t-\tau)^{-3/2}\, d\tau - \frac{1}{\sqrt{\pi K_m (t-a)}} \Big[-\big(U_0(t)\cos ft - V_0(t)\sin ft\big)\sin ft + \big(U_0(t)\sin ft + V_0(t)\cos ft\big)\cos ft \Big]$$

which simplifies to

$$U_2 = \frac{1}{2\sqrt{\pi K_m}} \int_0^a \Big[\big(U_0(\tau)\cos f(t-\tau) + V_0(\tau)\sin f(t-\tau)\big) \Big] (t-\tau)^{-3/2}\, d\tau - \frac{U_0(t)}{\sqrt{\pi K_m (t-a)}}$$

$$V_2 = \frac{-1}{2\sqrt{\pi K_m}} \int_0^a \Big[\big(U_0(\tau)\sin f(t-\tau) - V_0(\tau)\cos f(t-\tau)\big) \Big] (t-\tau)^{-3/2}\, d\tau - \frac{V_0(t)}{\sqrt{\pi K_m (t-a)}}$$

.... (8.18)

which may be integrated numerically. The surface drag terms are given by the product of the shear (8.18) and the eddy viscosity, the ordinary differential equation for the ice then being integrated in exactly the same way as in the previous chapter.

The integration of equations (8.02) using (8.18) requires a complete integration of (8.18) at each time-step in the integration of (8.02). In practice it would hardly be necessary to integrate back to $t = 0$ each time, since contributions are weighted by the

factor $(t-\tau)^{-3/2}$ so that two or three hours would probably suffice. Having evaluated the ice motion over a certain period it is then possible to use our solution (8.10), together with its analogous form in ψ, to determine the water velocity at different times and depths:

$$U(z,t) = \frac{z}{2\sqrt{\pi K_m}} \int_0^t \left[U_0(\tau)\cos f(t-\tau) + V_0(\tau)\sin f(t-\tau) \right] e^{-z^2/4K_m(t-\tau)} (t-\tau)^{-3/2} d\tau$$

$$v(z,t) = \frac{-z}{2\sqrt{\pi K_m}} \int_0^t \left[U_0(\tau)\sin f(t-\tau) - V_0(\tau)\cos f(t-\tau) \right] e^{-z^2/4K_m(t-\tau)} (t-\tau)^{-3/2} d\tau$$

.... (8.19)

which may be integrated numerically for all depths greater than 0 and all times up to t.

Equations (8.19) show that provided τ is sufficiently far from t, the exponential term will not dominate the integrand for a specific z. The greater the depth, the greater must be the value $(t-\tau)$ for the exponential term to disappear. This suggests a useful procedure for estimating the value of Km, since this parameter determines the rate at which surface velocity fluctuations diffuse downwards through the water.

Consider an ice water system, initially motionless, which at time t =0 receives a surface impulse of the Dirac delta type such that:

$$U_o(t) = V_o(t) = 0 \quad \text{at} \quad t \neq 0$$

$$\int_{-\infty}^{\infty} U_o(t)dt = \int_{-\infty}^{\infty} V_o(t)dt = 1$$

In this case we may solve the velocity equations (8.19) to obtain

$$U(z,t) = \frac{z}{2\sqrt{\pi K_m}} \cdot [1] \cdot \cos ft \; e^{-z^2/4K_m t} \; t^{-3/2}$$

$$V(z,t) = \frac{-z}{2\sqrt{\pi K_m}} \cdot [1] \cdot \sin ft \; e^{-z^2/4K_m t} \; t^{-3/2}$$

.... (8.20)

The absolute velocity will then be

$$\frac{z}{2\sqrt{\pi K_m}} \; e^{-z^2/4K_m t} \; t^{-3/2}$$

Figure 8.01 shows absolute velocities attained at a depth of 5 meters with eddy viscosities of 75 and 100 (c.g.s.) respectively. It is seen that the viscosity not only changes the elapsed time for maximum velocity, but also the general shape of the curve. In practice $U_o(\tau)$ and $V_o(\tau)$ will be continuously changing, and the velocity at any depth will then be simply a superposition of solutions of the type (8.20). By numerically integrating (8.19) with different values of K_m, correlation with the observed velocity may be used to obtain an average value of the eddy viscosity.

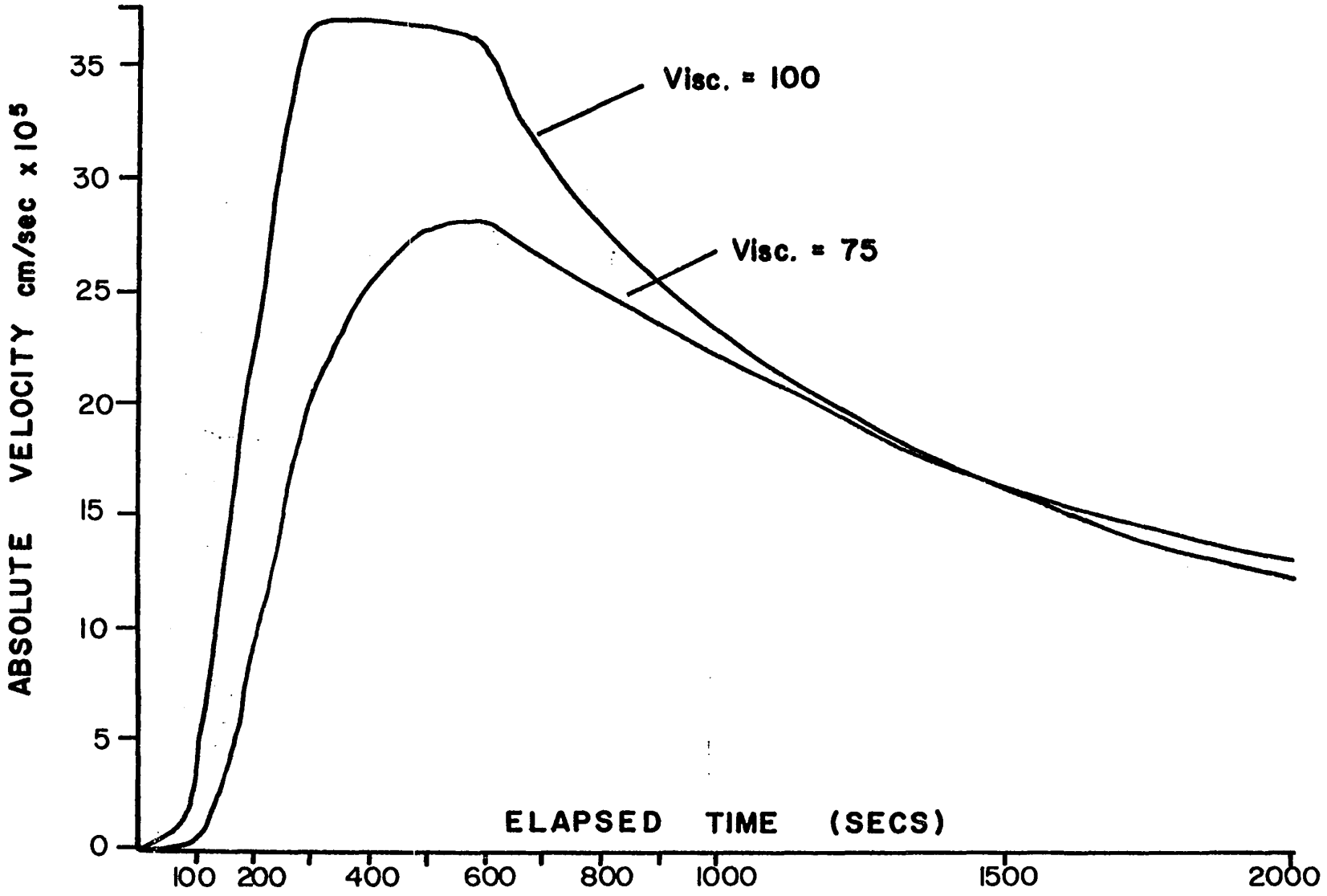

Figure 8.01 - Response of Water at 5 Meters to Unit Impulse at Surface.

8.3 - Inclusion of the boundary layer

A satisfactory evaluation of the drag exerted by the water on the ice must include an integration of the equations of motion with a depth-dependent eddy viscosity. In particular, if we accept that a Prandtl type of boundary layer exists close to the ice, this implies a linear increase in eddy viscosity from the ice to the base of the boundary layer. Beneath the boundary layer the eddy viscosity is generally assumed to be constant, though there appears to be little evidence to support either this or any alternative distribution. However, since changes in the eddy viscosity of the deeper layers influence the solution to an extent exponentially decreasing with depth, a uniform value beneath the boundary layer is a reasonable assumption.

Reed and Campbell (1960) matched equations under these assumptions, but allowed a 45^{o} direction shear at the interface. Hunkins (1967) obtained a good agreement between current profiles measured beneath the Arctic ice and that predicted by the boundary and spiral layer model proposed by Ekman (1928). Numerous other hypotheses have been put forward for the variation of eddy viscosity with depth: the problem is similar to that enccuntered in the case of air motion in Chapter 5. Kozlov (1962) has discussed the effect of variations in the viscosity coefficient in terms of power functions; Jeffreys (1923) considered the possibility that the coefficient was proportional to the square of the velocity shear. In Hidaka's analysis of time-dependent drift currents (1932), a solution was found for the expression

$$K_m = A(1 - z/B)^{1-c}$$

where A, B and C are chosen for the appropriate conditions. However, this expression cannot describe the situation in which the turbulence is suppressed close to the surface. Fjeldstad (1930) suggested the use of eigen function expansions to express the variation of eddy viscosity with depth, but unfortunately gave no examples. Hidaka's model can be solved for the case of a linearly increasing viscosity, appropriate to the boundary layer, by transforming the ordinary differential equation occurring in his derivation, into Bessel's equation. However, the boundary layer is generally considered to be very thin, perhaps less than one meter, and such a solution is likely to give misleading results.

An alternative approach is to consider the boundary layer to be of uniform, though smaller eddy viscosity, overlying a deeper layer also of uniform eddy viscosity. Such an approach implies a discontinuity in the mixing length at the interface, but does not imply a velocity or direction discontinuity. Using the procedure outlined in the previous section two or more equations can be matched under the assumption of a pointwise continuous stress and velocity distribution in the neighbourhood of the respective interfaces. The problem has an analogy in the conduction of heat through composite slabs; under different boundary conditions it has been discussed in the most general case by Sakai (1922), and also by Carslaw and Jaegar (1952). Part of this analysis, in particular that of the steady state part of the solution, follows their discussion.

We consider a two-layer system in which an upper layer of eddy viscosity K_{m_1}, occupying the region $-\ell < z < 0$ overlies an infinitely deep layer of viscosity K_{m_2} in the region $0 < z$.

The subscript 1 will denote quantities in the upper layer, the subscript 2 those in the lower layer. At the interface we match the stress

$$K_{m_1} \frac{\partial U_1}{\partial z} = K_{m_2} \frac{\partial U_2}{\partial z}$$

$$K_{m_1} \frac{\partial V_1}{\partial z} = K_{m_2} \frac{\partial V_2}{\partial z}$$

at $z=0$, $t>0$ .... (8.21)

and impose a finite velocity shear

$$U_1 = U_2$$

$$V_1 = V_2$$

at $z=0$, $t>0$ .... (8.22)

Under the transformation (8.03) we obtain from (8.21)

$$K_{m_1} \frac{\partial \varphi_1}{\partial z} \cos ft + K_{m_1} \frac{\partial \psi_1}{\partial z} \sin ft = K_{m_2} \frac{\partial \varphi_2}{\partial z} \cos ft + K_{m_2} \frac{\partial \psi_2}{\partial z} \sin ft$$

$$-K_{m_1} \frac{\partial \varphi_1}{\partial z} \sin ft + K_{m_1} \frac{\partial \psi_1}{\partial z} \cos ft = -K_{m_2} \frac{\partial \varphi_2}{\partial z} \sin ft + K_{m_2} \frac{\partial \psi_2}{\partial z} \cos ft$$

.... (8.23)

which reduces to

$$K_{m_1} \frac{\partial \varphi_1}{\partial z} = K_{m_2} \frac{\partial \varphi_2}{\partial z}$$

$$K_{m_1} \frac{\partial \psi_1}{\partial z} = K_{m_2} \frac{\partial \psi_2}{\partial z}$$

at $z=0$ .... (8.24)

Under the same transformation, (8.22) yields

$$\varphi_1 \cos ft + \psi_1 \sin ft = \varphi_2 \cos ft + \psi_2 \sin ft$$

$$-\varphi_1 \sin ft + \psi \cos ft = -\varphi_2 \sin ft + \psi_2 \cos ft$$

giving

$$\varphi_1 = \varphi_2$$

$$\psi_1 = \psi_2 \qquad \text{at } z=0 \qquad \ldots. (8.25)$$

Within each layer the equations of motion take the same form as in the previous section; i.e. after taking Laplace transforms,

$$\frac{\partial^2 \varphi_1'}{\partial z^2} - \left[\frac{p}{K_{m_1}}\right]^{1/2} \varphi_1' = 0 \qquad -\ell < z < 0 \qquad \ldots. (8.26)$$

$$\frac{\partial^2 \varphi_2'}{\partial z^2} - \left[\frac{p}{K_{m_2}}\right]^{1/2} \varphi_2' = 0 \qquad z > 0 \qquad \ldots. (8.27)$$

with the new conditions

$$K_{m_1} \frac{\partial \varphi_1'}{\partial z} = K_{m_2} \frac{\partial \varphi_2'}{\partial z} \qquad \text{at } z=0 \qquad \ldots. (8.28)$$

$$\varphi_1' = \varphi_2' \qquad \text{at } z=0 \qquad \ldots. (8.29)$$

$$\varphi_1' = \chi_\varphi'(p) \qquad \text{at } z=-\ell \qquad \ldots. (8.30)$$

$$\varphi_2' \to 0 \qquad \text{as } z \to \infty \qquad \ldots. (8.31)$$

Similar equations and conditions would be defined for the variable φ .

A solution of (8.26) which satisfies (8.30) is

$$\varphi_1' = \chi_\varphi'(p)\cosh\xi_1[l+z] + A\sinh\xi_1[l+z] \qquad \ldots. (8.32)$$

where we use the abbreviation

$$\xi_1 = \sqrt{\frac{p}{K_{m_1}}}, \quad \xi_2 = \sqrt{\frac{p}{K_{m_2}}}, \quad \eta = \sqrt{\frac{K_{m_2}}{K_{m_1}}}$$

A solution of (8.27) satisfying (8.31) is

$$\varphi_2' = B e^{-\xi_2 z} \qquad \ldots. (8.33)$$

Now substituting (8.32) and (8.33) into (8.28) and (8.29) to eliminate A and B we obtain

$$\varphi_1' = \chi_\varphi'(p)\frac{[\cosh\xi_1 z - \eta\sinh\xi_1 z]}{[\cosh\xi_1 l + \eta\sinh\xi_1 l]} \qquad \ldots. (8.34)$$

and

$$\varphi_2' = \chi_\varphi'(p)[\cosh\xi_1 l + \eta\sinh\xi_1 l]^{-1} e^{-\xi_2 z} \qquad \ldots. (8.35)$$

We will only consider (8.34) since we are chiefly interested in the surface shear; φ_2' may be developed in a similar fashion. Since (8.34) was not found in tables of inverse Laplace transforms, we use the method of expansion in negative powers of e , (Carslaw and Jaegar, 1963):

$$\varphi_1' = \chi_\varphi'(p)\frac{[e^{\xi_1 z} + e^{-\xi_1 z} - \eta e^{\xi_1 z} + \eta e^{-\xi_1 z}]}{[e^{\xi_1 l} + e^{-\xi_1 l} + \eta e^{\xi_1 l} - \eta e^{-\xi_1 l}]}$$

$$= \chi'_{\varphi(p)} \frac{e^{-\xi_1(z+l)} + \nu e^{\xi_1(z-l)}}{1 + \nu e^{-2\xi_1 l}}$$

where $\nu = \frac{1-n}{1+n}$

Now using the Binomial theorem we obtain

$$\varphi_1' = \chi'_{\varphi(p)} \left[e^{-\xi_1(z+l)} + \nu e^{\xi_1(z-l)} \right] \sum_{n=0}^{\infty} (-1)^n \nu^n e^{-2\xi_1 l n} \quad \ldots\ldots (8.36)$$

We are now in a position to take inverse Laplace transforms, so that using again the Superposition theorem we obtain:

$$\varphi_1 = \int_0^t \chi_{\varphi(\tau)} \sum_{n=0}^{\infty} (-1)^n \nu^n \left[\frac{(2n+1)l+z}{2\sqrt{\pi K_{m_1}(t-\tau)^3}} e^{-\frac{\{(2n+1)l+z\}^2}{4K_{m_1}(t-\tau)}} + \nu \frac{(2n+1)l-z}{2\sqrt{\pi K_{m_1}(t-\tau)}} e^{-\frac{\{(2n+1)l-z\}^2}{4K_{m_1}(t-\tau)}} \right] d\tau$$

The surface shear is then given by

$$\left.\frac{\partial \varphi_1}{\partial z}\right|_{z=-l} = \int_0^t \chi_{\varphi(\tau)} \sum_{n=0}^{\infty} \frac{(-1)^n \nu^n}{2\sqrt{\pi K_{m_1}(t-\tau)^3}} \left\{ \left(1 - \frac{2n^2}{K_{m_1}(t-\tau)}\right) e^{\frac{-n^2}{K_{m_1}(t-\tau)}} - \nu\left(1 - \frac{2(n+l)^2}{K_{m_1}(t-\tau)}\right) e^{\frac{-(n+l)^2}{K_{m_1}(t-\tau)}} \right\} d\tau \quad \ldots\ldots (8.37)$$

Again we find that numerical integration will not be possible without imposing a restriction on $\chi_{\varphi(\tau)}$ for an arbitrarily small period prior to $\tau = t$. Considering now, only this short interval

$a \leq \tau \leq t$ in which $\chi_\varphi(\tau) = \bar{\chi}_\varphi$, a constant, we obtain the new boundary condition replacing (8.30):

$$\varphi_1' = \frac{\bar{\chi}_\varphi}{p} \qquad \text{at } z = -\ell$$

The two solutions corresponding to (8.32) and (8.33) are then

$$\varphi_1' = \frac{\bar{\chi}_\varphi}{p} \cosh \xi_1 [\ell + z] + A \sinh \xi_1 [\ell + z]$$

$$\varphi_2' = B e^{-\xi_2 z}$$

Eliminating A and B , we have

$$\varphi_1' = \frac{\bar{\chi}_\varphi [\cosh \xi_1 z - \eta \sinh \xi_1 z]}{p [\cosh \xi_1 \ell + \eta \sinh \xi_1 \ell]}$$

Expanding as before in negative powers of e , gives

$$\varphi_1' = \frac{\bar{\chi}_\varphi}{p} \sum_{n=0}^{\infty} \nu^n \left\{ e^{-\xi_1 [(2n+1)\ell + z]} - \nu e^{-\xi_1 [(2n+1)\ell - z]} \right\}$$

and taking inverse Laplace transforms gives:

$$\varphi_1 = \bar{\chi}_\varphi \sum_{n=0}^{\infty} \nu^n \left\{ \operatorname{erfc} \frac{(2n+1)\ell + z}{2\sqrt{K_{m_1}(t-a)}} - \right.$$

$$\left. \nu \operatorname{erfc} \frac{(2n+1)\ell - z}{2\sqrt{K_{m_1}(t-a)}} \right\}$$

The derivative at the surface corresponding to (8.15) is then

$$\frac{-\bar{\tau}_{w,\psi}}{\sqrt{\pi K_m (t-a)}} \left\{ 1 + 2 \sum_{n=1}^{\infty} \nu^{n^2} e^{-n^2 \xi^2 / K_m (t-a)} \right\} \quad \ldots\ldots (8.38)$$

The expression (8.38) together with the non-steady part (8.37) which is integrated over the interval $0 \leq \tau \leq a$, are equivalent to the expression (8.16) for the case of uniform eddy viscosity, and give the surface shear in terms of φ and ψ for the boundary layer model. Substitution into (8.11) and multiplication by the surface eddy viscosity will then give the required drag on the ice. Using this drag term the ordinary differential equation for ice drift may then be integrated numerically as in Chapter 7.

Equation (8.37) shows that the time integration must be summed until convergence occurs. This greatly increases the required computation time. Convergence of the series will be more rapid for smaller time intervals; provided we are mainly concerned with the more rapid accelerations associated with ice-drift, integration of these equations should be practicable on a modern digital computer.

BIBLIOGRAPHY

Abramowitz, M. and I.A. Stegun, 1965: Handbook of Mathematical Functions, New York.

Blackadar, A.K., 1962: The Vertical Distribution of Wind and Turbulent Exchange in a Neutral Atmosphere. Journal of Geophysical Research, Vol. 67, No. 8, pp. 3095-3102.

Blackford, B.L. and Y.W. Tsang, 1964: Average Wind-Stress Data for the Gulf of St. Lawrence. Fisheries Research Board of Canada. MS Report Series (Oceanographic and Limnological), No. 183.

Blackman, R.B. and J.W. Tukey, 1959: The Measurement of Power Spectra from the point of view of Communications Engineering. New York, 1956.

Browne, I.M. and A.P. Crary, 1958: The Movement of Ice in the Arctic Ocean. Arctic Sea Ice. National Academy of Sciences - National Research Council Publication 598. Washington.

Campbell, W.J., 1964: On the Steady-State Flow of Sea Ice. Ph.D. Thesis, University of Washington.

Carslaw, H.S. and J.C. Jaegar, 1952: Conduction of Heat in Solids, 2nd ed., Oxford.

_____ 1963: Operational Methods in Applied Mathematics. Dover, New York.

Defant, A., 1961: Physical Oceanography Vol. 2, Pergamon Press, London.

Defant, F., 1940: Trägheitschwingungen im Ozean und in der Atmosphäre. Veröff. Meteorol. Inst., Univ. Berlin, Vol. 4, No. 2.

De Lury, D.B., 1950: Values and Integrals of Orthogonal Polynomials up to n=26. University of Toronto Press, Toronto.

Ekman, V.W., 1905: On the Influence of the Earth's Rotation on Ocean Currents. Arkiv för Matematik, Astronomi och Fysik, Band 2, No. 11, pp. 1-52.

_____ 1928: Eddy-viscosity and skin-friction in the dynamics of winds and ocean currents. Memoirs of the Royal Meteorological Society Vol. 2, pp. 161-172. (Quoted in Hunkins, 1966).

Ellison, T.H., 1956: Atmospheric Turbulence, in "Surveys in Mechanics", ed. G.K. Batchelor & R.M. Davies, New York, pp. 400-430. (Quoted in Blackadar, 1962).

Farquharson, W.I., 1962: Tides, Tidal Streams and Currents in the Gulf of St. Lawrence. Dept. of Mines and Technical Surveys, Ottawa.

_____ 1966: St. Lawrence Estuary Current Surveys. Bedford Institute of Oceanography Report No. 66-6. (Unpublished MS).

Fel'zenbaum, A.I., 1958: The Theory of Steady State Drift of Ice and the Calculation of the Long Period Mean Drift in the Central Part of the Arctic Basin. Problems of the North, No. 2. (English Translation by National Research Council, Ottawa).

Fjeldstad, J.E., 1930: Ein Problem aus der Windstromtheorie. Zeitschrift für angewandte Mathematik und Mechanik, Vol. 10, pp. 121-137.

_____ 1964: Internal Waves of Tidal Origin. Part 1: Theory and Analysis of Observations. Geophys. Publik. Oslo.

Frost, R., 1948: Quarterly Journal of the Royal Meteorological Society, Vol. 74. (Quoted in Haltiner and Martin, 1957).

Fukutomi, T., 1951: A Theory of the Steady Drift of Sea Ice due to Wind on the Frozen Sea. Arctic Sea Ice. NAS-NRC publication 598, Washington.

Gordienko, P., 1958: Arctic Ice Drift. Arctic Sea Ice. NAS-NRC publication 598, Washington.

Haltiner, G.J. and F.L. Martin, 1957: Dynamical and Physical Meteorology. McGraw-Hill, New York/Toronto/London.

Hamming, R.W., 1962: Numerical Methods for Scientists and Engineers. McGraw Hill, New York/Toronto/London.

Haurwitz, B., 1936: Gerlands Beitr. Geophysik. Vol. 45 (1935) and Vol. 46 (1936). (Quoted in Haltiner and Martin, 1957).

Heisenberg, W., 1948: Zur statischen Theorie der Turbulenz. Z. Physik Vol. 124, pp. 628-657.

Hidaka, K., 1932: Anwendung der Stokes'schen Methode auf die Theorie der Winderzeugten Meerstromungen. Memoirs of the Imperial Marine Observatory, Kobe, Vol. 5, No. 2.

Hildebrand, F.B., 1956: Introduction to Numerical Analysis. McGraw Hill, New York/Toronto/London.

Hunkins, K., 1966: Ekman Drift Currents in the Arctic Ocean. Deep Sea Research, Vol. 13, pp. 607-620.

_____ 1967: Inertial Oscillations of Fletcher's Ice Island (T-3). Journal of Geophysical Research, Vol. 72, No. 4, pp. 1165-1174.

I.B.M., 1968: S.S.P. Version 3. International Business Machines Corporation. Publication H20-0205-3.

Ingram, R.G., 1967: Ice Drift in the Gulf of St. Lawrence. M.Sc. Thesis, Marine Sciences Center, McGill University.

Ingram, R.G., O.M. Johannessen and E.R. Pounder, 1968: A Pilot Study in the Gulf of St. Lawrence. Marine Sciences Center, McGill University, MS Report No. 5.

Jenkins, G.M. and D.G. Watts, 1968: Spectral Analysis and its Applications. Holden-Day, San Francisco/Cambridge/London/ Amsterdam.

Johannessen, O.M., E.R. Pounder, H. Serson, J. Keys, D. Lindsay, W. Seifert and E. Banke, 1968: Preliminary Report on the "Ice Drift Study" in the Gulf of St. Lawrence, Winter 1968. Marine Sciences Center, McGill University, MS Report No. S-13.

Johannessen, O.M., S. Smith, E.R. Pounder, J. Keys, H. Serson, E. Banke and D. Finlayson., 1969: Preliminary Report from the McGill Ice Drift Study in the Gulf of St. Lawrence, 1969. Marine Sciences Center, McGill University, MS Report No. S-15.

Kohler, H., 1933: Kgl. Svenska Vetenskapsakad. Handl., Vol. 13. (Quoted in Haltiner and Martin, 1957).

Kozlov, V.F., 1963: On the Influence of a Change in the Vertical Mixing on Drift Currents. Isvestya Geophys. Series No. 7, pp. 671-674. (English edition).

Lettau, H., 1950: A re-examination of the "Leipzig wind profile" considering some relations between wind and turbulence in the friction layer. Tellus 2, pp. 125-129. (Quoted in Blackader, 1962).

Nansen, F., 1902: The Oceanography of the North Polar Basin. The Norwegian North Polar Expedition, 1893-1896, Scientific Results, 3.

Nomitsu, T., 1933: A Theory of the Rising Stage of Drift Current in the Ocean. Memoirs of the College of Science, Imperial University of Kyôto, Series A, Vol. 16, No. 2, pp. 161-175.

Panofsky, H.A. and R.A. McCormick, 1960: The Spectrum of Vertical Velocity near the Surface. Quarterly Journal of the Royal Meteorological Society, Vol. 86, pp. 495-503. (Quoted in Blackadar, 1962).

Ralston, A., 1965. A First Course in Numerical Analysis. McGraw-Hill, New York/Toronto/London.

Reed, R.J. and W.J. Campbell, 1960: A Theory and Observations of the Drift of Ice Station Alpha. Final Report, task number N.R. 307-250, University of Washington.

_____ 1962: The Equilibrium Drift of Ice Station Alpha. Journal of Geophysical Research, Vol. 67, No. 1, pp. 281-297.

Rossby, C.G. and R.B. Montgomery, 1935: The Layer of Frictional Influence in Wind and Ocean Currents. Papers in Physical Oceanography and Meteorology, M.I.T. and Woods Hole Oceanographic Institute, Vol. 3, No. 3.

Sakai, 1922: Linear Conduction of Heat through a Series of Connected Rods. Sci. Rep. Tohoku University. Vol. 11, No. 1, pp. 351-78.

Shuleikin, V.V., 1938: The Drift of Ice Fields. Doklady. Akad. Nauk SSSR, Vol. 19, No. 8. (Translated).

Sverdrup, H.U., 1928: The Wind Drift of the Ice on the North Siberian Shelf. The Norwegian North Polar Expedition with "Maud", 1918-1925, Scientific Results, Vol. 4, No. 1.

Sweers, H.E., 1967: Some Fortran II Programs for Computer processing of oceanographic observations. NATO Subcommittee on Oceanographic Research. Technical Report No. 37, Bergen.

Taylor, G.I., 1916: Skin Friction of the Wind on the Earth's Surface. Proc. Royal Soc. (London), Series A, Vol. 92, pp. 196-199.

Untersteiner, N. and F.I. Badgley, 1965: The Roughness Parameters of Sea Ice. Journal of Geophysical Research, Vol. 70, No. 18, pp. 29-33.

Webster, A.G., 1966: Partial Differential Equations of Mathematical Physics. Dover, New York.

Zubov, N.N., 1943: Arctic Sea Ice. Translated for USAF Cambridge Research Centre.

APPENDIX 1 - Flow Charts of main computer programmes.

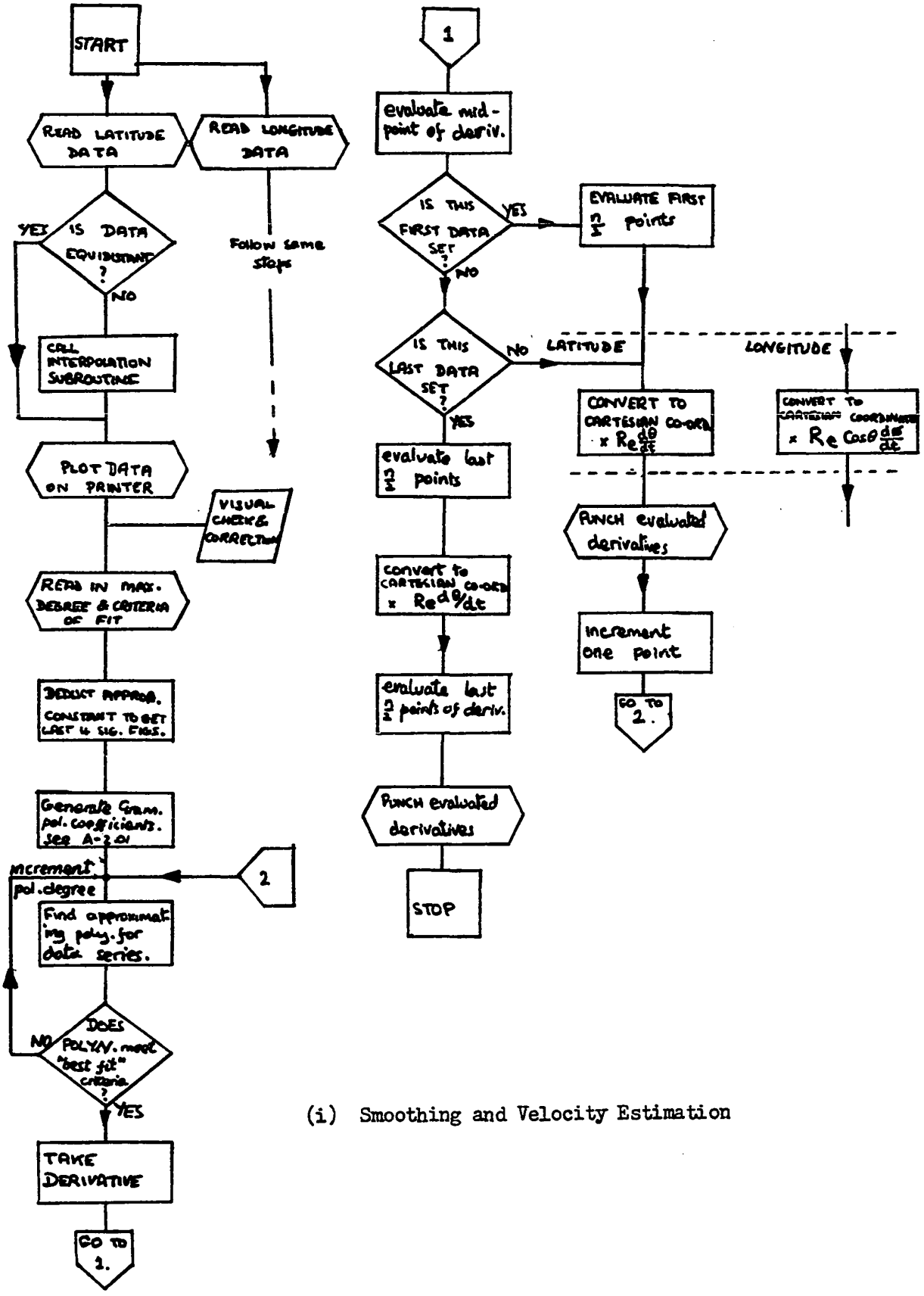

(i) Smoothing and Velocity Estimation

(ii) Tidal Analysis

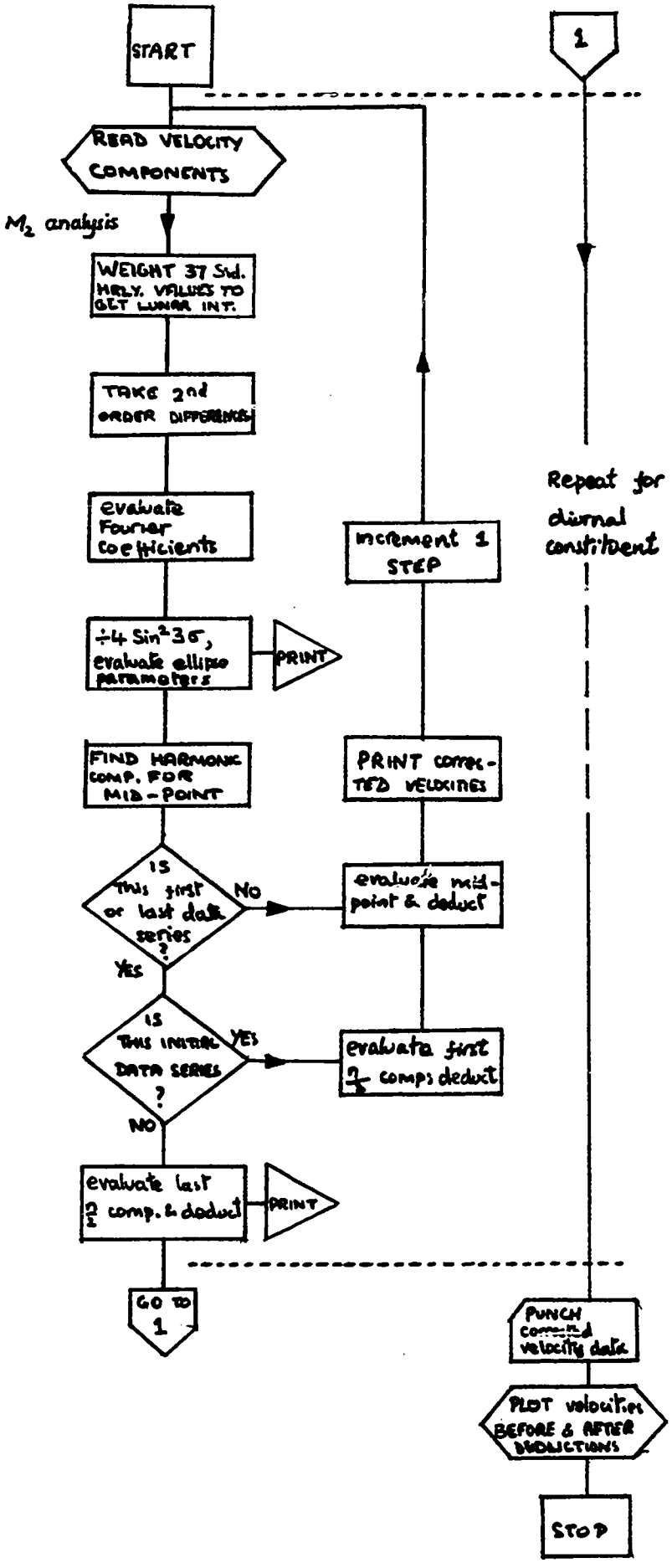

(iii) Spectral Analysis

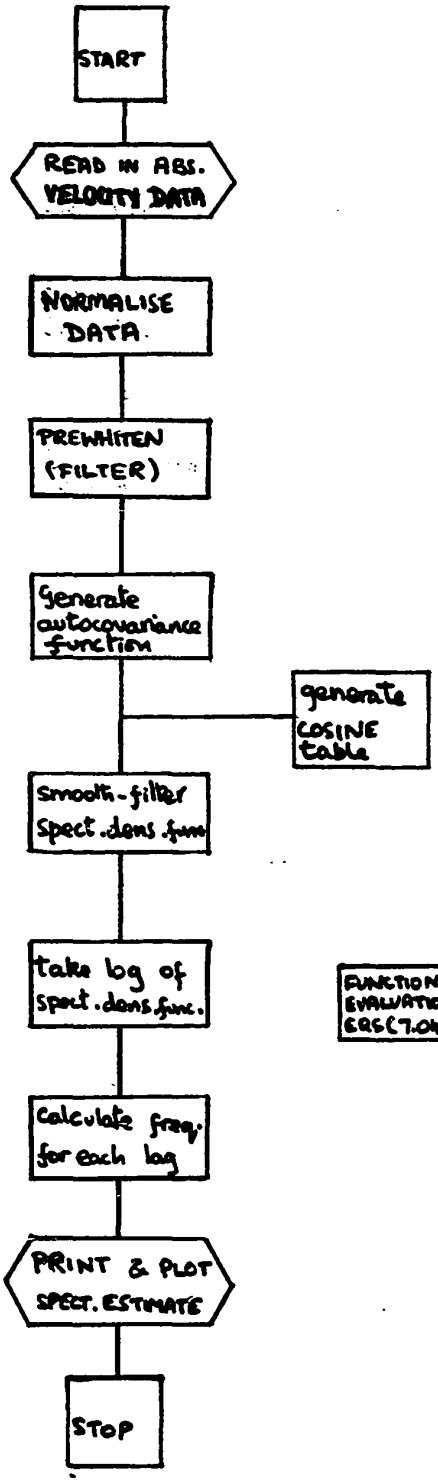

(iv) Numerical Model for Time-Dependent Motion

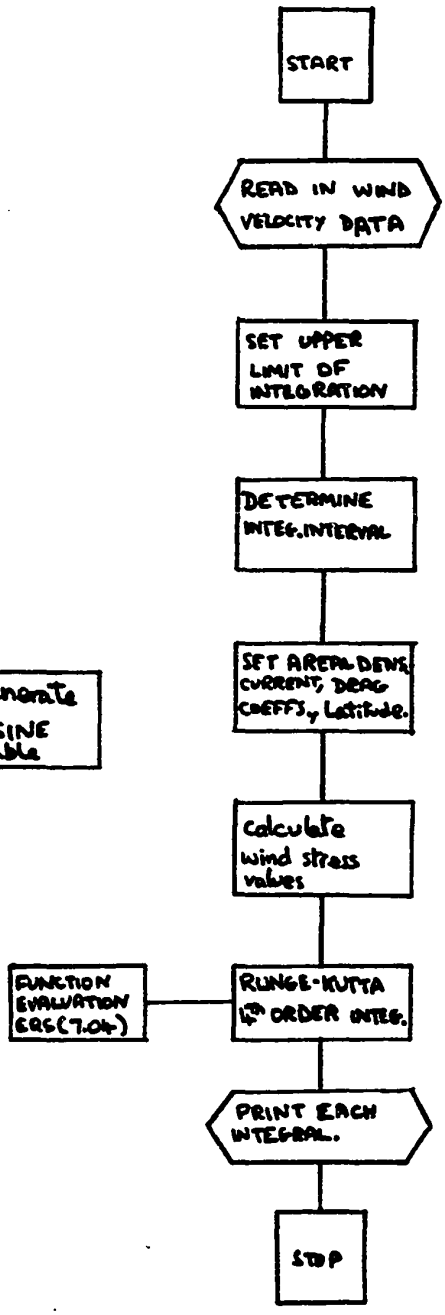

APPENDIX 2 - Scheme for Generating Gram Polynomial Coefficients

Ralston (1965) describes a procedure for using Gram Orthogonal Polynomials in functional approximations. When used with equidistant data great accuracy, speed and flexibility may be obtained. The standard method in this case is to determine each functionally approximated point $y_m(x)$ using orthogonal polynomials up to degree m. It is convenient to take an odd number of points, n, and to let zero be the mid-point of the range of the abscissas. Thus the points are zero centered and extend to $\pm L$ each side of the origin where $L = \frac{n-1}{2}$. We let s be the translated value of x; then,

$$y_m(s) = \sum_{j=0}^{m} b_j P_j(s,L) \qquad \text{.... (A-2.01)}$$

where

$$b_j = \frac{\sum_{i=1}^{n} W_i \bar{f}_i P_j(s_i,L)}{\sum_{i=1}^{n} W_i \left[P_j(s_i,L)\right]^2}$$

W_i = a weighting value

$\bar{f}_i$ = i^{th} original data point

$P_j(s_i,L)$ = the orthogonal polynomial of order j evaluated at s_i, L.

The polynomials $P_j(s,L)$ are generated from the definition (Ralston, 1965):

$$P_j(s,L) = \sum_{k=0}^{j} (-1)^{k+j} \frac{(j+k)^{(2k)}}{(k!)^2} \cdot \frac{(L+s)^{(k)}}{(2L)^{(k)}}$$

.... (A-2.02)

where

$$x^{(n)} = x!/(x-n)! \quad , \text{ the factorial function.}$$

These polynomials have been tabulated by De Lury (1950) for a range of S, j and L. However, this method does not permit us to determine derivatives. For this we need to separate out from (A-2.02) the coefficients of S. A series of these coefficients was calculated and generalised; a recursive relationship was then found which permits the coefficients to be rapidly calculated by machine. Table A-2.01 shows the generating scheme. Much computation time may be saved by making use of the fact that alternate coefficients are zero; it is possible to store the coefficients in a two-dimensional vector to save memory space.

To obtain the coefficients of the approximating polynomial, $a_0, a_1, \ldots\ldots, a_m$, we use the expression (A-2.01) and equate coefficients for each power of S. Thus

$$a_0 = \sum_{j=0}^{m} b_j C_{0,j}$$

$$a_1 = \sum_{j=0}^{m} b_j C_{1,j}$$

$$\vdots$$

$$a_m = \sum_{j=0}^{m} b_j C_{m,j}$$

The author is indebted to R.H. Farmer for assistance in devising this scheme and for finding the recursive relationships given in Table A-2.01.

TABLE A-2.01

For generating coefficients $C_{p,j}$ of number p and polynomial order j .

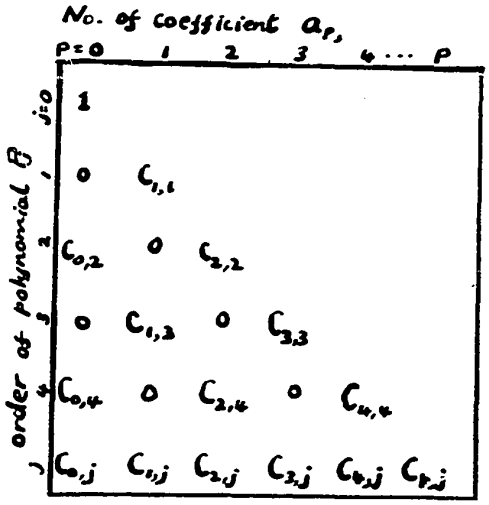

Recursive Relationships:

Each coefficient $C_{p,j}$ is composed of several elements. Let the t^{th} element of $C_{p,j}$ be denoted by square brackets $[p,j,t]$. $C_{0,0} = 1$; all other coefficients in the first column are then found from

$$C_{0,j} = \left\{ -[0,j-1,0] - \sum_{t=1}^{j-1} [0,j-1,t] \frac{(j+t)}{(j-t)} - [0,j,t-1] \right.$$

The coefficients of the last column in each row are found from

$$C_{p,j} = [j-1, j-1, 1] \frac{(4j-2)}{j} \cdot \frac{1}{(2L+j-1)}$$

All remaining coefficients are determined by

$$C_{p,j} = \sum_{t=0}^{j-s-1} \frac{j+t+s}{j-t-s} \cdot [s,j-1,t] + \frac{2j-1}{2} \cdot \frac{1}{2L-j+1} \left\{ [s-1,j-1,j-s-1] + (L-j+1)[s,j-1,j-s-1] \right\}$$

APPENDIX 3 - Wind Data Used in Regression Analysis

On-shore winds selected for meteorological stations around the Gulf from February 13th to 18th. These data were kindly supplied by J. Walmsley.

Geos. Speed (Knots)	Geos. Dir'n (From. deg)	Surface Speed (Knots)	Surface Dir'n (From. deg)
Port Menier			
10	315	10	270
12	285	10	247
10	320	10	247
19	360	15	270
29	320	15	247
18	320	15	270
32	180	15	135
Mont Joli			
10	290	10	180
10	320	10	180
13	295	10	225
14	340	10	225
18	315	20	202
19	325	10	225
28	330	15	225
32	330	15	315
29	325	20	292
47	330	10	292
35	325	15	315
19	315	15	0
20	230	15	180
40	195	15	157
55	330	30	270
80	330	30	292
55	160	20	270
55	335	25	315
Seven Islands			
20	275	1	67
11	300	5	180
19	225	10	67
34	175	15	112

Geos. Speed (Knots)	Geos. Dir'n (From. deg)	Surface Speed (Knots)	Surface Dir'n (From. deg)
Daniel's Harbour			
22	275	20	225
23	255	15	225
5	275	5	202
5	15	5	292
5	345	5	270
70	315	25	270
53	295	40	247
29	270	30	225
22	245	30	225
17	250	20	225
16	285	25	270
13	300	20	270
18	335	15	292
14	315	15	270
10	270	15	225
45	255	40	225
Fox River			
10	330	10	315
31	300	20	292
35	320	25	315
42	150	10	135
70	300	10	292
Natashquan			
50	295	15	270
43	245	25	225
Cape Whittle			
28	280	15	247
25	260	10	225
11	270	5	270
45	285	25	225
10	245	1	202
30	220	30	225
27	230	20	202

Geos. Speed (Knots)	Geos. Dir'n (From. deg)	Surface Speed (Knots)	Surface Dir'n (From. deg)
Grindstone Island			
1	325	1	247
10	15	10	45
10	15	10	45
27	10	15	337
40	5	20	0
33	5	20	0
38	340	25	337
30	335	15	315
40	310	20	315
35	300	20	315
38	270	25	270
30	290	20	315
28	300	15	315
25	305	15	315
35	305	15	315
23	305	15	270
28	315	10	315
21	275	10	292
17	220	15	202
50	185	45	180
60	280	35	270
47	270	35	292
70	270	35	292
55	295	35	315
Miscou Island			
5	355	5	45
40	195	20	180
Port-aux-Basques			
10	15	5	135
33	300	30	270
38	290	25	270
18	270	20	270
25	290	25	270
19	300	15	270
40	195	15	202
45	205	35	225
40	290	35	270
45	270	35	247

APPENDIX 4 - (a) Transformation of Acceleration Equations

(b) Transcendental Functions used in Chapter 8

(a) Transformation of Acceleration Equations:

To show that equations (8.01) and (8.03) imply (8.04):

First substitute (8.03) into (8.01) to obtain

(i) $\varphi_t \cos ft - f\varphi \sin ft + \psi_t \sin ft + f\psi \cos ft + f\varphi \sin ft - f\psi \cos ft =$
$(K_m \varphi_z)_z \cos ft + (K_m \psi_z)_z \sin ft$

(ii) $-\varphi_t \sin ft - f\varphi \cos ft + \psi_t \cos ft - f\psi \sin ft + f\varphi \cos ft + f\psi \sin ft =$
$-(K_m \varphi_z)_z \sin ft + (K_m \psi_z) \cos ft$

Now multiply (i) by $\cos ft$ and (ii) by $\sin ft$

(iii) $\varphi_t \cos^2 ft + \psi_t \sin ft \cos ft = (K_m \varphi_z)_z \cos^2 ft + (K_m \psi_z)_z \sin ft \cos ft$

(iv) $-\varphi_t \sin^2 ft + \psi_t \sin ft \cos ft = -(K_m \varphi_z)_z \sin^2 ft + (K_m \psi_z)_z \sin ft \cos ft$

Adding (iii) and (iv) gives

(v) $\varphi_t \cos 2ft + \psi_t \sin ft \cos ft = (K_m \varphi_z)_z \cos 2ft + 2(K_m \psi_z)_z \sin ft \cos ft$

and subtracting (iv) from (iii) gives

(vi) $\varphi_t = (K_m \varphi_z)_z$

Substituting (vi) into (v) gives

$$\psi_t = (K_m \psi_z)_z$$

as required.

(b) Transcendental Functions used in Chapter 8:

(i) Gamma Function:

$$\Gamma(x) = \int_0^\infty e^{-t} t^{x-1}\, dt$$

(ii) Incomplete Gamma Function:

$$\Gamma(\alpha,x) = \int_x^\infty e^{-t} t^{\alpha-1}\, dt$$

This may be written

$$\Gamma(\alpha,x) = \Gamma(\alpha) - \gamma(\alpha,x)$$

where $\gamma(\alpha,x)$ is the complementary part of $\Gamma(\alpha,x)$:

$$\gamma(\alpha,x) = \int_0^x e^{-t} t^{\alpha-1}\, dt$$

(iii) $\Gamma(\tfrac{1}{2}) = \sqrt{\pi}$

(iv) Error Function

$$\operatorname{erf}(x) = \frac{2}{\sqrt{\pi}} \int_0^x e^{-t^2}\, dt$$

(v) Complementary Error Function

$$\operatorname{erfc}(x) = 1 - \operatorname{erf}(x)$$

(vi) $\sqrt{\pi}\, \operatorname{erf}(x) = \gamma(\tfrac{1}{2}, x^2)$

(vii) $$\frac{d^n}{dx^n} \operatorname{erf}(x) = (-1)^{n+1} \frac{2^n}{\sqrt{\pi}} x^{n-1} e^{-x^2}$$

APPENDIX 5 - Modification to permit non-zero initial conditions in transient model Chap. 8.

If we choose to consider non-zero initial conditions, we have:

$$\varphi(z,0) = U(z,0)$$

$$\psi(z,0) = V(z,0)$$

where $U(z,0)$, $V(z,0)$ are the known initial velocities. For instance, we might assume that at time $t=0$ we have a steady state Ekman type of flow with ice travelling at velocity V_0 in the v -direction. Solving the Ekman equations under these conditions would give:

(i) $$\varphi(z,0) = -V_0 e^{-\left[\frac{f\rho_w}{2K_m}\right]^{\frac{1}{2}} z} \cos\left(\left[\frac{f\rho_w}{2K_m}\right]^{\frac{1}{2}} z + \pi/2\right)$$

(ii) $$\psi(z,0) = -V_0 e^{-\left[\frac{f\rho_w}{2K_m}\right]^{\frac{1}{2}} z} \sin\left(\left[\frac{f\rho_w}{2K_m}\right]^{\frac{1}{2}} z + \pi/2\right)$$

To obtain the actual value of $\varphi(z,t)$, $\psi(z,t)$ due to the instantaneous plane source at $\varphi(z',t)$, $\psi(z',t)$ we must find the Green's function of equations (8.04). This is given (Carslaw & Jaegar, 1959) by:

(iii) $$\frac{1}{2\sqrt{\pi K_m (t-\tau)}} \left\{ e^{-(z-z')^2/4K_m(t-\tau)} - e^{-(z+z')^2/4K_m(t-\tau)} \right\}$$

The modified value of $\varphi(z,t)$, $\psi(z,t)$ is then obtained by integrating the product of (iii) with (i) and (iii) with (ii) respectively, over depth, and adding the result to the solution determined for zero initial conditions:

(iv) $$\varphi(z,t) = \frac{1}{2\sqrt{\pi K_m t}} \left[\int_0^\infty \varphi(\xi,0) \left\{ e^{\frac{-(z-\xi)^2}{4K_m t}} - e^{\frac{-(z+\xi)^2}{4K_m t}} \right\} d\xi + z \int_0^t \chi_\varphi(\tau) e^{-z^2/4K_m(t-\tau)} (t-\tau)^{-\frac{3}{2}} d\tau \right.$$

where $\varphi(\xi,0)$ is defined by (i). The initial condition part of (iv) rapidly becomes small compared to the other part, and may then be dropped from the solution.

NOTATION

In order of use; applicable except where otherwise indicated in the text.

Symbol	Meaning	Page where first used
u, v	x, y components of ice velocity	14
θ	Latitude	14
ϕ	Longitude	14
R_e	radius of the earth	14
R_t	amplitude of tidal oscillation	22
σ	angular frequency of tide	22
φ	phaselag of tide	22
t	time	22
δ	random fluctuations	22
Δ^i	i^{th} order difference	22
χ	orientation of tidal ellipse	23
τ_{max}	time of maximum tidal velocity	24
u_g, v_g	x, y components of geostrophic wind	34
f	Coriolis Parameter = $2\Omega \sin\theta$	34
Ω	angular velocity of earth	34
p_a	atmospheric pressure	34
ρ_a	density of air	34
u_z, v_z	x, y components of velocity at height z	36
K_m	kinematic eddy viscosity	36
k	von Karmàn constànt	37
u^*	surface friction velocity	37
ϵ	rate of dissipation of turbulent energy	37
l	typical eddy length	37
λ	value of l in the free atmosphere	37

NOTATION (cont'd.)

Symbol	Meaning	Page where first used
z_o	surface roughness parameter	37
α_o	cross-isobar wind-angle	37
p	constants defining viscosity distribution	39
R	% reduction from geostrophic to surface wind	42
w	absolute value of wind velocity	46
M_n	mean of data series	47
S.D.	standard deviation of data series	47
C_j	cross-correlation for lag j.	47
D_i	i^{th} absolute value of ice drift velocity	47
$\hat{C}(f)$	autospectra at frequency f	51
d.f.	degrees of freedom	51
α_p	variable used to define % confidence: $100(1-\alpha_p)$	51
$\chi_{d.f.}$	probability distribution	51
τ_{ax}, τ_{ay}	x, y components of wind-stress	52
$\vec{D}$	Coriolis force = $\text{mass} \times f \times \vec{V}_i \times \vec{k}$	52
ρ_i	ice density	52
h_i	ice thickness	52
$\vec{i}, \vec{j}, \vec{k}$	unit orthog. vectors, $\vec{k}$ pointing vertically up	52
α'_w	drag coefficient of water (Prandtl boundary layer)	54
$\vec{V}_i$	ice velocity vector	54
$\vec{r}$	relative velocity between ice and top of spiral layer	54
H_f	boundary layer thickness	54
β	angle between $\vec{V}_i$ and $\vec{r}$	54

NOTATION (cont'd.)

Symbol	Meaning	Page where first used
α	angle between $\vec{\tau}_a$ and $\vec{V}_i$	54
ρ_w	density of water	54
c_i	constants defining drag per unit mass	59
W_x, W_y	x, y components of surface wind velocity	59
K_w	water drag coefficient (numerical model)	63
K_a	air drag coefficient (numerical model)	63
c_x, c_y	x, y components of geostrophic current	68
m	areal density	68
μ_e	coefficient of eddy viscosity	76
$L\{\ \}$	Laplace Transformation of $\{\ \}$	80
$\bar{\chi}_\varphi, \bar{\chi}_\psi$	the constant value of $\chi_\varphi(\tau)$, $\chi_\psi(\tau)$	82

$F, G, \varphi, \psi, \chi_\varphi, \chi_\psi$ are used as function names

All times are given in G.M.T. unless otherwise indicated

1 Pendulum Hour = $\frac{\pi}{12\Omega \sin\theta}$

1 Knot = 51.48 cm/sec